



**Politecnico
di Torino**



**UNIVERSITÀ
DEGLI STUDI
DI TORINO**

Doctoral Dissertation
Doctoral Program in Bioengineering and Medical-Surgical Sciences (33th cycle)

Development of innovative systems for clinical Pulse Wave Velocity assessment

New diagnostic and therapeutic devices,
systems and techniques

Irene Buraioli

* * * * *

Supervisors

Prof. Danilo Demarchi, Supervisor
Prof. Franco Veglio, Co-supervisor

Doctoral Examination Committee:

Prof. Paolo Samorì, Referee, University of Strasbourg
Prof. Andrea De Marcellis, Referee, University of L'Aquila

Politecnico di Torino
May 1th, 2021

This thesis is licensed under a Creative Commons License, Attribution - Noncommercial- NoDerivative Works 4.0 International: see www.creativecommons.org. The text may be reproduced for non-commercial purposes, provided that credit is given to the original author.

I hereby declare that, the contents and organisation of this dissertation constitute my own original work and does not compromise in any way the rights of third parties, including those relating to the security of personal data.

.....
Irene Buraioli
Turin, May 1th, 2021

Summary

In collaboration with STMicroelectronics, University of Torino (Città della Salute e della Scienza di Torino Hospital) and PolitoBIOMed Lab interdepartmental laboratory, the main aim of my research project is the design of a low-cost Pulse Wave Velocity (PWV) estimation system. This activity is born as answer to a specific medical request to have an affordable, but reliable, PWV estimator. The principal goal is the possibility to have a wearable device to improve from punctual measurement to a continuous monitoring of the PWV cardiovascular parameter.

Pulse Wave Velocity is a hemodynamic parameter that describes the velocity at which the blood pressure pulse propagates through the arterial tree. PWV estimation relies on the extraction of Pulse Transit Time (PTT), that is the time employed by blood pulse to propagate between two points and on the measured distance between the two considered point. PWV is becoming more and more important in clinical diagnosis because it is an independent cardiovascular risk predictor and it contributes to global cardiovascular risk stratification, as highlighted by European Society of Cardiology and Hypertension. Unlike all other cardiovascular parameters, the propagation speed manages to maintain its predictive and prognostic value even where the others prove unreliable and, for this reason, it is considered the gold standard among the stiffness indices.

However, this parameter's importance struggles to take off in medical practice and expand in the clinical environment for many reasons. One of the mains is the difficulty in carrying out the measurement and the time employed. So far, the evaluation of PWV takes place in a timely manner: first the signals of the pulse waves are acquired, and then, in a second moment, the speed that this wave takes to propagate between two points is evaluated through specific algorithms.

When this project starts, no solution guaranteed continuous monitoring of the parameter as a direct retroactive control of the subject's state of health under examination. The time required for data analysis and estimation means that this measure, although very useful because it is correlated with multiple physiological parameters (blood pressure, heart rate, etc.), is not much used in clinical practice.

This perspective can undergo a radical change through this thesis, allowing the diffusion of the evaluation of the PWV parameter itself.

With the conducted project, it is possible to monitor the PWV trend in real-time, considerably expanding the potential applications and drastically modifying the procedure even in environments where, today, given the measurement's difficulty and impracticality, it is not much considered. In particular, this work's final purpose was to design a device reliable in the measurement, with a procedure easy to carry out and that does not require a high economic investment by the user, i.e. made with components take out of the shelf.

Different sensors and methodologies were evaluated to pursue this goal, starting from bio-sensors, their electronic conditioning circuits, and their algorithms for parameter extraction.

Chapter 1 gives a wide-ranging sight on the cardiovascular system and its physiology, the considered bio-signals, the electronic components used and the relative softwares. Meanwhile, the others chapter described four different designed and testes systems for the non-invasive and continuous PWV assessment. In particular, Chapter 2 presents ATHOS, that is a tonometer-based prototypal device validated through an official clinical study on 90 volunteers.

In the following, Chapter 3, 4 and 5 three other instruments are introduced with the purpose to obtain a wearable system, without the need of a specialized operator, and that involves respectively the PhonoCardioGram (PCG), the PhotoPlethysmoGram (PPG) and the pressure pulse acquired by innovative graphene pressure sensor.

Finally, the last Chapter 6 contains the final considerations and the future developments.

Contents

List of Tables	9
List of Figures	10
1 Background	13
1.1 The Cardiovascular system	14
1.1.1 The heart	15
1.1.2 The cardiac period	16
1.1.3 The vessels	21
1.1.4 Arterial Blood Pressure and Hypertension	24
1.2 Analyzed Biological Signals	25
1.2.1 Electrocardiogram Signal	25
1.2.2 Photoplethysmogram Signal	31
1.2.3 Phonocardiogram Signal	34
1.2.4 Arterial Pulse	35
1.3 Pulse Wave Velocity	38
1.3.1 Evaluation methodology and Commercial Devices	41
1.4 Studied sensors	48
1.4.1 Tonometer	48
1.4.2 Optical Sensors	49
1.4.3 Analog Microphone MP33AB01H	52
1.4.4 Graphene pressure sensor	53
1.5 Implemented Device	56
1.5.1 STM32F429 Discovery Kit	56
1.5.2 STEVAL-IDB006V1M	57
1.5.3 STEVAL-IME002-V1	58
1.6 Used Softwares	59
1.6.1 Keil	59
1.6.2 VisualStudio	59
1.6.3 Matlab	60

2	The ATHOS device	61
2.1	System overview	62
2.2	The system hardware	63
2.2.1	Tonometers interconnection	65
2.2.2	ECG EDAN SE-1	66
2.2.3	The firmware and Bluetooth transmission	68
2.3	The system software	70
2.3.1	The intersecting tangent point	72
2.3.2	The filters	72
2.3.3	The algorithm for real-time PWV	73
2.4	The PWV acquisition procedure	77
2.5	System Validation	81
2.5.1	Results	84
2.5.2	Results Discussion	88
3	PWV with Phonocardiogram	91
3.1	Hardware implementation	92
3.2	Signal Analysis	96
3.2.1	Frequencies analysis	97
3.2.2	Shape repeatability and feature extraction	100
3.3	Validation Results	102
4	PWV with Photoplethysmography	107
4.1	System Hardware	108
4.1.1	Photoplethysmogram signal Acquisition	109
4.1.2	Phonocardiogram signal Acquisition	113
4.1.3	Elettrocardiogram signal Acquisition	114
4.1.4	Tonometer signal Acquisition	115
4.1.5	Acquisitions Management	115
4.2	Signals analysis	116
4.3	Acquisitions	117
4.3.1	Carotid acquisition	117
4.3.2	Carotid-Femoral acquisition	119
4.4	Results Discussion	123
5	PWV with Graphene pressure sensor	125
5.1	HardWare implementation	125
5.1.1	Graphene pressure sensor signal Acquisition	126
5.1.2	Elettrocardiogram signal Acquisition	129
5.1.3	Tonometer signal Acquisition	129
5.1.4	Acquisitions Management	129
5.2	Signals Analysis	130
5.2.1	Cross-correlation technique	131

5.3	Validation Results	133
5.3.1	ITP method	133
5.3.2	Cross-correlation method	135
5.4	Results Discussion	136
6	Conclusions	137
A	Articles copyrights	139
	Nomenclature	141
	Bibliography	143

List of Tables

1.1	Classification of hypertension grade	25
1.2	Pulse Wave Velocity value according to the age	40
1.3	Current commercial devices	46
2.1	Transmit and receive in bidirectional mode with STM32F429ZIT6	65
2.2	ATHOS study population	82
2.3	ATHOS results compared with SphygmoCor	85
2.4	Classes of accuracy by Artery Society Guidelines	88
2.5	Validation studies of the commercial and ATHOS devices	89
3.1	PTTs with phonocardiogram VS tonometer	105
4.1	Carotid PTTs obtained with all the considered sensors	118
4.2	Configuration <i>a</i> results	120
4.3	Configuration <i>b</i> results	121
4.4	Configuration <i>c</i> results	123
5.1	Results graphene with ITP VS ATHOS VS SphygmoCor	134
5.2	Results graphene with cross-correlation VS ATHOS VS SphygmoCor	136

List of Figures

1.1	Cross Section of human heart	15
1.2	Electrical conduction in the heart	17
1.3	Cardiac cycle and its phases	19
1.4	The blood flow	21
1.5	Section of an artery	22
1.6	Human circulatory system	23
1.7	Aortic pressure variation	24
1.8	Electrocardiogram Signal	26
1.9	Bipolar limb leads	28
1.10	Electrocardiogram augmented limb leads	29
1.11	Unipolar chest leads configuration	30
1.12	PhotoPlethysmoGram signal components	32
1.13	PhotoPlethysmoGram signal characteristic parameters	33
1.14	PhonoCardioGram signal components	34
1.15	A cylindrical shell wall tension	36
1.16	Pulse pressure amplification in the arterial system	37
1.17	Arterial Pulse characteristic parameters	38
1.18	Pulse Wave Velocity measurement	39
1.19	Pulse Wave Velocity value according to the age	40
1.20	Clinical PWV assessment	41
1.21	Sphygmocor Device	42
1.22	PulsePen Device	43
1.23	Complior Device	43
1.24	Arteriograph Device	44
1.25	Vicorder Device	45
1.26	pOpmètre Device	45
1.27	LPS35HW acquisition chain	48
1.28	Tonometer MEMS sensor	49
1.29	ST Physiological probe	50
1.30	ST Physiological probe technological details	50
1.31	Osram SFH7050 sensor	51
1.32	MP33AB01H frequency response	52

1.33	MP33AB01H mechanical configuration	53
1.34	Working principle of the graphene pressure sensor	54
1.35	Synthesis and architecture of rGO-R ₁ , rGO-R ₂ , and rGO-R ₃	55
1.36	Graphene pressure sensor fabrication process	55
1.37	Relative resistance as a function of the pressure applied	56
1.38	Discovery Kit STM32F429	57
1.39	Steval-IDB006V1M	58
1.40	STeval-IME002-V1	59
2.1	ATHOS device summary scheme	62
2.2	Block diagram of ATHOS system	63
2.3	ATHOS power supply scheme	64
2.4	ATHOS main device unit	64
2.5	ATHOS sensors probes	66
2.6	ECG Edan SE-1 and its configuration	66
2.7	EDAN SE-1 analog conditioning	67
2.8	STM32F429ZIT6 microcontroller interconnections in ATHOS	68
2.9	The ATHOS STM32F429ZIT6 microcontroller firmware flowchart	69
2.10	The ATHOS Bluetooth protocol	69
2.11	Block diagram of ATHOS system	70
2.12	ATHOS transferred buffer processing	71
2.13	Extraction of Intersecting Tangent Point (ITP)	72
2.14	Biquadratic Cascade IIR Filters block diagram	73
2.15	First stage of the real-time PWV assessment	74
2.16	To-append buffer creation	76
2.17	Summary of the real-time “intersecting tangent” feature extraction	77
2.18	ATHOS Study and patient data window	78
2.19	ATHOS acquisition window	79
2.20	ATHOS Graphical User Interface menu bar	79
2.21	ATHOS Report Window	80
2.22	Flow chart of ATHOS study protocol	83
2.23	Box-plot comparison of PWV from SphygmoCor and ATHOS	84
2.24	PTT Bland Altman plot SphygmoCor VS ATHOS	86
2.25	PTT scatter plot SphygmoCor VS ATHOS	86
2.26	PWV Bland Altman plot SphygmoCor VS ATHOS	87
2.27	PWV scatter plot SphygmoCor VS ATHOS	87
3.1	Phonocardiogram signals acquisition system	92
3.2	Sensor configuration for the PCG acquisition.	93
3.3	Microphone analog signal conditioning diagram	93
3.4	Conditioning circuit of PCG acquisition channels	94
3.5	Interconnections diagram of the PCG system	95
3.6	Phonocardiogram signals filtering	96
3.7	Ear Tangent Point feature in PCG signal	97

3.8	Phonocardiogram frequencies analysis	98
3.9	Plot of the two components forming the signal detected by a microphone on the skin in proximity of an artery	99
3.10	Shape repeatability analysis of displacement and sound signals	101
3.11	Sound pulse wave considered features	101
3.12	Flow chart of the phonocardiogram signal post-processing	103
3.13	cfPTT with phonocardiogram and Intersecting Tangent Point feature	104
3.14	PCG and tonometer simultaneous acquisitions	105
4.1	Photoplethysmography system overview	108
4.2	Acquisition board configuration	109
4.3	Acquisition board diagram	109
4.4	Optical sensor analog conditioning diagram	110
4.5	Osram Sensor polarization circuit	110
4.6	Osram sensor analog conditioning circuit	111
4.7	SiPM Sensor polarization circuit	112
4.8	SiPM sensor analog conditioning circuit	113
4.9	Analog microphone conditioning diagram	113
4.10	Analog microphone conditioning circuit	114
4.11	Electrocardiogram conditioning circuit	114
4.12	The system firmware flowchart	115
4.13	All the analyzed signals and relative features	116
4.14	Sensor configuration for the total system acquisition	117
4.15	Configuration <i>a</i> signals and features	119
4.16	Configuration <i>b</i> signals and features	121
4.17	Configuration <i>c</i> signals and features	122
5.1	Graphene pressure sensor system overview	126
5.2	New acquisition board flowchart	126
5.3	Graphene pressure sensor conditioning diagram	127
5.4	Graphene pressure sensor analog conditioning circuit	127
5.5	Graphene pressure sensor	128
5.6	Sensor configuration for graphene acquisition	129
5.7	features analysis with graphene signals	130
5.8	Cross-correlation algorithm flow chart	131
5.9	Cross-Correlation technique	132
5.10	Final set up of the graphene system	133
5.11	Clinical protocol for graphene validation	134
5.12	PWV Bland Altman plot graphene(ITP) VS SphygmoCor	135
5.13	PWV Bland Altman plot graphene(cross-correlation) VS SphygmoCor	135
A.1	IEEE copyright request 1	139
A.2	IEEE copyright request 2	140

Chapter 1

Background

This doctoral thesis' main aim was the design of a low-cost clinical device for a suitable and reliable Pulse Wave Velocity (PWV) estimation. According to this goal, in this first chapter are introduced all the topics and devices later treated in details and that let to be better introduced in the field.

In the detail, the cardiovascular system is firstly presented: the heart, the cardiac period, and the vessels. Secondly, its major correlated illnesses are treated, focusing on the hypertension. This last, in fact, is the main pathology faced in this thesis, for its straight correlation with the arterial stiffness.

In the second section, all the bio-signals used in these years to extract the velocity of the blood pulse are explained. The electrocardiogram, related to the electrical activity of the heart. The phonocardiogram, that is linked with the sounds emitted by the passage of the hematic flow in the vessel. The photoplethysmogram signal, related to the amount of light absorbed by the blood during the cardiac period. And, at the end, the Pulse Wave as the direct detection of superficial tension variation on the skin in proximity of a vessel walls.

In a third part, a detailed explanation of Pulse Wave Velocity is given, together with its utility and the clinical devices for its assessment currently in the market.

While, lastly, the electric devices implemented in this work and the relative Software are treated.

1.1 The Cardiovascular system

The human cardiovascular system is an organ system that transports blood through vessels to and from all parts of the body, conveying sources of nourishment and oxygen to tissues and clearing away carbon dioxide and other wastes. It is formed by a closed structure of tubes where the blood is pushed by a central muscular pump, the heart. Two circuits can be distinguished: the pulmonary and the systemic. The both consist of arterial, capillary, and venous components [1].

Pulmonary circulation is a part of the circulatory system responsible for forming a circuit of vessels that transport blood between the heart and the lungs. Systemic circulation, on the other hand, forms a closed circuit between the heart and the rest of the body. It aids in transporting oxygenated blood, which carries nutrients, to different tissues.

The entire blood path starts in the arteries which receive the oxygenated blood at high velocity and pressure and transport it around the body. The blood passes through different sizes of arteries: from the aorta, the biggest one, to the arterioles and the capillaries, the final microscopic branches of arteries, where cellular nutrients are distributed and waste products are received. The deoxygenated blood, loaded with waste products, flows from capillaries to the venous systems. This capillaries-fusion forms venules and finally veins that converge into superior and inferior venae cavae. The two final main veins allow deoxygenated blood back to the heart [2].

The circulatory system has three primary functions:

- *Protection:* It performs a protective action through white blood cells, which clean up cellular debris and delete pathogens that may have entered the body. In addition, red blood cells and platelets operate to protect wounds. Among other things, blood also transports antibodies, which provide selective protection from pathogens to which the body has already been exposed to;
- *Regulation:* It helps to monitor body temperature and to keep it stable, by controlling the blood flow. Blood can help to regulate the body PH, that may be altered for the presence of sodium bicarbonate, which acts as a buffer solution;
- *Transport:* It allows blood transport along the body and this permits to carry nutrients, oxygen, and hormones.

1.1.1 The heart

The heart is the cardiovascular system core and pushes the blood through all the body. It is cone-shaped, with the broad base directed upward and to the right and the apex pointing downward and to the left. This organ is located between the lungs, in the middle of the chest, behind and slightly to the left of the sternum.

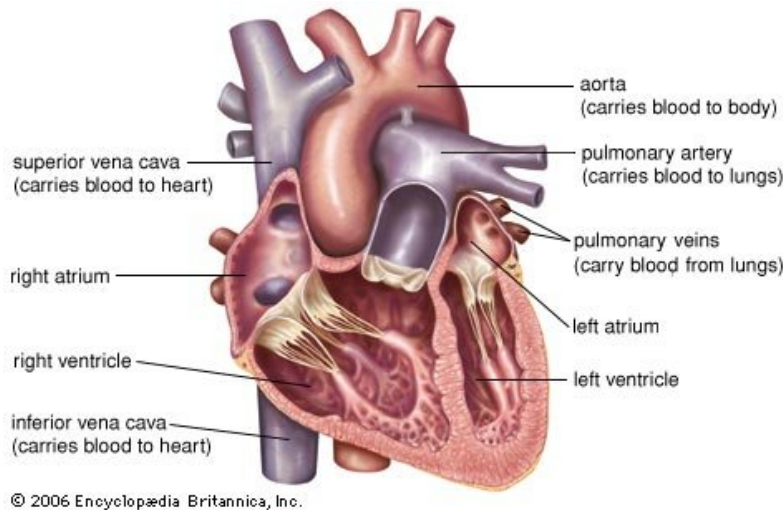


Figure 1.1: Cross Section of human heart [1].

The heart is appended in its own membranous bag, the *pericardium*. The robust outer section of the sac, or fibrous pericardium, is tightly attached to the diaphragm below, the mediastinal pleura on the side, and the sternum in front. The outer portion is attached by ligaments to the spinal column, diaphragm, and other parts of the body, and the inner one is adhered to the heart muscle. A coating of fluid separates the two layers of membrane, lubricating the two membranes with every beat of the heart [1].

The heart has four chambers, Figure 1.1. It is divided by *septa*, or partitions, into right and left halves, and each half is subdivided into two chambers respectively. The upper chambers are called left and right atria and are separated by a portion named interatrial septum. Meanwhile, the lower chambers are known as left and right ventricles and divided by the interventricular septum.

The *right atrium*, or right superior portion of the heart, is a thin-walled chamber receiving blood from all tissues except the lungs and merged into the superior (upper body) and inferior (lower body) venae cavae. Blood flows from the right atrium to the *right ventricle*, the right inferior portion of the heart. It is the chamber from which the pulmonary artery carries blood to the lungs.

The *left atrium*, smaller and thinner than the other upper part, collects the oxygenated blood from the pulmonary veins. This blood then flows into the *left ventricle*, that is the largest and strongest chamber: its walls are only about a half-inch thick, but they have enough force to push blood through the aortic valve and into the body, through the aorta.

Because of the watertight lining of the heart (the *endocardium*) and the thickness of the myocardium, the heart cannot depend on the blood contained in its own chambers for oxygen and nourishment. It possesses a vascular system of its own, called the *coronary arterial system*. Heart's structure could be considered as divided into two separated districts: the left, where blood is deoxygenated, coming through vena cava, courses to the lung, and the right part that allows for the oxygen-rich blood, coming from the pulmonary district, to be pushed in the aorta.

These two parts are separated by valves. There are totally four valves and all of them work with a pressure gradient: blood moves from the side where the pressure is higher to the side where it is lower. In particular, two types of valves can be distinguished: atrium-ventricular and semilunar. The former valves are thin and let the blood to flow from the atrium to the ventricle, meanwhile the latter are the ones connecting ventricles with the two principal arteries (aorta and pulmonary artery). There are four different valves: *tricuspid* (between right atrium and ventricle, so called because it consists of three irregularly shaped cusps), *pulmonary* (between right ventricle and pulmonary artery), *mitral* (between left atrium and ventricle) and *aortic* (between left ventricle and aorta). Closure of the heart valves is associated with an audible sound, called the *heartbeat*. The first sound occurs when the mitral and tricuspid valves close, the second when the pulmonary and aortic semilunar valves close [1].

1.1.2 The cardiac period

Electrical impulses from the myocardium, the heart muscle, cause its contraction. These begin from the *sinoatrial node* (SA), that is located at the top of the right atrium, behaves as “natural pacemaker”. From it, the impulse travels through the atria and ventricles muscle fibres causing them to contract. This contraction happens with a regular and natural frequency but its rate could be subjected to variations depending on physical demands, stress, or hormonal factors; this is controlled by the autonomous and central nervous system.

In particular, the heart beating is achieved thanks to the innate rhythmicity of the cardiac muscle; no nerves are situated within the organ itself. The mere possession of this intrinsic ability is not sufficient, however, without a right coordination to enable the heart to function efficiently. For this purpose, two

small specialized masses of tissue, or nodes, are in charge of originating the impulses that later are propagated through an elaborate conducting system, with terminal branches extending to the inner surface of the ventricles. The impulse is propagated as a wave that travels from cell to cell. Voltage-sensitive protein channels on the surface of the *sarcolemma*, the membrane that surrounds the muscle fibre, support the flow of current as it relates to the flow of specific ions (ion-specific channels) and to the relative difference in electrocal potential between the outer and inner sides. When an excess of negative ions inside the sarcolemma is generated, an opposite and equal amount of positive ions occurs outside. When a nerve impulse stimulates ion channels to open, positive ions (potassium) flow into the cell and cause depolarization, which leads to muscle cell contraction.

Under relaxing conditions, the heart cell is for the most part penetrable exclusively by positively charged potassium ions, which gradually pervade the cell. In the sinoatrial node are situated specialized pacemaker cells, in which the negative resting potential moves rhythmically towards the positive threshold. When the threshold potential is surpassed, the cell activates its depolarization and there is an aperture of ion channels that transport sodium and calcium into the cell. This abrupt growth in the heart membrane potential is transmitted from cell to cell, creating a depolarization wave that functionally represents the heart's excitation signal. Then, specialized atrial cells speedily propagate this signal through conduction tissue: the atrioventricular node, and His and Purkinje

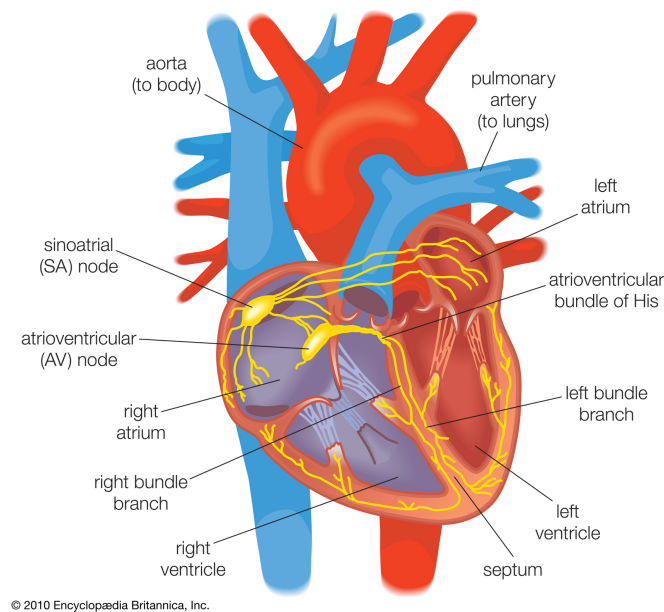


Figure 1.2: Electrical conduction in the heart [1].

cell bundles. The dispersion is followed by slower signal diffusion into ventricular muscle cells (Figure 1.2) [1].

Each time the heart beats, following the sinoatrial node stimulus, a new cardiac period is produced. In this, every chamber activity is composed by two phases: diastole, a filling phase, and systole, a contracting one. *Diastole* denotes the piece of time when the ventricles are relaxed (not contracting). *Systole* represents the period in which the left and right ventricles contract and eject blood into the aorta and pulmonary artery, respectively. During systole, the aortic and pulmonic valves open to permit ejection into the aorta and pulmonary artery. The atrioventricular valves are closed during systole, therefore no blood is entering the ventricles; however, blood continues to enter the atria through the vena cavae and pulmonary veins [3].

The cardiac cycle diagram presented in Figure 1.3 shows to the right depicts changes in aortic pressure (AP), left ventricular pressure (LVP), left atrial pressure (LAP), left ventricular volume (LV Vol), and heart sounds during a single cycle of cardiac contraction and relaxation. These changes are related in time to the electrocardiogram (better described in 1.2.1).

In particular, five different steps could be discerned in each section (right or left part).

1. *Atrial Contraction:*

As the atria contract, the pressure within the atrial chambers increases, which forces more blood flow across the open atrioventricular (AV) valves, leading to a rapid flow of blood into the ventricles. Atrial contraction normally accounts for about 10% of left ventricular filling when a person is at rest, arriving up to 40% with high heart rates.

After atrial contraction is complete, the atrial pressure begins to fall causing a pressure gradient reversal across the AV valves. This causes the valves to float upward (pre-position) before closure. At this time, the ventricular volumes are maximal, which is termed the end-diastolic volume (EDV in Figure 1.3).

(Atrium-Ventricular Valve opened, SemiLunar Valve closed)

2. *Isovolumetric Contraction:*

Myocyte contraction and a rapid increase in intraventricular pressure occurs. Early in this phase, the rate of pressure development becomes maximal. The AV valves close when intraventricular pressure exceeds atrial pressure (first heart sound S_1).

During the time period between the closure of the AV valves and the opening

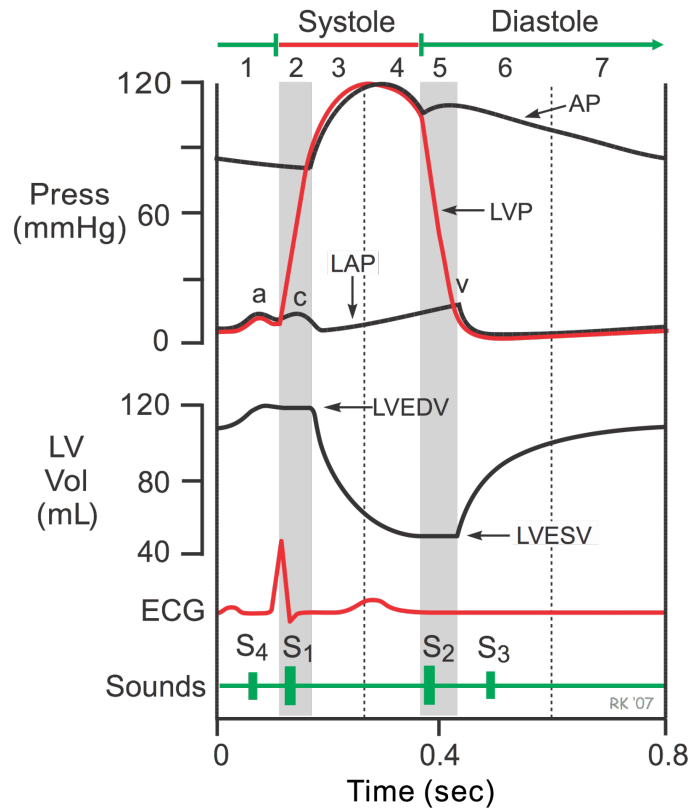


Figure 1.3: Cardiac cycle and its phases [3].

of the aortic and pulmonic valves, ventricular pressure rises rapidly without a change in ventricular volume (i.e., no ejection occurs).

(Atrium-Ventricular Valve closed, SemiLunar Valve closed)

3. *Rapid Ejection:*

This phase represents the initial and rapid ejection of blood into the aorta and pulmonary arteries from the left and right ventricles, respectively. Expulsion begins when intraventricular pressures becomes higher than the pressures within the aorta and pulmonary artery, causing the aortic and pulmonary valves to open. The blood is driven out because the total energy of the blood inside the ventricle exceeds the total energy of the blood inside the aorta. The maximum outflow velocity is reached at the beginning of the ejection phase and the maximum (systolic) pressures of the aorta and pulmonary artery are achieved.

(Atrium-Ventricular Valve closed, Aortic and Pulmonic Valve opened)

4. *Reduced Ejection:*

Approximately 200 ms after the beginning of ventricular contraction ventricular repolarization occurs. Repolarization leads to a decline in ventricular active tension and pressure generation; therefore, the rate of ejection (ventricular emptying) falls.

(Atrium-Ventricular Valve closed, Aortic and Pulmonic Valve opened)

5. *Isovolumetric Relaxation:*

When the intraventricular pressures fall sufficiently at the end of phase 4, the aortic and pulmonic valves abruptly close (aortic precedes pulmonic) causing the second heart sound (S_2) and the beginning of isovolumetric relaxation. Valve closure is associated with a small backflow of blood into the ventricles and a characteristic notch (incisura or aortic notch) in the aortic and pulmonary artery pressure tracings.

Although ventricular pressures decrease during this phase, volumes do not change because all valves are closed. The volume of blood that remains in a ventricle is called the end-systolic volume and is 50 ml in the left ventricle. The difference between the end-diastolic volume and the end-systolic volume is 70 ml and represents the stroke volume.

(Atrium-Ventricular Valve closed, SemiLunar Valve closed)

6. *Rapid Filling:*

As the ventricles continue to relax at the end of phase 5, the intraventricular pressures will at some point fall below their respective atrial pressures. When this occurs, the AV valves rapidly open and passive ventricular filling begins. Despite the inflow of blood from the atria, intraventricular pressure continues to briefly fall because the ventricles are still undergoing relaxation. Once the ventricles are completely relaxed, their pressures will slowly rise as they fill with blood from the atria.

(Atrium-Ventricular Valve opened, SemiLunar Valve closed)

7. *Reduced Filling:*

As the ventricles continue to fill with blood and expand, they become less compliant and the intraventricular pressures rise. The increase in intraventricular pressure reduces the pressure gradient across the AV valves so that the rate of filling falls late in diastole.

In normal, resting hearts, the ventricle is about 90% filled by the end of this phase.

(Atrium-Ventricular Valve opened, SemiLunar Valve closed)

1.1.3 The vessels

The cardiovascular system's vessels are made up of a closed scheme of tubes that carry blood to all the parts of the body and back to the heart. The first distinction that could be done is between those that move blood from the heart to the body, the arteries, and the ones that move back the de-oxygenated blood to the central organ, the veins. Figure 1.4 reported this vessels categorization.

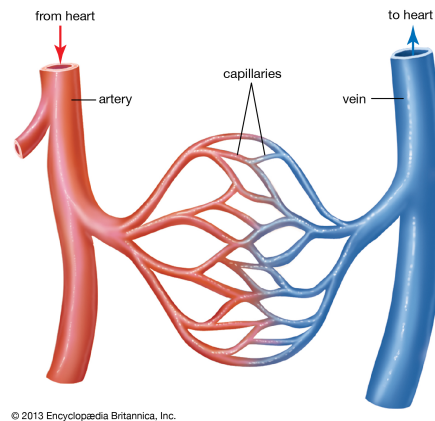


Figure 1.4: Blood flows from the heart through arteries and into capillaries. It then returns to the heart through veins [1].

Arteries carry blood to the body's tissues at high pressure, exerted by the pumping action of the heart. The heart forces the blood into these elastic tubes, which chase each other, sending the blood in pulsating waves. It is therefore imperative that the vessels possess strong and elastic walls to ensure fast and efficient blood flow to the tissues. This wall are composed by three layers (Figure 1.5): the tunica intima (innermost endothelium covered with a surface of elastic tissue), the tunica media (smooth muscle cells blent with elastic fibers, the smaller the artery the less the elastic part amount) and the tunica adventitia (the strongest of the three, composed by collagenous and elastic fibers, it protects the vessel from overexpansion).

When the arteries decrease their diameter they become *arteriole*, characterized by a progressive thinning of the vessel wall and a decrease in the size of the lumen, or passageway. They still have the tunica intima (with a thinner layer of elastic fibers), the tunica media no loger has ekastic but only muscle fibres and the tunica adventitia is exclusively made by connective tissue elements.

The small arteries and arterioles act as control valves through which blood is released into the *capillaries*. The strong muscle wall is able to close the passage or allow it to expand to several times its normal size, thus greatly altering the

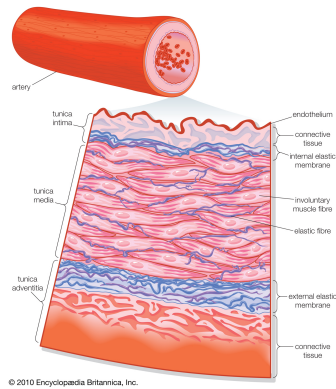


Figure 1.5: Transverse section of an artery [1].

blood flow to the capillaries. Blood flow is from this retroactively controlled system directed to the tissues that require it the most. As the size of the arterioles decreases, the three layers become less and less defined, until the microscopic capillary tubules are made up of a single layer of endothelium which is a continuation of the innermost lining cells of arteries and veins.

In the thin capillaries the exchange between the inside oxygen and the tissue carbon dioxide happens. From this, the capillaries converge again forming *venules*. They are made by an endothelial tube supported by a small amount of collagenous tissue and, in the larger venules, by a few smooth muscle fibres as well. As they increase their size, they start to have a wall structure similar to the arteries one, albeit much thinner.

The *veins* are the last part of the blood vessel path and their function is to carry blood from peripheral tissues to the heart. They have only one endothelial lining, surrounded by the middle tunica and with less muscle and elastic tissue than the arterial wall. In addition, the adventitious tunic is mainly made of connective tissue. The blood pressure in these vessels is extremely low compared to that in the arterial part of the system and the blood has to go out at an even lower pressure. This creates the need for a special mechanism to keep the blood moving as it returns to the heart. To achieve this, many veins have a unique valve system. These valves, formed by semilunar folds in the tunica intima, are present in pairs and serve to direct blood flow to the heart, particularly upward (more are found in the veins of the extremities than anywhere else in the body). Veins are more distensible than arteries, and their walls are built to allow them to expand or contract. They tend to follow a course parallel to that of arteries but are present in greater numbers. Their channels are larger than those of the arteries and their walls are thinner.

The *aorta* is the largest vessel in the systemic circuit, which arises from the left ventricle and carries blood from the heart to all organs and other structures in the body. It has three regions: the ascending aorta, the arch of the aorta and the descending aorta; the latter can be further subdivided into thoracic and abdominal aorta. The aorta emerges from the heart as the ascending aorta, turns to the left and arches over the heart (the aortic arch) and passes downward as the descending aorta (Figure 1.6]). The three main arteries branch off from the aortic arch and give rise to additional branches that supply oxygenated blood to the head, neck, upper limbs and upper body. The descending aorta flows along the posterior center of the trunk past the heart, lungs, and esophagus, through an opening in the diaphragm and abdominal cavity.

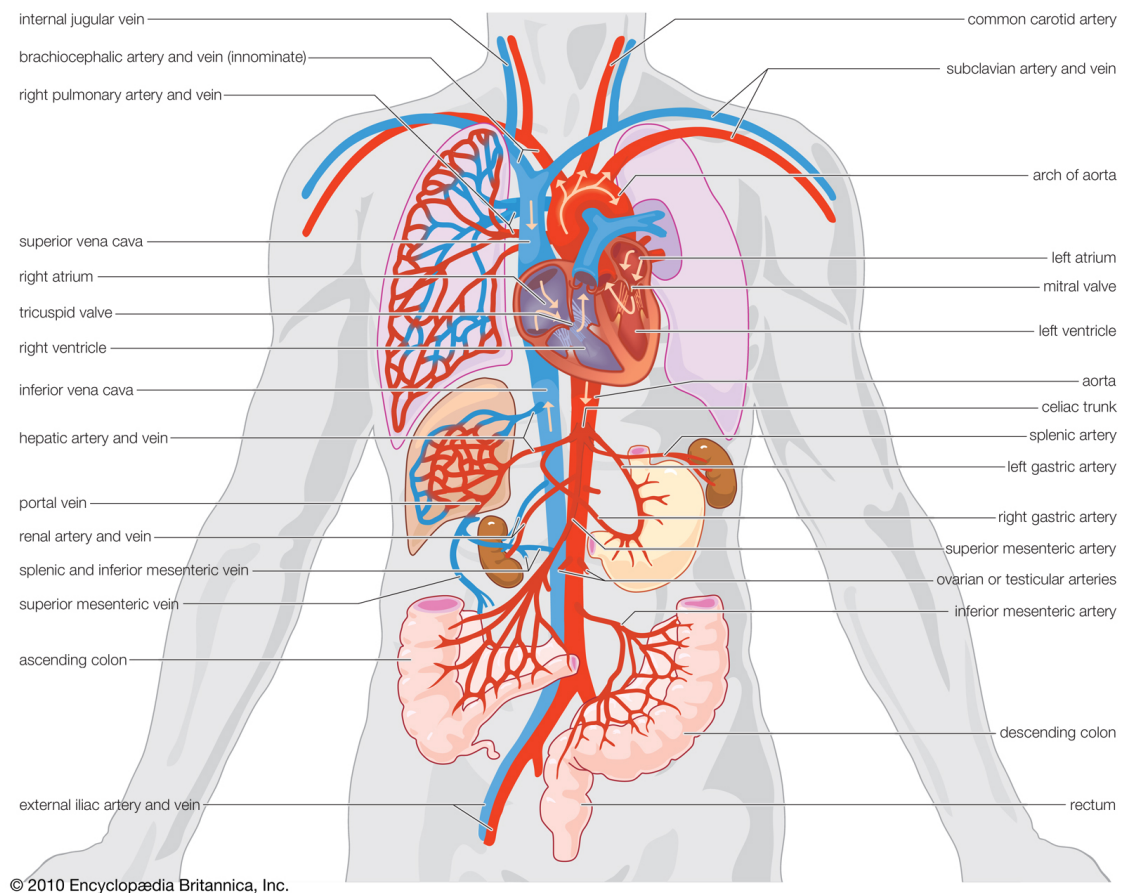


Figure 1.6: Parts of the human circulatory system that highlight arterial supply and venous drainage of the organs [1].

1.1.4 Arterial Blood Pressure and Hypertension

As the left ventricle expels blood into the aorta, the aortic pressure increases. The maximum aortic pressure after expulsion is called *systolic pressure*. As the left ventricle relaxes and fills, the pressure in the aorta decreases. The lowest pressure in the aorta, which occurs just before the ventricle expels blood into the aorta, is called *diastolic pressure*. When blood pressure is measured using a sphygmomanometer, the upper value is the systolic pressure and the lower value is the diastolic pressure.

Normal systolic blood pressure is <120 mmHg and normal diastolic blood pressure is <80 mmHg. The difference between systolic and diastolic blood pressure is the aortic pulse pressure, which is typically between 40 and 50 mmHg. The trend of the aortic pressure variation for each cardiac cycle is shown in Figure 1.7.

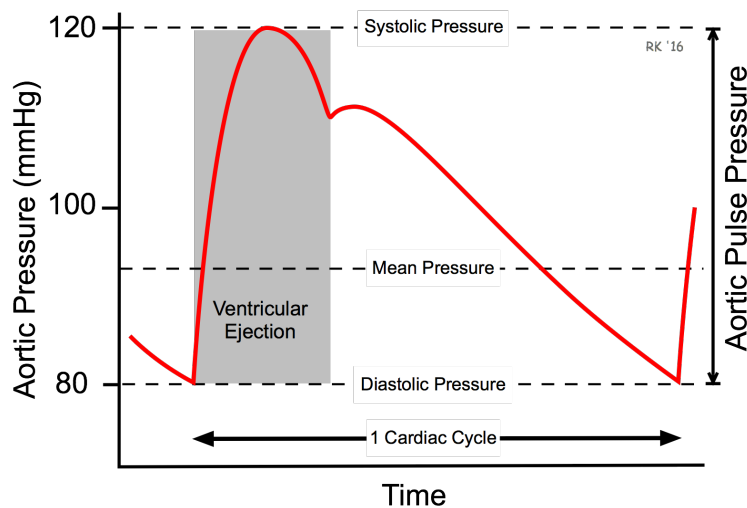


Figure 1.7: Aortic pulse pressure variation during one cardiac cycle [3].

Hypertension

An high value of blood pressure is termed "*Hypertension*" and it is a pathological status that afflicts a lot of people, more than one billion worldwide and it is more often a "silent killer" causing morbidity and mortality. This epithet comes from the asymptomaticity related to this illness that takes place until the damaging effects appear (such as stroke, myocardial infarction, renal dysfunction, visual problems, etc.). In fact, Hypertension is a major risk factor for coronary artery disease, myocardial infarction ("heart attacks") and stroke.

In the "European Society of Cardiology and Hypertension guidelines" are defined all the criteria to identify and classify this pathology, included the threshold blood pressure values. The last update of this document was drawn up in 2018 ([4]) and in Tab. 1.1 all the categories are summarized.

Table 1.1: Classification of office blood pressure and definitions of hypertension grade in adults (2018 ESH Guidelines, [4])

Category	Systolic (mmHg)		Diastolic (mmHg)
Optimal	< 120	and	< 80
Normal	120-129	and/or	80-84
High Normal	130-139	and/or	85-89
Grade 1 hypertension	140-159	and/or	90-99
Grade 2 hypertension	160-179	and/or	100-109
Grade 3 hypertension	≥ 180	and/or	≥ 110
Isolated systolic hypertension	≥ 140	and	≥ 90

The threshold values reported in Tab. 1.1 are given to easily address in the practice the diagnosis and the decision about treatment. Hypertension is characterized by the level of Blood Pressure (BP) at which the benefits of treatment (either with lifestyle interventions or drugs) unequivocally outweigh the risks of treatment. It is defined as office Systolic Blood Pressure (SBP) values above 140 mm Hg and/or and Diastolic Blood Pressure (DBP) values 90 mm Hg. Moreover, from this different levels of severity could be distinguished (grade 1, grade 2 and grade 3). The more is the hypertension asperity, the more the cardiovascular and renal risk associated [4].

1.2 Analyzed Biological Signals

In this section all the signals analyzed during this p.h.D work will be explained. The common denominator they have is about the detection of the cardiac pulse, resulting from the ejection of the left ventricle that spreads through the body and its relative track. On the opposite, they mainly differ for the transduction principle used to monitor the pulse through electric, optical, sound or strain detection.

1.2.1 Electrocardiogram Signal

An Electrocardiogram Signal (ECG) is produced measuring how the electrical activity of the heart changes over time: action potentials within each cardiac cell propagate throughout the heart becoming a whole during each cardiac cycle. The

ECG provides specific waveforms of electric potential differences when the atria and ventricles depolarize and repolarize.

In particular, during the heart cycle, one part of the cardiac tissue is depolarized and another part is at rest, or polarized (as discussed in par. 1.1.2). This results in a charge separation, or dipole. The moving dipole causes current flow in the surrounding body fluids between the ends of the heart, resulting in fluctuating electric fields throughout the body. Electrodes on the surface of the skin detect the voltage of this electrical field, which gives rise to the electrocardiogram [5].

As an ECG is recorded, a signal of voltage versus time is produced, which is normally displayed in millivolts (mV) versus seconds. A typical ECG waveform is shown in Figure 1.8. For this recording, the negative electrode was placed on the right wrist and the positive electrode placed on the left ankle. In this way it is possible to observe a series of peaks and waves that correspond to ventricular or atrial depolarization and repolarization, with each segment of the signal representing a different event within the cardiac cycle.

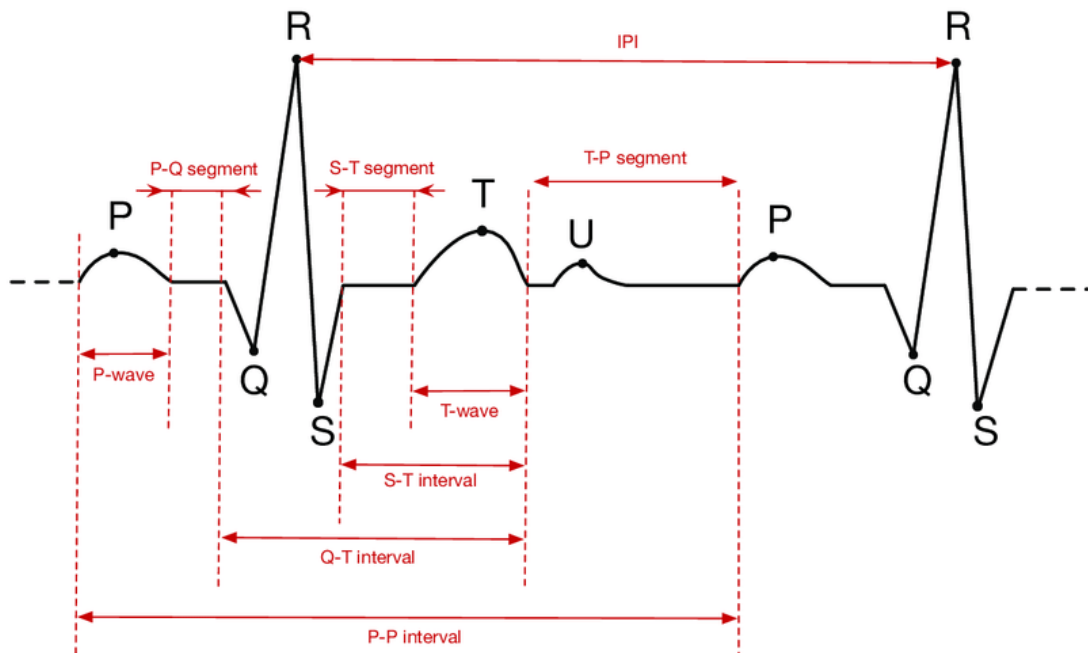


Figure 1.8: A typical electrocardiogram (ECG) signal and its main features: peaks (P, Q, R, S, T, U), waves, segments and intervals. IPI, Inter-Pulse Interval [6]

The cardiac cycle begins with the firing of the sinoatrial node in the right

atrium. This firing is not detected by the ECG because the sinoatrial node is not composed of an enough large quantity of cells, these do not create an electrical potential big enough to be recorded by distal electrodes.

The depolarization of the sinoatrial node is conducted rapidly throughout both the right and the left atria, giving rise to the *P-wave* (Figure 1.8). This represents the depolarization of both atria and the onset of atrial contraction; the P-wave lasts normally around 80–100 milliseconds.

As the P-wave ends, the atria are thus depolarized and this corresponds to the beginning of contraction. The signal then returns to baseline while action potentials (not large enough to be detected) spread through the atrioventricular node and bundle of His. Then, roughly 200 ms after the beginning of the P-wave, the right and left ventricles begin to depolarize resulting in the recordable *QRS complex*, which lasts approximately 100 ms (Figure. 1.8). The first negative deflection (if present) is the Q-wave, the large positive deflection is the R-wave, and if there is a negative deflection after the R-wave, it is called the S-wave. As the QRS complex ends, the ventricles are completely depolarized and begin the contraction. It has to be noticed that the exact shape of the QRS complex depends on electrodes displacement used for signals recording.

Simultaneous with the QRS complex, atrial contraction has ended and the atria are repolarizing. However, the effect of this global atrial repolarization is sufficiently masked by the much larger amount of tissue involved in ventricular depolarization, and so it is not normally detected in the ECG. Toward the end of ventricular contraction, the ECG signal returns to baseline. The ventricles then repolarize after contraction, giving rise to the *T-wave*. The T-wave is normally the last detected potential in the cardiac cycle, thus it is followed by the P-wave of the next cycle, repeating the process (Figure 1.8).

The ECG is typically acquired with electrodes placed directly on the skin surface and then the potential difference between them is evaluated. The characteristics of the detected waveform depend not only on the amount of cardiac tissue involved, but also on the electrodes orientation, referred to the major dipoles in the heart. In fact, ECG waveform will shape different depending on varying different electrode positions and number of electrodes involved. Typically, an ECG is obtained using a number of different electrode locations (e.g. limb leads or precordial) or configurations (unipolar, bipolar, modified bipolar), which have been standardized by universal application of certain conventions [5]. Different configurations for electrocardiogram acquisition are shown as follow.

Bipolar limb leads

Bipolar recordings use the standard limb lead configurations shown in Figure 1.9a. All these sets up are based on an established equilateral triangle (traced between the shoulders and the bottom chest, with the heart in the center) and called the *Einthoven triangle* in honor of Willem Einthoven, who developed the electrocardiogram in the early 1900s. In this, three main configurations could be distinguished.

Lead I measures the potential difference between the two arms and, by convention, it has the positive electrode on the left arm and the negative electrode on the right. In this and the other two limb leads, an electrode on the right leg acts as a reference electrode for recording purposes (summarized by the expression 1.1).

$$V_{LA} - V_{RA} = V_I \quad (1.1)$$

The other two bipolar limb configuration differ from the positive and negative voltage electrode position. In the *lead II* configuration, the positive electrode is on the left leg and the negative electrode is on the right arm (equation 1.2).

$$V_{LL} - V_{RA} = V_{II} \quad (1.2)$$

Meanwhile, *Lead III* has the positive electrode on the left leg and the negative one on the left arm (formula 1.3).

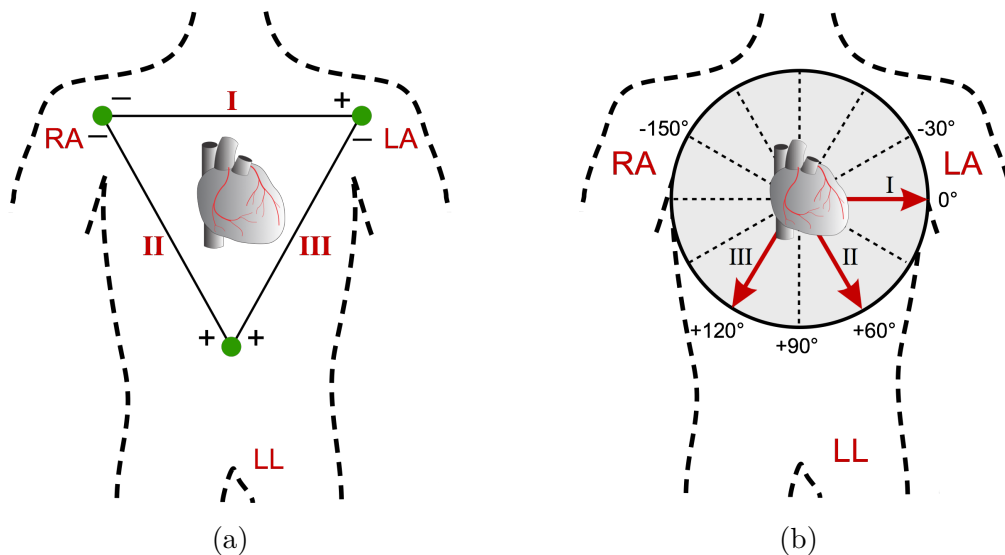


Figure 1.9: (a) The Einthoven's Triangle; (b) Axial reference system for the bipolar limb leads [3].

$$V_{LL} - V_{LA} = V_{III} \quad (1.3)$$

If the limb cables are attached to the extremity of the limb (wrists and ankles) or at the origin of the limb (shoulder or thigh) makes no significant differences in the recording. Indeed, the limb can simply be seen as a long thread coming from a point on the trunk of the body.

If the three limbs of Einthoven's triangle (assumed to be equilateral) are disunited the positive electrode for lead I is said to be at zero degrees relative to the heart (along the horizontal axis between LL and RA (see Figure 1.9b). Similarly, the positive electrode for lead II (RA-LL axis) will be $+60^\circ$ relative to the central organ, and the positive electrode for lead III (LA-LL axis) will be $+120^\circ$ relative to the heart as shown to the right. This new construction of the electrical axis is called *the axial reference system* [3]. With this system, a wave of depolarization traveling at $+60^\circ$, as the peak QRS does, produces the greatest positive deflection in lead II. For this reason also if all the derivations let to have a quite good ECG signal, the one commonly used is the II, in which the QRS complex results to be emphasized.

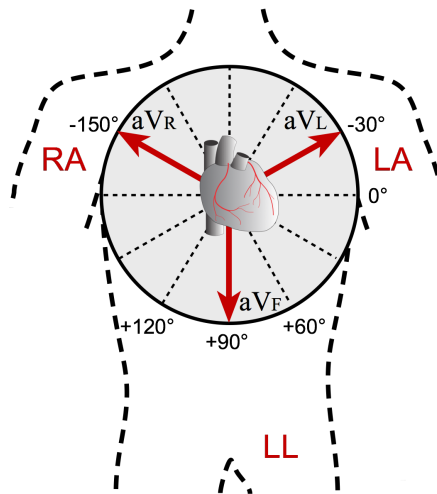


Figure 1.10: Electrocardiogram augmented limb leads [3].

Unipolar Augmented limb leads

Besides the previous bipolar configurations, there are other unipolar ones. Where the term "unipolar" implies that there is one single positive electrode referred against a combination of the other limb electrodes. Also in this case, as for the

bipolar, the electrodes are located on the left arm (aV_L), the right arm (aV_R) and the left leg (aV_F).

Using the axial reference system, these three are located relatively to the lead I axis (see Figure 1.10): the (aV_L) at -30° , the (aV_R) at -180° and the (aV_F) at $+90^\circ$. Each one better accentuates that depolarization that occurs along its direction.

The three augmented unipolar leads, coupled with the three standard bipolar limb leads (Figure 1.2.1), comprise the six limb leads of the ECG that let to record the heart electrical activity on the *frontal plane*.

Unipolar chest leads

Besides the three standard limb leads (Paragraph 1.2.1) and the three augmented limb leads (Paragraph 1.2.1), by convention, there are six precordial, unipolar chest leads. This configuration places six positive electrodes on the chest surface over different regions of the heart in order to record electrical activity in a plane perpendicular to the frontal plane, the *transverse plane*. These six leads are named $V_1 - V_6$. Also in this case, as well for the previous, a wave of depolarization traveling toward a particular electrode on the chest surface will elicit a positive deflection.

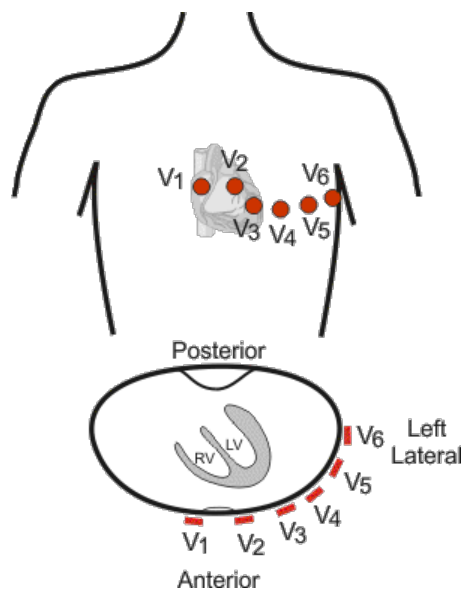


Figure 1.11: Unipolar chest leads configuration.

The six positive electrodes are placed for their definition in this positions (as depicted in Figure. 1.11):

- V_1 : fourth intercostal space at the right sternal margin;
- V_2 : fourth intercostal space at the left sternal margin;

- V_3 : between V_2 and V_4 ;
- V_4 : fifth intercostal space on the mid-clavicular line;
- V_5 : fifth intercostal space on the anterior axillary line;
- V_6 : fifth intercostal space on the mid-axillary line.

In summary, the chest leads provide a different view of the electrical activity within the heart. Therefore, the waveform recorded is different for each lead compared to the limb leads.

1.2.2 Photoplethysmogram Signal

The term *plethysmograph* has Greek origin, it is the merge between "*plethysmos*", increase, and "*graph*", that means write. As a matter of fact, it results to be an instrument mainly used to determine and register blood volume variations in the body (blood flow), that occur every heartbeat.

There are various types of plethysmograph and they differ in the way used for the volume changes detection. In particular, several transducer could be used depending on the application target: water, air, strain gauge, impedance, and photoelectric. In the biomedical field, the most common used is the photoelectric plethysmography, also known as PhotoPlethysmoGram Signal (PPG). Compared to the others, it presents two main advantages: the usage simplicity and the cost-effectiveness. Moreover, it does not need direct contact with the skin surface, as the other plethysmograph methods [7].

The low-cost and simplicity of this optical technology has been offering significant benefits to healthcare, starting from the sport monitoring in health subjects (consumer application) to the clinical diagnosis in hospitalized patients (e.g. in primary care where non-invasive, accurate and simple-to-use diagnostic techniques are desirable).

The PPG uses a probe which contains a light source and a detector to identify cardiovascular pulse wave, that propagates by way of the body. Light, travelling through biological tissue, is absorbed by different substances: pigments in the skin, bone, and arterial or venous blood. The most of them do not generate a variation of the absorbed light amount, but contribute to create the static PPG value (offset). Whereas, the arterial blood has a quantity of absorption that is directly dependent on the hemoglobin amount (related to the oxygen, in turn), that creates the dynamic pulse rhythmicity. For this, the PPG signal reflects the blood movement in the vessel, which goes from the heart to the detection point through the blood

vessels in a wave-like signal (see Figure 1.12). The point used to do measurement could be fingertips, toes, earlobes, forehead or many others in proximity to a vessel.

In other words, it is an optical measurement technique that, using a light sent into the tissue, measures the amount of back-scattered light, strictly linked to the variation of blood volume.

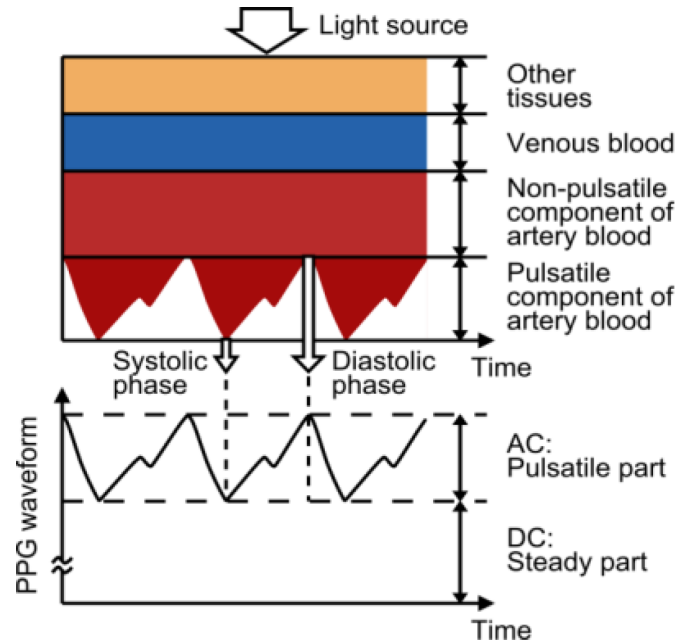


Figure 1.12: Components composing the PhotoPlethysmoGram [8].

As already discussed, the photoplethysmogram probe is made by a light source and a photodetector (photodiode or phototransistor): the former illuminates the tissue (e.g. skin) and the latter measures small variations in light intensity, associated with changes in vessels blood volume. The more the blood volume, the less the light intensity detected and vice versa.

Three different light sources could be used: green with $\lambda = 535$ nm, red with $\lambda = 660$ nm and infra-red with $\lambda = 990$ nm. A higher wavelength lets light to deeply penetrate into the tissue, increasing the possibility to detect not only superficial vessels.

A PPG waveform (Figure 1.12) consists of two parts [8]:

- The *DC component* is correlated with the detection of transmitted or reflected optical signal from both the tissue structure and the mean volume between arterial and venous blood. It undergoes also slow variation corresponding to

the subject breathing;

- The *AC component* shows blood volume changes that occur throughout systolic and diastolic phases of the cardiac cycle. Its fundamental frequency depends on heart rate and is superimposed onto the DC component.

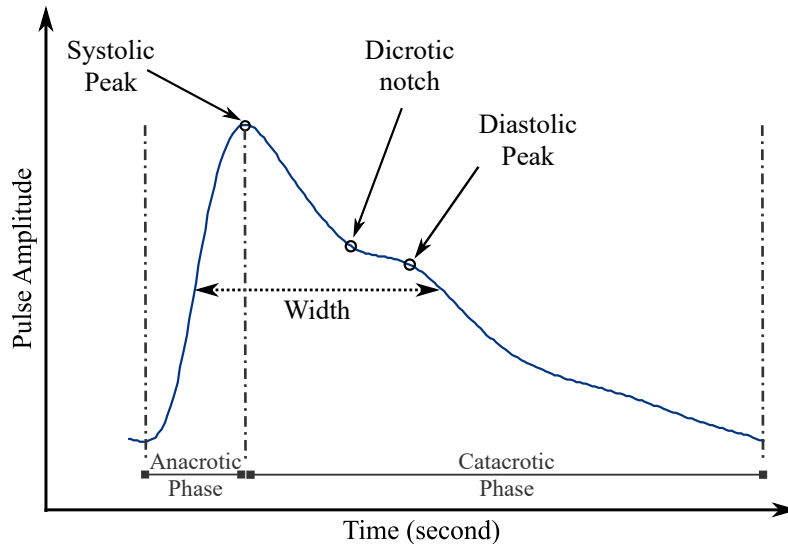


Figure 1.13: A typical waveform of the PPG and its characteristic parameters.

This signal is affected by heartbeat, haemodynamics and physiological condition caused by changes in arteriole properties. All these physiological parameters could change PPG wave profile. The usual profile is shown in Figure 1.13. PPG pulse is commonly divided into two steps: an anacrotic phase and a catacrotic phase. The *anacrotic phase* is the rising edge of the pulse and it is primarily concerned with systole, whereas the *catacrotic phase* is the falling edge of the pulse due to diastole and wave reflections from the periphery. A *dicrotic notch* (Figure 1.13) could be usually seen in the catacrotic phase for subjects with healthy compliant arteries.

Many cardiovascular features could be extracted from PPG signal:

- *Systolic amplitude*: indicator of pulsatile changes in blood volume caused by arterial blood flow around the measurement site;
- *Peak to peak interval*: distance between two consecutive systolic peaks (the R-R interval in the ECG signal correlates closely with the Peak-Peak interval as both represent a completed heart cycle);
- *Pulse area*: the total area under the PPG curve;
- *Pulse interval*: the distance between the beginning and the end of the PPG waveform.

1.2.3 Phonocardiogram Signal

PhonoCardioGram Signal (PCG) is an accurate recording plot of sounds and murmurs made by the heart during a cardiac cycle. With the term "heart sounds" are included all the audible tones generated by the contraction and relaxation of atria and ventricles, the valve movements and the blood flow.

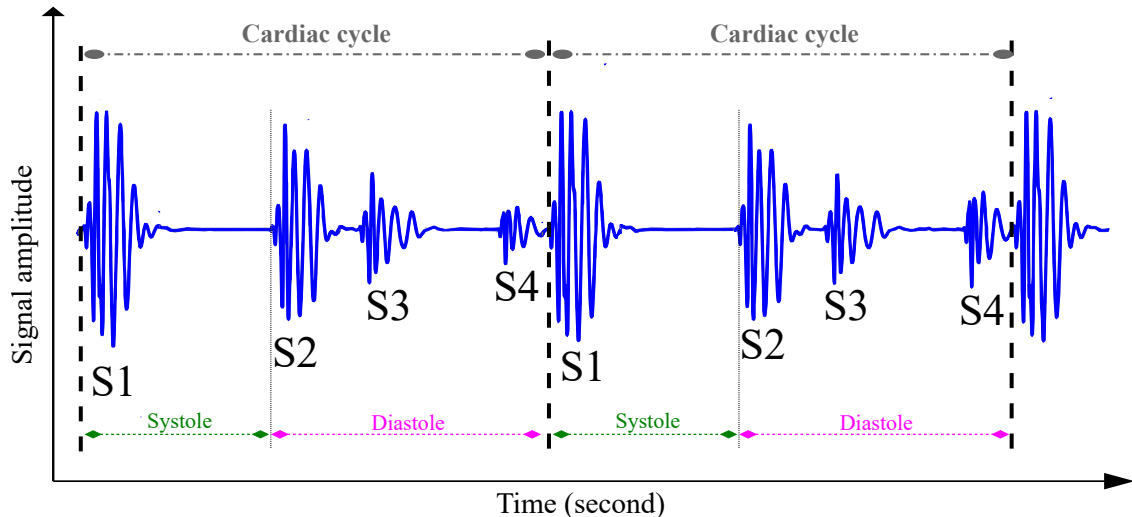


Figure 1.14: PCG heart sound signal components and correlation with the cardiac cycle phase.

The two main components of the cardiac acoustic signal, those that are always detectable, are the first heart sound (S1) and the second heart sound (S2) [9]. There are then other secondary components, the waves S3 and S4, audible if the acquisition is conducted in good conditions (low level noise and high quality of the used instrument) and usually in young people. Figure 1.14 displays a typical PCG signal with its components underlined.

Usually, this signal is not clean as the one previously shown, a phenomenon called pathological *murmurs* could be heard in case of turbulent flow or valve narrowing. This occurrence is the most common abnormal behaviour recorded in the heart. It is possible to distinguish this sound from the normal one because it has a longer duration and is much noisier. Turbulences could also be caused by other behaviours, such as local obstructions, diameter variations or valve insufficiency.

S1 occurs at the onset of the ventricular contraction, during the closure of the AV valves. It contains a series of low-frequency vibrations, and is usually the longest and loudest heart sound. The audible sub-components of S1 are those

associated with the closure of each of the two AV-valves.

S2 is heard at the end of the ventricular systole, during the closure of the semilunar valves. Typically, its frequency is higher than *S1*, and its duration is shorter. It has aortic and pulmonary sub-components.

A third low-frequency sound (*S3*, ventricular gallop) could be heard at the beginning of the diastole. It is generally agreed that *S3* is associated with the over distention of the ventricle during the rapid filling phase: the rapidly distending ventricle reaches a point when its distention is checked by the resistance of its wall, causing audible vibrations. While, in late diastole, during atrium contraction, a fourth heart sound (*S4*, atrial gallop), may be detected.

PCG is included from 10 to 400 Hz in frequency range. *S1* has components in 10 to 140 Hz bands, *S2* has higher components in 10 to 400 Hz. The two last components, *S3* and *S4*, are barely detectable with direct auscultation, usually they come out with secondary signal editing (filtering and signal amplification). This happens because human ear is more sensitive to frequencies included in speech range (1000 to 2000 Hz), so these sounds are primarily low-frequency vibrations that are too weak to be heard. This is the reason why digital recording and analysis of these vibrations may produce information that cannot be perceived by the physician's ear.

These sounds are of short duration and highly non-stationary, i.e. their frequency properties vary with time. The transmission of the sound through the thorax depends on the properties of the body (chest wall thickness, layers of fat) and the complexity of auscultation gives to the signal low intensity. The sounds may be recorded differently on several locations, sometimes including overlapping components. The properties of the transducer (e.g. frequency response) may also significantly affect the recorded signal.

1.2.4 Arterial Pulse

Arterial system is the network of vessels that delivers the oxygenated blood to the peripheral organs and tissues, as said in Paragraph 1.1.3. The blood flow is sustained by the heart, which behaves like a pump. In this context, the arterial tree contributes to convert the pulsating flow from the heart to a continuous capillary flow. Several levels of elasticity can be found along the different vessel path: aorta is very elastic, while femoral and radial arteries are more muscular. The more elastic the vessel, the higher the volume of blood that can be accommodated for a small rise in pressure.

Concerning this complex vascular system and its principal aim, the recording obtained with a pulse transducer placed externally, over the carotid artery, is known

as Arterial Pulse, or Wave Pulse, or Sphygmic Wave. It has a contour and shape very similar to a pressure curve obtained through a catheter placed internally in the carotid artery and recorded with a strain gauge manometer system. In fact, as depicted by the Laplace Law (equation 1.4), the wall tension for a thin-walled cylindrical shell, is directly related with the pressure inside.

$$Tension \propto P(Pressure) * R(Radius) \quad (1.4)$$

Moreover, if the wall has a thickness, as the arteries under investigation have, the tension becomes inversely related also to the vessel thickness (equation 1.5).

$$Tension \propto \frac{P(Pressure) * R(Radius)}{2h(wallthickness)} \quad (1.5)$$

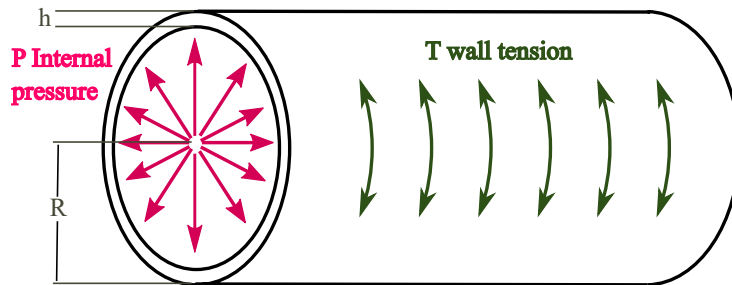


Figure 1.15: Characteristics of a cylindrical shell that influence the wall tension.

In particular, there are three different factors that could influence Pulse Wave value: volume of blood flow, pressure in the vessel and reflection of the peripheral waves. The similarity of the externally sensed carotid pulse tracing and the internally detected pressure curve is due to the dominance of pressure pulse effect on the tension of the vessel wall for the greater part of the cardiac cycle.

This signal changes its contour depending on the vessel under investigation and the related arterial impedance characteristics: resistance, inertia, and compliance. The first, resistance, is associated to blood viscosity and the geometry of the vasculature. The second, inertia, is connected to the mass of the column of blood, and the last, compliance, is related to the distensibility of the vascular walls. Since ejection of the major portion of the stroke volume takes place in the early and mid-systole, the cause of major change in tension in early and mid-systole is a result of changes in both volume and pressure [10]. During the last part of systole and during diastole, however, the predominant effect must be primarily due to changes in pressure, although volume may also play a role. Generally, as reported in Figure 1.16, the DBP and mean blood pressure are relatively constant in the arterial system, but systolic blood pressure increases in the direction of the

peripheral circulation.

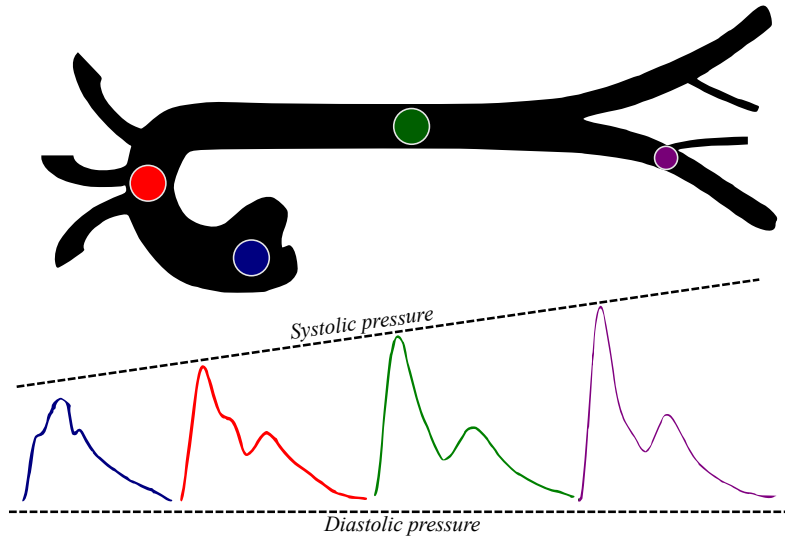


Figure 1.16: Pulse pressure amplification in the arterial system, from the center to the periphery.

Hence, depending on the artery used for the variation in superficial tension detection, several pulse shapes can be sensed. But, whichever is the exacted wave, these all have always three different phases that can be identified:

- *Percussion wave* (from P_d to P_s): initial systolic portion of the pressure pulse;
- *Tidal wave* (starting from P_i): later systolic portion of the pressure pulse;
- *Dicrotic Wave*: wave following the *dicrotic notch* (roughly corresponding to the timing of second hearth sound) and therefore diastolic.

Figure.1.17 represents these time periods referred to the carotid signal and compared with the related aortic pressure variation.

All the biological signals analyzed in this chapter (Electrocardiogram, Photoplethysmogram, Phonocardiogram, and the Arterial pulse) have been used in this project with the purpose of identifying the blood pulse passage. Some of them, like the Arterial Pulse and the Photoplethysmogram describe this phenomenon using a different method of transduction but resulting in a similar signal shape. Chosen a vessel, the Pulse Wave detects variation in superficial tension, whereas the PPG the quantity of absorbed light.

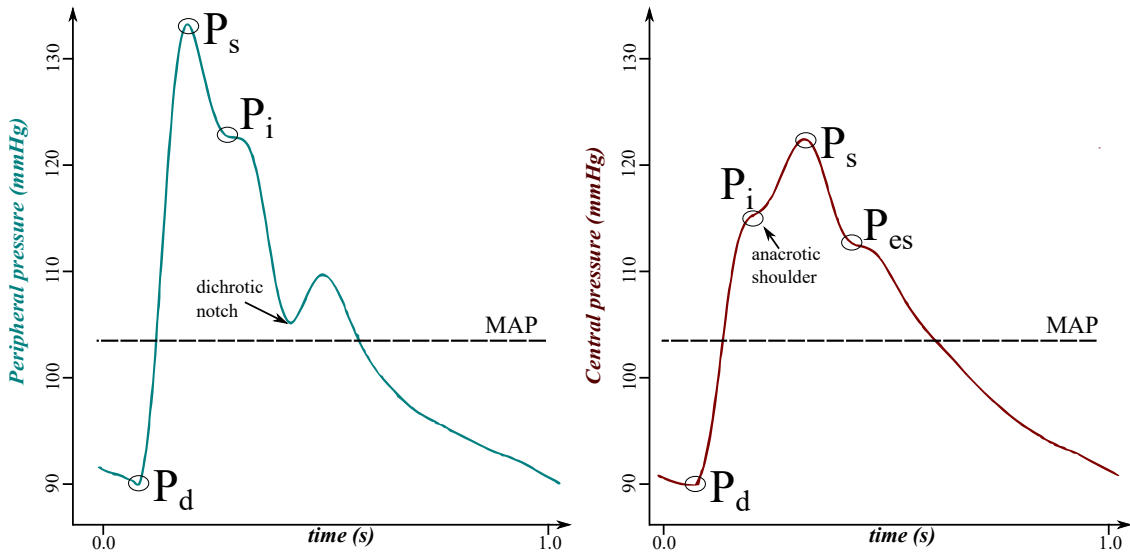


Figure 1.17: Features of the radial pulse wave and corresponding central aortic pressure wave (P_d is DBP, P_s means SBP, P_i corresponds to inflection point, and P_{es} stays for incisura).

1.3 Pulse Wave Velocity

Cardiovascular Diseases (CVDs) are a group of illnesses that involve both the heart and the circulatory system. A strictly correlated parameter with the state of the cardiovascular system is the large arterial stiffness [11]. This has become one of the most important classifiers for cardiovascular pathologies. Particularly, the arterial stiffness is bonded with the elastic properties of the vessels, and it plays an essential role with the systolic blood pressure. In turn, a high arterial stiffness could lead to cardiac hypertrophy and arterial lesions [12], [13]. Nowadays, several methods have been addressed to quantify arterial stiffness using a noninvasive approach [14]–[16].

One way to assess the elastic property of the arterial tree is the Pulse Wave Velocity (PWV), that corresponds to the velocity at which blood pulse propagates through the cardiovascular system. The higher the PWV, the stiffer the blood vessel walls. Moreover, for the first time in 2007 (last update in 2018, [4]), in the European Society of Cardiology and Hypertension guidelines appeared the PWV as a significant predictor of cardiovascular risk stratification and useful for identifying asymptomatic organ damage (OD).

This velocity could be evaluated considering any two sites of the cardiovascular system but, according to the “Expert consensus document on arterial stiffness”,

the carotid-femoral PWV (cfPWV) is the noninvasive gold standard for this type of measurement [17]. Indeed, with the cf-PWV, there is the possibility to evaluate the aorta's elasticity, which is the most susceptible, among all arteries, to undergo changes in response to risk factors and aging [18].

In the clinical noninvasive cf-Pulse Wave Analysis, the two sites associated with the heart blood ejection action on each cardiac cycle are the carotid pulse, close to the neck, and the femoral pulse, located midway between the anterior superior iliac spine and the symphysis pubis. A specific distance d separates these sites, which corresponds to the path length through the arterial tree. It is approximately estimated with the direct measure of the distance between proximal and distal points. The time needed by the pulse to propagate between these two sites is called the delay or Pulse Transit Time (PTT). The PWV parameter is computed as the linear ratio between d and the PTT, as in Equation 1.6.

$$PWV = \frac{\text{distance}}{\text{pulse}_{\text{distal}}(\text{time}) - \text{pulse}_{\text{proximal}}(\text{time})} = \frac{d}{PTT} \quad (1.6)$$

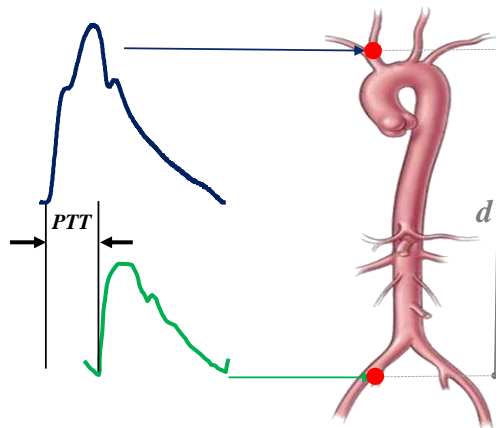


Figure 1.18: Non-invasive Pulse Wave Velocity assessment.

Many different pulse waveforms have been used to assess PWV, such as pressure wave, distension wave or flow wave. Usually, the points and the signals used to calculate Pulse Wave Velocity are different for medical or commercial devices with this purpose. According to the commercial, as proximal point is considered straight heart, with the ECG, and for proximal measurement the PPG at finger. On the other hand, the medical method considers the two systolic foos of carotid Pulse Wave, considering this as proximal, and femoral Pulse Wave, as distal (Figure 1.18).

Typical values of PWV are from 5 to 10 m/s and the cut-off value for the CV risk assessment is set at 10 m/s. Besides the pathological condition, according to the "Reference Values for Arterial Stiffness" [19], the PWV varies both with the age and with the blood pressure. Indeed, the elder is the subject the more is the BP values change. Table 1.2 reports the typical PWV depending on the age for a healthy population.

Table 1.2: Distribution of pulse wave velocity (m/s) according to the age category in the normal values population, [19]

Age Category	Mean ($\pm SD$)	Median (10-90 pc)
<30	6.2 (4.7-7.6)	6.1(5.3-7.1)
30-39	6.5 (3.8-9.2)	6.4 (5.2-8.0)
40-49	7.2 (4.6-9.8)	6.9 (5.9-8.6)
50-59	8.3 (4.5-12.1)	8.1 (6.3-10.0)
60-69	10.3 (5.5-15.0)	9.7 (7.9-13.1)
≥ 70	10.9 (5.5-16.3)	10.6 (8.0-14.6)

SD stays for standard deviation; pc means percentile

Meanwhile, in the following graphics is report the correlation between PWV, age and the blood pressure respectively (Figure 1.19).

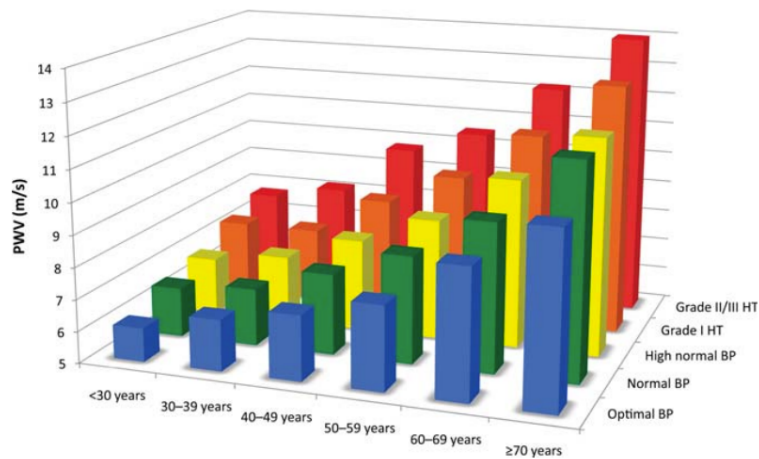


Figure 1.19: Reference values for pulse wave velocity (PWV): mean values according to age and blood pressure (BP) categories. HT, hypertension [19].

1.3.1 Evaluation methodology and Commercial Devices

Nowadays, several devices exist to assess this cardiovascular parameter, as thoroughly reviewed by Nabeel, P. M., et al. [20]–[22]. They differ for the methodology and the procedure used to evaluate the PWV.

Regarding the methodology, typically the most used and reliable approach is the applanation tonometry, followed by cuff-based oscillometry [23], ultrasound [24] and optical sensors [25]. Instead, the procedure comprises the actions needed by the instrument's user to address the PTT evaluation, and it depends on the presence of the electrocardiogram (ECG) signal in the system. Basically, two types of PWV extraction could be distinguished: the one-step and the two-steps methods (Figure 1.20).

The *two-steps method* involves both the ECG and arterial pulse signals. In the first phase, the time employed by the blood pulse to propagate from the heart (ECG reference) to the carotid (pulse detection) is taken as carotid Pulse Transit Time (cPTT). Then, in a second moment, the propagation time from the heart (ECG reference) to the femoral site (pulse detection) is recorded as femoral Pulse Transit Time (fPTT). Finally, the PTT considered for the PWV evaluation is the difference between the two acquired intervals (cfPTT= fPTT - cPTT).

On the other hand, the *one-step method* consists of a single simultaneous acquisition of the pulse wave on carotid and femoral sites, without the ECG's need, so directly evaluating the differential PTT.

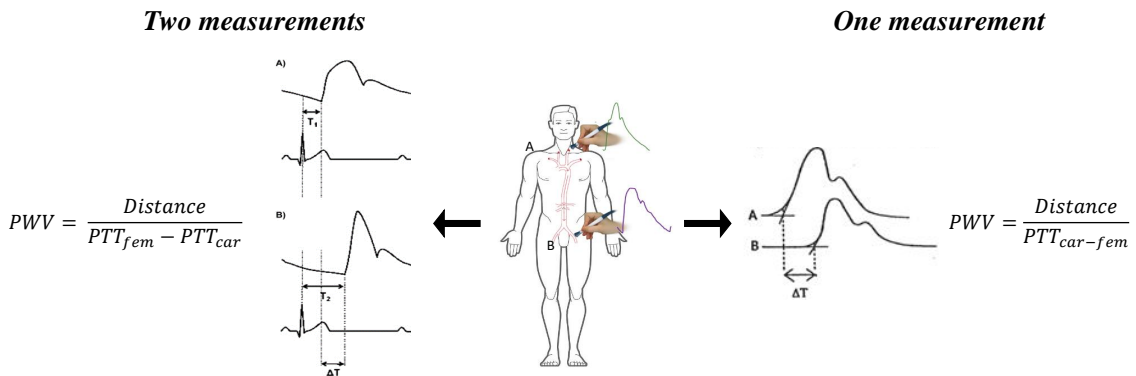


Figure 1.20: PWV assessment through the two possible methods.

Concerning the clinical extraction of the pulse wave velocity, many devices are available in the medical segment.

Sphygmocor

SphygmoCor (AtCor Medical, Sydney, Australia) is considered as the gold-standard to measure PWV non-invasively. It analyses the pulse wave of carotid and femoral arteries, estimating the delay with respect to the ECG wave. SphygmoCor (Figure 1.21) offers the possibility of carotid-femoral PWV measurements in two steps. The first step is used to simultaneously record carotid pulse wave and ECG, while the second step is the recording of femoral pulse wave and ECG. ECG recording during measurements is necessary for synchronization of carotid and femoral pulse wave times. The transit time is determined using the intersecting tangent method. The path length is calculated by subtracting the distance between the carotid artery measurement site and sternal notch (carotid-notch), from the distance between the femoral artery site and the sternal notch (femoral-notch), as it was found in best agreement with invasive measures [26].

SphygmoCor Xcel device (Xcel, Atcor Medical, Australia) is a new SphygmoCor device that allows femoral and carotid signals to be acquired simultaneously. To assess PWV, carotid pulse waves are measured by applanation tonometry, as for the SphygmoCor device. In place of femoral artery tonometry, the Xcel device uses the volumetric displacement waveform obtained from a partially inflated cuff positioned around the upper thigh. The distance is measured from the sternal notch to the carotid site (distance 1), from the femoral artery at the inguinal ligament to the proximal edge of the thigh cuff (distance 2) and from the sternal notch to the proximal edge of the thigh cuff (distance 3). Distance 1 and 2 are then subtracted from distance 3. PWV is then obtained by measuring foot-to-foot transit time (intersecting tangent method) between the carotid pulse and the cuff-acquired femoral pulse and dividing it by the calculated distance [27].

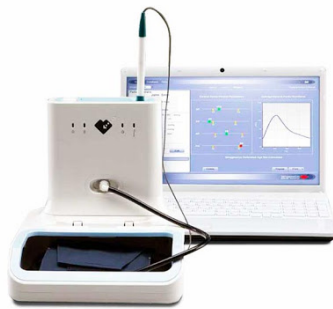


Figure 1.21: Sphygmocor Device [28].

PulsePen

The *PulsePen* (DiaTecne, Italy) is composed of one tonometer and an integrated and ECG unit. The carotid and femoral pulse waves are acquired in two steps by applanation tonometry, both synchronized with the ECG R peak. The foot of the pulse waveform is determined by the intersecting tangent method, and distance is assessed as in SphygmoCor device [29].



Figure 1.22: PulsePen Device [30].

Complior

The *Complior* (Colson, France) uses two dedicated piezoelectric pressure mechanotransducers directly applied to the skin in a simultaneous acquisition of pressure pulses. One probe is positioned at the common carotid artery, the central detection site, whereas the other probe is placed at the femoral artery site. Since the acquisition is simultaneous, no ECG recording is needed. The distance measurement is calculated by a direct superficial measurement, with a tape measure, from the carotid artery to the femoral artery [31].



Figure 1.23: Complior Device [32].

Arteriograph

The main principle of PWV estimation behind *Arteriograph* device (TensioMed, Budapest, Hungary) is to record oscillometric pressure curves based on plethysmography and register pulsatile pressure changes in an artery on the upper arm [33]. *Arteriograph* is equipped with an inflatable cuff placed on the patient's upper arm and inflated 35 mmHg above the subject's SBP (systolic and diastolic BPs are used to calibrate the system). Pressure variation in the cuff influence a pressure receptor and the signal is transferred to a computer. The basis of the technique is the generation of two systolic peaks. First, there is an early peak (P1) created by the ejection of the blood volume from the left ventricle into the aorta. The pressure wave is transmitted to the lower part of the body and the reflected wave from the periphery generates the late systolic peak (P2). The return time (RT) is the difference (in ms) between the first (P1) and the reflected systolic wave (P2) and is related to the stiffness of the aorta. The RT is than related to the distance from the jugulum (Ju) to the symphysis (Sy), resulting in the PWV.

$$PWV = \frac{Ju - Sy(m)}{RT/2(s)} \quad (1.7)$$



Figure 1.24: Arteriograph Device [34].

Vicorder

The *Vicorder* system (Skidmore Medical, UK) is an automatic device that uses an oscillometric technique, whereby proximal and distal inflatable cuffs are placed on areas of interest [35]. To assess carotid-femoral PWV a 30 mm partial cuff is placed over the neck at the level of the right carotid artery, with a larger oscillometric cuff (100 mm wide) placed around the upper part of the right thigh. Distance is measured superficially from the suprasternal notch to the top of the thigh cuff. Pulse waveforms are simoultanesly recorder as the cuff

inflate to 65 mm Hg and the transit time in milliseconds is computed. Transit time is assessed using the maximum second derivative method (an in-built cross-correlation algorithm centered around the peak of the second derivative of pressure).



Figure 1.25: Vicorder Device [36].

pOpmètre

The pOpmètre (Axelife SAS, France) utilizes two photodiode sensors, similar to pulse oximeters. The photodiodes are positioned on the finger and on the toe, so that the pulpar arteries are in the scope of the infrared ray. The pOpmètre measures the transit time between the foot of the pulse waves of the finger and of the toe, presuming to approximate the aortic PTT. The algorithm used for the foot detection is the maximum of the second derivative. It measures the finger- toe pulse transit time (ftPTT) on the same pulse wave. PTTs are continuously measured for 20 s, and all pulse waves were accepted for the foot detection and signal processing studies. Two indices are computed: the difference



Figure 1.26: pOpmètre Device.

in pulse wave transit time between toe and finger (ft-PTT; in millisecond) using the maximum of the second derivative algorithm for foot wave detection, and ft-PWV (in meter per second; $\text{ft-PWV} = k \times \text{patient's height} / \text{ft-PTT}$), using a chart based on the height of 187 individuals measured in occupational medicine (personal data), where k is dependent on height. The use of the height chart relates to the fact that the aortic valves correspond to an anatomical stable landmark.

Table 1.3 summaries all the commercial devices for PWV assessment previously described. They mainly differ for the methodology used for the signal extraction (applanation tonometry, piezoelectric mechano-transducer, cuff-based oscillometry or photodiode sensor), for the type of analyzed PWV (depending on the considered acquisition sites it could be the clinical carotid-to-femoral or the commercial finger-to-toe pulse), and, finally for the physical distance these instruments need to be acquired before the procedure started for the velocity evaluation.

Table 1.3: Current commercial devices for PWV measurement with method, assessment type and path length used.

Method	Devices	Measurements	Path length
Applanation Tonometry	SphygmoCor	cf-PWV	Carotid-Notch Femoral-Notch
	PulsePen	cf-PWV	Carotid-Notch Femoral-Notch
Piezoelectric Mechano- transducer	Complior	cf-PWV	Carotid-Femoral
Cuff-based Oscillometry	SphygmoCor Xcel	cf-PWV	Thigh cuff-Notch Notch-Carotid Femoral-Cuff
	Arteriograph	aPWV	Jugulum-Symphysis
	Vicorder	cf-PWV	Notch-Thigh cuff
Photodiode sensor	pOpmètre	ft-PWV	$k \times \text{subject's height}$

*cf-PWV: carotid-femoral pulse wave velocity; ft-PWV: finger-toe pulse wave velocity
aPWV: aortic Pulse Wave Velocity*

Besides the commercial devices, the standard ways to non-invasively extract the value at which the blood flows in the arterial tree consist of using the standard medical imaging, such as:

- *Ultrasound*

Several ultrasonographic techniques based on Doppler velocity assessment have been used to estimate arterial stiffness. Aortic PWV can be measured with Doppler ultrasound, using different approaches [22].

With the ‘simultaneous technique’, two microphones are placed, respectively, to the left side of the neck (to insonate the left subclavian artery) and on the abdomen (to insonate the abdominal aorta above the bifurcation) and record simultaneously the pressure wave.

A more recent technique to measure aPWV is based on the estimation of the delay between Doppler waveforms recorded in the distal aortic arch and in the distal external iliac artery, with ultrasound probe sampling the two sites in sequence. Since wave recording is not simultaneous, an ECG acquisition is needed [37].

CfPWV can be measured with a pulsed Doppler ultrasound probe placed at the carotid artery level, and subsequently, at the femoral artery (ECG recording necessary to synchronize pulse waves) [38]. Path length is measured superficially as the distance between the two probes.

- *Magnetic Resonance Imaging*

MRI is a non-invasive technique that allows direct imaging of the thoracic and abdominal aorta without the use of length approximation. Several MRI techniques have been developed to assess PWV, differing mostly in the way distance and time delay are measured. Phase contrast MRI, for example, can be used to acquire blood flow velocity along any given anatomical plane. Flow measurements obtained either from ‘through-plane’ or inplane velocity-encoded MRI can be used to determine the time delay (transit time) between the onset of flow in cross-section anatomic plane in the ascending and descending thoracic (or abdominal) aorta. In-plane velocity-encoded-MRI proved to be strongly correlated to invasive PWV assessment [39].

On the other hand, as stated in the abovementioned guidelines, the recommended reference standard for true aortic PWV is simultaneous pressure waveforms recorded invasively with high fidelity pressure sensors from just above the aortic valve and just above the aortic bifurcation. If simultaneous recording is not performable, sequential recordings referenced to the ECG is considered an acceptable alternative (ensuring there is no significant variation in heart rate or blood pressure during the recording) [22].

1.4 Studied sensors

In this paragraph all the sensors used for the PWV assesment will be described. As said before, they mainly differ for the transduction method and for the generated signal. What they have in common is the possibility to detect the blood pulse passage, wherever they are placed on the skin in proximity to an artery vessel.

1.4.1 Tonometer

The first approached sensor is a tonometer, specifically designed for this application by STMicroelectronics (Geneva, Switzerland). It consists of a modified pressure sensor (LPS35HW) able to detect superficial tension variations, in other words, configured as a force sensor for this specific application.

The LPS35HW is an ultra-compact piezoresistive pressure sensor which operates as a digital output barometer, whose deflections and relative resistance variations are read through a Wheatstone bridge and which allows to obtain the final pressure value (force, in our case). In the detail, the acquisition chain is composed of a low noise amplifier which, through an ADC, provides a digital value that derives from the variation in resistance (see Figure 1.27) [40].

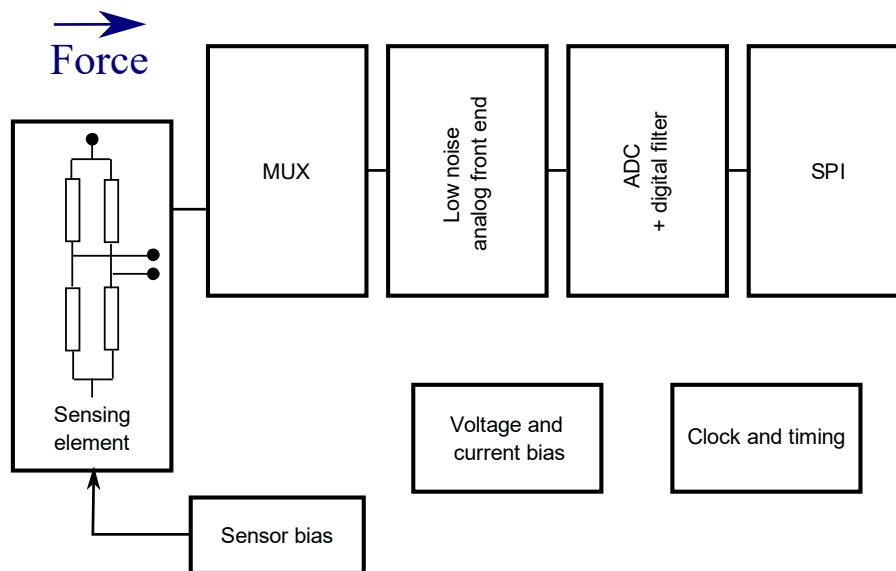


Figure 1.27: Block diagram of the LPS35HW acquisition chain.

In order to obtain a force sensor from the LPS35HW MEMS, its metallic lid was removed and the cavity filled with a resin (blue part in Figure 1.28a)

that transmits the motion to the actual sensor covered with gel (yellow part in Figure 1.28a). This process is under patenting decision. Thus, more details cannot be disclosed. Such modified MEMS was then soldered onto a 1 cm diameter printed circuit board (PCB) alongside two small bypass capacitors (Figure 1.28b). On the bottom side of the PCB is only present a header to power (3.3 V, tenths of μA) the sensor and provide SPI communication (24-bit pressure data output). Only a few millimeters of sensor raise over the plastic cover [40].

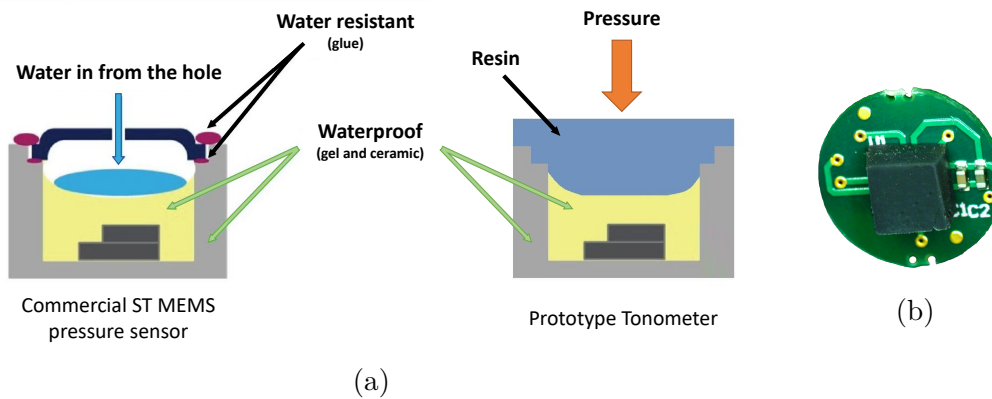


Figure 1.28: (a) The modified tonometer MEMS; (b) A microscope image of the resulting PCB with the black resin [40].

If placed on the skin in proximity of the arterial vessel, this sensor lets to detect the alteration of the superficial tension generated by the blood pulse inside the artery. As reported in the literature and described by the Laplace law (see 1.2.4), this variation is strongly linked to the change of the blood pressure occurring inside the vessel. Through this sensing, it is possible to collect the pulse wave generated by the systolic ejection on different body locations [40].

1.4.2 Optical Sensors

Concerning the photoplethysmogram signal, it has been acquired using two different optical sensors, that will be illustrated in the next paragraphs.

ST Physiological probe

This sensor is a miniaturized optical system based on the ST Silicon Photomultipliers (SiPMs) photodetector coupled with an infrared (IR) LEDs used as optical light sources. The IR LED is necessary as light emitter, meanwhile the SiPM is an advanced light detector able to read weak optical signals coming from deep

arteries (Figure 1.29).

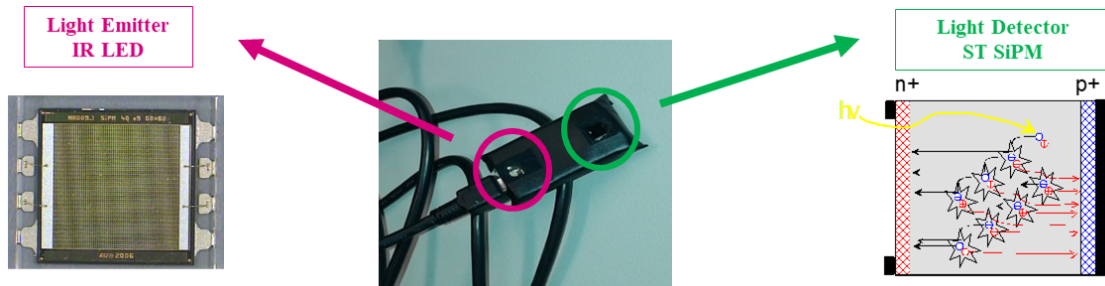


Figure 1.29: The ST physiological probe structure [41].

The SiPM is an optometric sensor made up by a LED and a semiconductor photodiode. Compared to PMT (Photomultiplier tube) or APD (Avalanche PhotoDiode) it has several advantages. Such as: low bias voltage ($<100\text{ V}$), high photon detection efficiency (PDE) for visible photons or in the near infrared, excellent single photon response, fast rise time ($\ll 1\text{ ns}$), low energy consumption, insensitivity to magnetic fields, compactness, and mechanical strength.

SiPM is produced directly from a silicon wafer whereby multiple arrays of microcells are implanted, which everyone is a single photon avalanche photodiode. Every microcell has a square shape with an active area of $40 \times 40\ \mu\text{m}^2$ size. In addition, thin grooves filled with oxide and metal surround the active area of the pixels in order to reduce crosstalk between adjacent microcells.

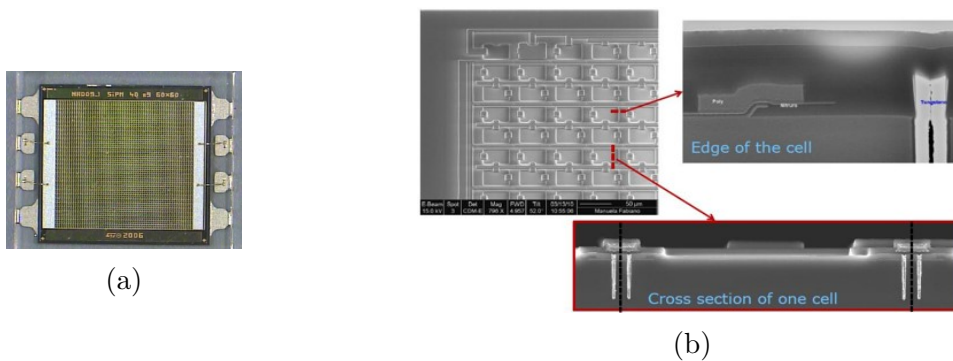


Figure 1.30: (a) Array of photodiodes, 4400 cells ($60\ \mu\text{m} \times 60\ \mu\text{m}$.; (b) Technological Details.

Each SPAD (Single-photon avalanche diode) works in Geiger mode and it is connected to the power supply via a damping resistor to switch off the avalanche

current. The resistance value increases as the temperature decreases with a temperature coefficient equal to $-0.98 \text{ k}\Omega/\text{°C}$.

A longpass absorbing optical filter with cutoff at 650 nm is mounted on SiPM surface. This probe is ideal to read weak optical signals coming from deep arteries.

Osram SFH7050

The SFH7050 is a fully integrated optometric sensor, designed and optimized for reflective pulse oximetry in PPG system (Figure 1.31). It has three LEDs emitting at different wavelength and a large area photodiode (PD). The three LEDs are green (525 nm), red (660 nm) and infrared (940 nm).

Furthermore, LEDs and PD are physically separated by a light barrier to minimize the internal crosstalk, enhancing the signal-to-noise ratio (SNR). The physical dimensions of the package are $4.7 \text{ mm} \times 2.5 \text{ mm} \times 0.9 \text{ mm}$.



Figure 1.31: SFH 7050 with integrated LEDs and photodiode.

The signal obtained by this optical sensor is strongly influenced by the physical implementation (cover glass, air-gap) and by the biological characteristics (such as the measuring point, the skin tone, and the applied pressure). The photodiode has a sensitive area of $1.3 \times 1.3 \text{ mm}^2$ and transforms the light received from the environment into current, which is generally amplified and converted to voltage through a trans-impedance amplifier.

For instance, if the photodiode is powered with $V_R=5 \text{ V}$ at $T_A=25 \text{ °C}$ these are some typical values of the component:

- Photocurrent ($I_{p,940}$): $1.3 \text{ }\mu\text{A}$ ($\lambda=940 \text{ nm}$, $E_e=0.1 \text{ mW}/\text{cm}^2$);

- Maximum sensitivity wavelength: (λ_{Smax}): 920 nm;
- Spectral range of sensibility ($\lambda_{10\%}$): 400 nm to 1100 nm;
- Spectral sensitivity (λ_{940}): 0.77 A/W;
- Forward voltage (V_F): 0.9 V ($I_F=10$ mA, $E_e=0$ mW/cm²)

1.4.3 Analog Microphone MP33AB01H

The MP33AB01H (STMicroelectronics, Geneva, Switzerland) is a compact, low-power microphone built with a low-profile sensing element, capable of detecting acoustic waves. This last part is manufactured using a specialized silicon micro-machining process to produce audio sensors.

In the detail, the MP33AB01H has an acoustic overload point of 125 dB SPL with a 66 dB signal-to-noise ratio and it is guaranteed to be operative over an extended temperature range from -30 to 100 °C.

The main electrical characteristics of this component, specified for a $V_{dd}=2.2$ V, are:

- Current consumption(I_{dd}): 0.25 mA;
- Sensitivity at 1 kHz (S_O): -38 dB V;
- Signal-to-noise ratio at 1 kHz (SNR): 66 dB;

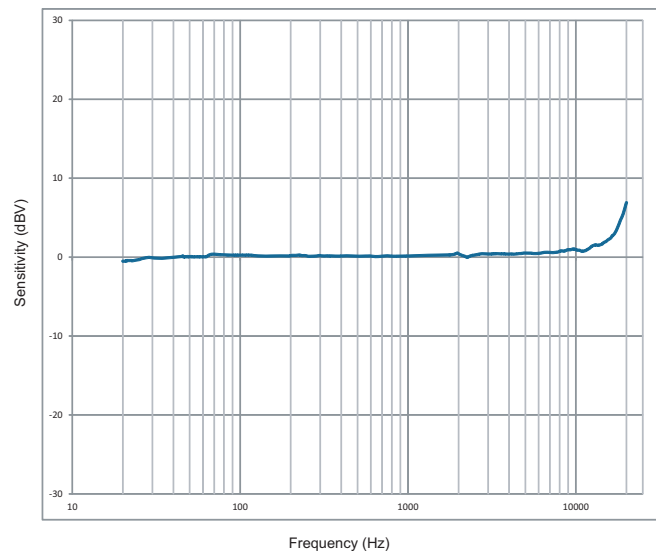


Figure 1.32: MP33AB01H analog microphone typical frequency response [42].

- Distortion at 125 dB SPL (THD): 10%.

The typical frequency response, normalized at 2 kHz and given by datasheet is reported in Figure 1.32.

This sensor, based on MEMS capacitive transduction, consists of two silicon plates, one of which is fixed and the other movable. The device architecture includes an electrode that covers the fixed surface to make it conductive, and some acoustic holes that allows sound to pass through, as shown in Figure 1.33. The movable plate is only fixed at one side of its structure, hence it can move. Thus, the membrane moves back due to the ventilation hole that makes it possible for the flowing out of the compressed air in the back chamber. This cubicle permits the membrane to move inwards.

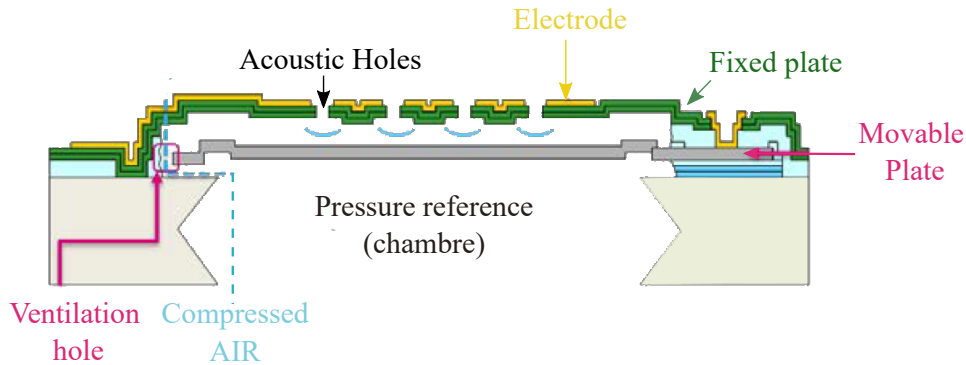


Figure 1.33: MEMS microphone mechanical configuration [42].

Therefore, the microphone MEMS sensor is a variable capacitor and its transduction principle is based on a change in the capacitance between a fixed plate and a membrane, where the movement of the latter is due to the incoming wave of the sound. The integrated circuit converts the variation of the polarized MEMS capacitance into an analogue output.

1.4.4 Graphene pressure sensor

The last sensor implemented is an innovative graphene pressure device, developed by the nanochemistry group of "Institut de science et d'ingénierie sur-moléculaire" (ISIS) in Strasbourg (France). Thanks to a straight collaboration between us and the french group, this sensor has been improved and upgraded to be integrated in a wearable system for the continuous PWV monitoring, as it will be explained later in the detail (see Chapter 5).

This sensor consists of a layer-by-layer structured based on graphene. This material was chosen for its peculiar characteristics, such as excellent electrical conductivity, high transmittance, outstanding mechanical properties, and large surface area [43]. Moreover, it is noteworthy that graphene can be safely employed in devices being in direct contact with human skin, making it suitable for biomedical application.

The approach used in this device fabrication lets to extremely improve the sensitivity of a common piezoresistive pressure sensor. To do this, the active material has been assembled by merging the commercial available graphene oxide (GO) with amino functionalized molecules. Reacting these two, in fact, permits to form covalent bonds on the basal plane of GO through the epoxy ring-opening reaction (Figure 1.34).

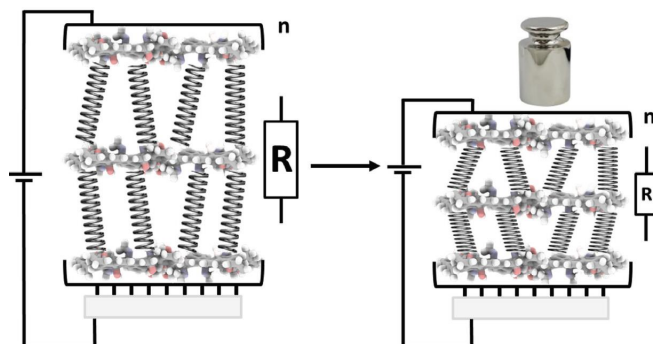


Figure 1.34: Schematic of working principle of the pressure sensor [44].

Three diverse organic molecules, with similar contour length but different rigidity, were chosen to functionalize the GO and see which one would give better performances in terms of response to pressure changes (Figure 1.35): triethylene glycol amine (R_1), 1-octylamine (R_2), and 4-aminobiphenyl (R_3). With them, three distinct sensors were created. At the end of the evaluation, the R_1 (triethylene glycol amine) is the molecule that seems to have a more linear correlation.

As recalled in Figure 1.35, in the first place a condensation between R_1 and GO is created, at the end of this hybrid structures are obtained in the form of ink dispersed in ethanol. Then, in a second step, such chemically modified GO (CMGO) is reduced with hydrazine to restore high electrical conductivity. This two steps constitute the preliminary phase of molecules preparation, that will lead to multilayer structures with spacing between adjacent GO sheets which are dictated by the employed molecular pillars.

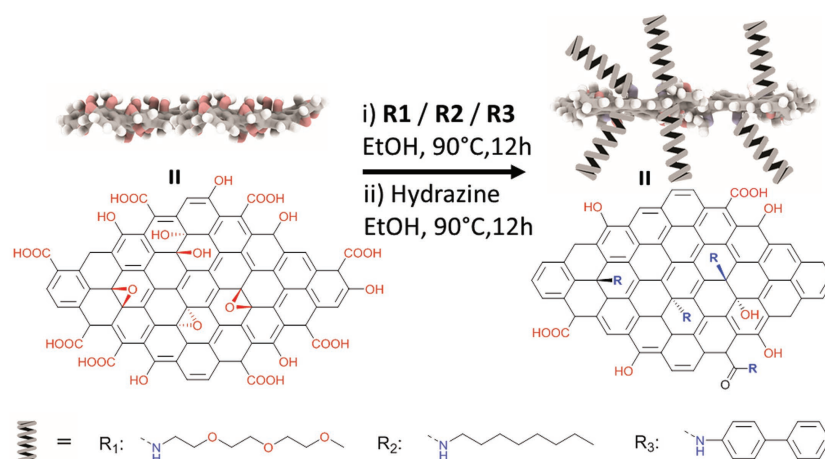


Figure 1.35: Synthesis and architecture of rGO-R₁, rGO-R₂, and rGO-R₃ [44].

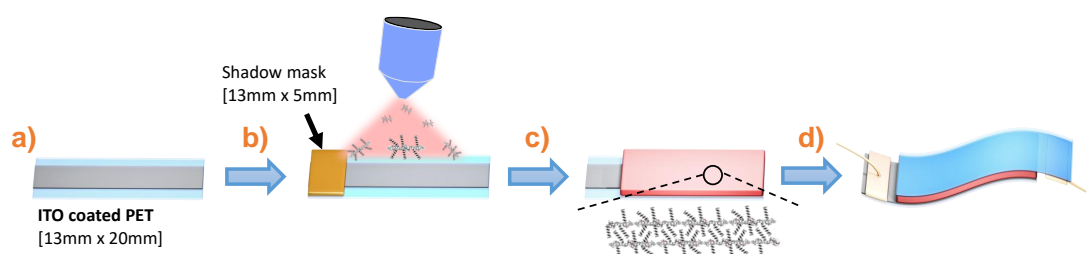


Figure 1.36: Graphene pressure sensor fabrication process [44].

When the molecular compound is ready, the real device production stages begin. In particular, as depicted in Figure 1.36, the main steps are:

- Two rectangular (13x20 mm²) substrates of indium tin oxide (ITO) – poly(ethylene terephthalate) (PET) are prepared;
- Spray-coating* of functionalized reduced graphene oxide inks (rGO-R₁) through a shadow mask onto the two PETs;
- The amount of accumulated material is monitored by UV–vis absorption, when a transmittance of 20% at 500 nm is achieved the mask is removed;
- The two electrodes are fixed together using polyimide (PI) tape; copper wire and silver paste are used for electrical contact.

The final result is a high sensitive piezoresistive sensor capable of small pressure variations detection. The three different configurations (rGO-R₁, rGO-R₂, and rGO-R₃) were tested by exploiting a force gauge equipped with a movement-control stand combined with a sourcemeter to offer a steady bias voltage. In Figure 1.37

are reported the results obtained, plotting the equation 1.8 that links the applied pressure (P) with the resistance with the applied pressure (R) or without (R_0).

$$S = \frac{\Delta R}{R_0} \frac{1}{\Delta P} \quad (1.8)$$

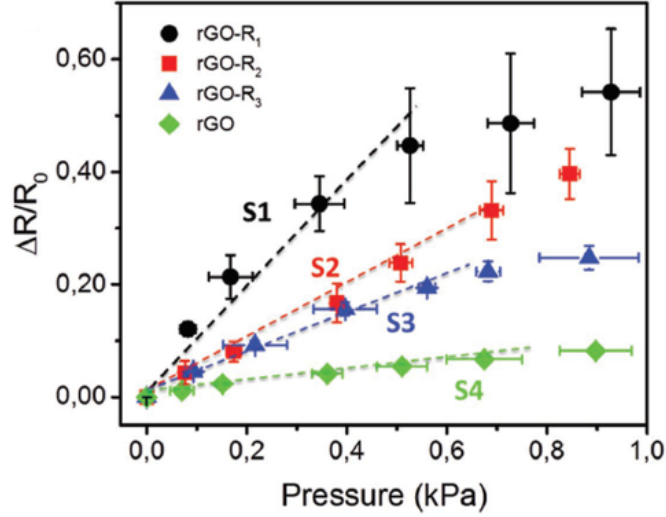


Figure 1.37: Relative resistance as a function of the pressure applied for sensor rGO-R₁ (black circles), rGO-R₂ (red squares), rGO-R₃ (blue triangle), and simple rGO (green diamond) (error bar: mean \pm standard deviation). [44].

Considering the linearity and the amount of inducted response (i.e. the resistance percentage change), for this project the functionalized rGO-R₁ has been the one chosen.

1.5 Implemented Device

This paragraph contains all the off-shelf devices adopted for the projects conducted during this PhD project, with their main characteristics.

1.5.1 STM32F429 Discovery Kit

The STM32F429 Discovery Kit board (Figure 1.38) hosts the microcontroller unit STM32F429ZIT6, a 32-bit high-performance microcontroller part of the STM32F4 family based on the ARM Cortex-M4 core. The Discovery Kit also includes an ST-LINK/V2 embedded debug circuit, a 2.4" QVGA TFT LCD,

an external 64-Mbit SDRAM, an USB OTG micro-AB connector, LEDs and push-buttons (user and reset). The power supply can be provided by the host PC through the USB cable, or by an external 5 V power supply.

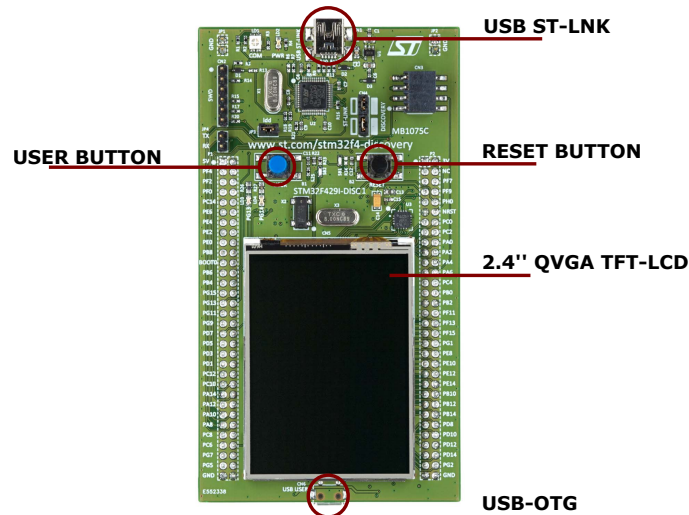


Figure 1.38: Discovery Kit STM32F429 board and its main characteristics.

The main component of the Discovery Kit is the STM32F429ZIT6 microcontroller unit based on ARM Cortex-M4 32-bit RISC core operating at a frequency of up to 180 MHz, which features a single precision Floating Point Unit (FPU). This microcontroller incorporates high-speed embedded memories (2 Mbyte of Flash memory and 256 Kbytes of RAM) and an extensive range of enhanced I/Os and peripherals connected to two APB (Advanced Peripheral Bus) buses, two AHB (Advanced High-performance Bus) buses and a 32-bit multi-AHB bus matrix.

On the board, there are 114 General-Purpose input/outputs (GPIOs) pins which can be configured by software as output, as input or as peripheral alternate function. Moreover, this MCU offers three 12-bit ADCs which shares up to 16 external channels, performing conversions in the single-shot or scan mode (automatic conversion on a selected group of analog inputs) and the conversion could be triggered by the embedded general-purpose timers. Furthermore, the STM32F429ZIT6 features 6 SPIs (Serial Peripheral Interface Bus) interfaces configurable in slave or master modes, in full-duplex or simplex communication modes.

1.5.2 STEVAL-IDB006V1M

The STEVAL-IDB006V1M is an evaluation board based on the SPBTLE-RF module (Figure 1.39). The module is ETSI, FCC and IC certified and uses

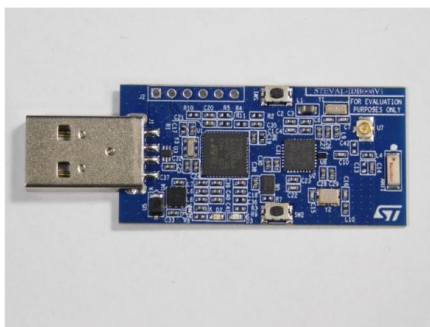


Figure 1.39: Steval-IDB006V1M, dongle based on the SPBTLE-RF.

the BlueNRG-MS, a low power Bluetooth Smart IC which is compliant with the Bluetooth 4.1 specification and supports both master and slave roles. The SPBTLE-RF module integrates ST's BALF-NRG-01D3 balun and a chip antenna. The STEVAL-IDB006V1M is equipped with an STM32L low power microcontroller to control the BlueNRG, and also features a USB connector for PC GUI interaction and firmware update, such as the one available for the BlueNRG-MS evaluation kit. An SWD connector allows the development of specific firmware on the microcontroller.

1.5.3 STEVAL-IME002-V1

The STEVAL-IME002V1 evaluation board has been designed around the new HM301D Diagnostic Quality Analog Front End, with the purpose to demonstrate how to perform measurements with bio-electric and bio-impedance sensors. It contains a 32-bit microcontroller that is part of the STM32 family and its primary role is to supervise the SPI protocol of the analog front ends and to implement an USB connection with the PC (Figure 1.40).

This board has been designed to manage up to three HM301D devices in an SPI concatenation where the three sensors on the board switch thanks to a dedicated mux. The working daisy chain sequences are U1 (first HM301D on the board), U1 and U2 (second HM301D), U1 and U2 and U3 (third HM301D). Only one configuration is possible and the access order can't be modified.

By using this board it is possible to record the Einthoven equilateral triangle and all the lead connections (see Paragraph 1.2.1). In this project, only two derivations have been used, as they are sufficient to acquire the requested features from the ECG signal.

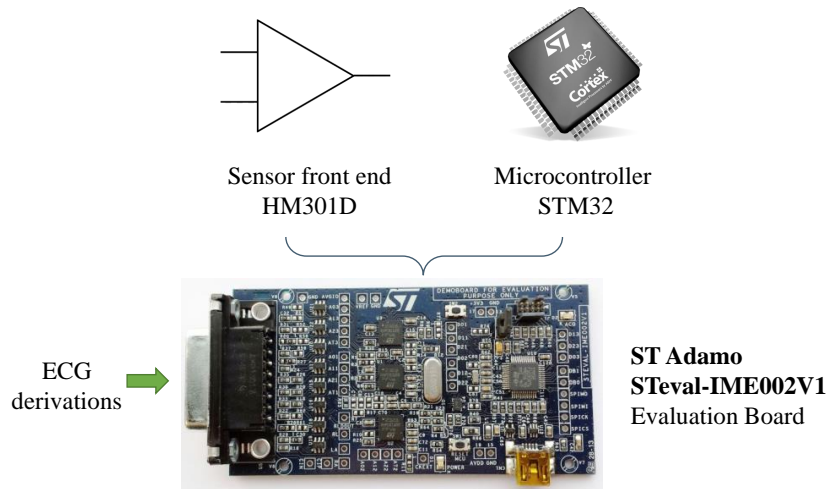


Figure 1.40: STeval-IME002-V1, dongle based on the SPBTLE-RF, Board connection and its logic diagram..

1.6 Used Softwares

The last paragraph of this chapter describes the main software used, in broad terms.

1.6.1 Keil

Keil- μ Vision5, an integrated development environment made by ARM, was used to program, configure and manage the MCUs and its modules. It is a windows-based development platform that integrates the tools needed to develop embedded applications including a C/C++ compiler, macro assembler, linker/locator and HEX file generator. It provides all the required tools to support the specific characteristics and features of STM microcontroller families, including the device debugging capabilities and the flash memory firmware download.

1.6.2 VisualStudio

Visual Studio is an Integrated Development Environment(IDE) developed by Microsoft to develop GUI(Graphical User Interface), console, Web applications, web apps, mobile apps, cloud, and web services, etc. With the help of this IDE, it is possible to create managed code as well as native code. It uses the various platforms of Microsoft software development software like Windows store, Microsoft Silverlight, and Windows API, etc. It is not a language-specific IDE as there is also

the opportunity to write code in C#, C++, VB(Visual Basic), Python, JavaScript, and many more languages. It provides support for 36 different programming languages.

1.6.3 Matlab

MATLAB is a high-performance language for technical computing. It integrates computation, visualization, and programming in an easy-to-use environment where problems and solutions are expressed in familiar mathematical notation. This environment is an interactive system whose basic data element is an array that does not require dimensioning. This allows to solve many technical computing problems, especially those with matrix and vector formulations, in a fraction of the time it would take to write a program in a scalar non-interactive language such as C or Fortran.

Chapter 2

The ATHOS device

This second chapter contains the detailed description of the main prototype born from this PhD project. It consists of a clinical device able to assess pulse wave velocity (PWV) in a easy, non-invasive, and reliable way; through both the one and two steps methods (previously discussed in Paragraph 1.3.1). This system, indeed, could be interfaced with a commercial electrocardiograph to perform the traditional two-steps PWV evaluation. But, it also presents two separate sensors for the simultaneous carotid and femoral acquisition.

Thanks to the strict collaboration with the internal medicine team of "Città della salute e della scienza" hospital in Turin, this instrument has been developed as the right answer to a specific request to have a reliable, easy-to-use, and low-cost device. The continuous medical feedback let to address all the practical and usage aspects and to obtain an innovative approach, part of which (the software) is now under patent submission.

This chapter is structured as follow: in the first part the hardware of the device is detailed, the second presents the software with the signal processing and, in the last, the validation results are shown.

2.1 System overview

The ATHOS (Arterial sTiffness faitHful tOol aSsessment) prototype for noninvasive PWV evaluation is mainly composed of a hardware unit that manages the signals acquisition and a specific laptop application that processes the acquired data and provides a graphical representation to the clinical operator. The entire system has been developed in order to be compliant with the clinical safety rules and guidelines described in the IEC-60601 standard for medical devices [45]. Furthermore, although the system performs the PWV one-step measurement, it offers the possibility to be interfaced with an external clinical-grade ECG device. This choice allows doctors to monitor the patient's health condition and, in addition, to have the opportunity to compare the resulted PWVs both with the direct differential PTT and with the two-steps method (provided by the gold standard instrument, still based on ECG).

The ATHOS device comprises a main unit that manages and synchronizes all the signal acquisitions. With this system, there is the possibility to simultaneously acquire two pulse waves together with the ECG signal coming from the EDAN SE-1 electrocardiograph (Edan, Shenzhen, China), see Figure 2.1.

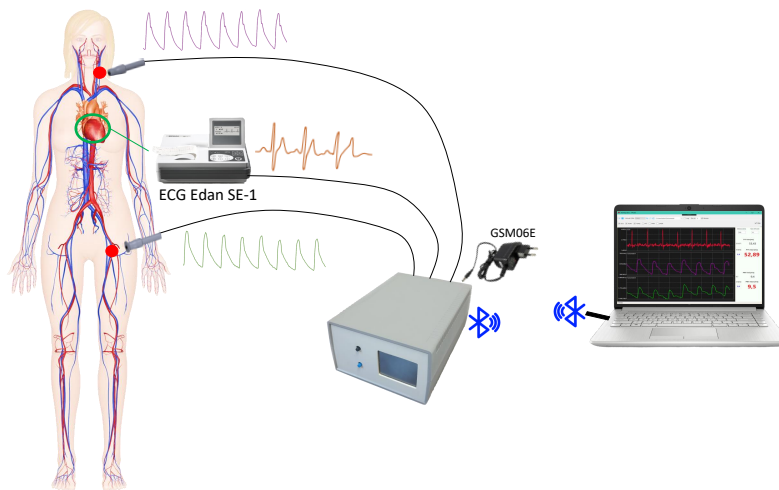


Figure 2.1: ATHOS device summary scheme [40].

The diagram reported in Figure 2.2 (with in yellow the data flow path) outlines the connections that allow the signal to be acquired by the probes, collected by the main unit and wire-less sent to the laptop, where the software plot and process the data. A powerful MCU, included in the central unit, handles the synchronous acquisition of the three different signals (two digital tonometers and one analog

ECG from the Edan SE-1) and the low energy Bluetooth transmission (v4.1) of the collected data.

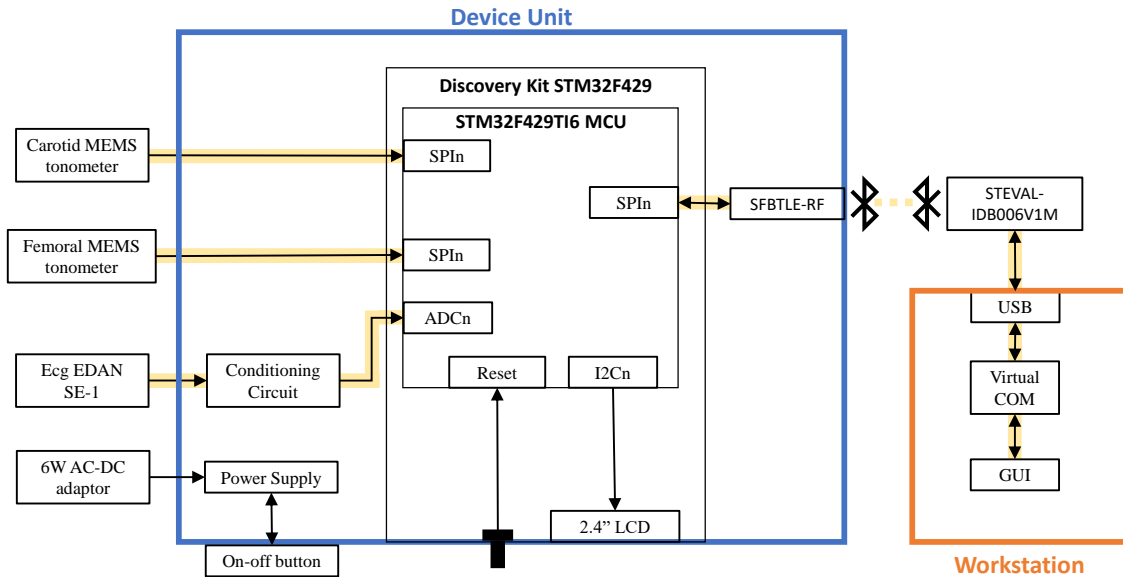


Figure 2.2: Block diagram of ATHOS system.

2.2 The system hardware

To fulfill the compliance with the IEC-60601-1 standard, the acquisition unit is powered by a 6W AC-DC adaptor (GSM06E Mean Well). This power supply is specially designed for medical equipment because it implements double isolation with respect to the AC power supply. In addition, all the connectors for cables and panels were chosen to ensure a safe connection, avoid misconnections, and be suitable for medical applications.

The entire acquisition system is managed by an STM32F429 Discovery Kit (Paragraph 1.5.1) and placed into the main unit (Figure 2.4b).

The adopted Discovery Kit also includes a 2.4” LCD that is used to give the operator useful information about the sensors and the status of Bluetooth Low Energy (BLE) wireless connection. To power the discovery board, starting from the 6V voltage given by the external power supply, a linear voltage regulator provides the required 5V. When the discovery board is switched on, it generates a 3.3V voltage useful to power the MEMS sensors for the pulse wave signals

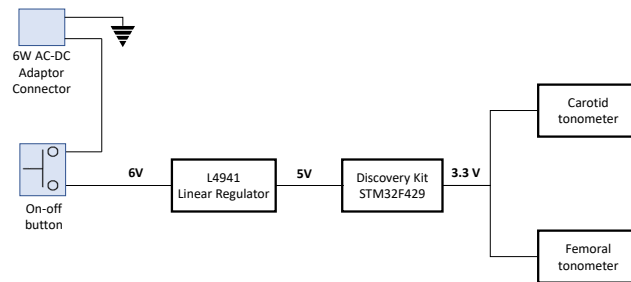


Figure 2.3: ATHOS power supply scheme.

detection. In Figure 2.3 is reported the scheme of the power supply and how the 3.3 V voltage supply for the tonometers is created from the 6 W AC-DC Adaptor.

The STM32F429 Discovery kit also offers two microswitches that could be programmed to give a direct command to the MCU. Both the buttons are made accessible on the device front panel and they could be pressed by the operator to reset the system (Figure 2.4a). Moreover, there is a switch to turn on or off the entire device in the back panel.



(a)



(b)

Figure 2.4: ATHOS main device unit: (a) The unit front panel; (b) The internal interconnections [40].

2.2.1 Tonometers interconnection

The sensors used for the arterial pulse acquisition are the tonometer probes, described in 1.4.1, that provide a digital output. They are interfaced to the MCU core using two SPI ports, configured in a 3-wire communication protocol.

Compared to a normal SPI interface, that uses four signal, this protocol lets to reduce the communication via to three: clock (SCLK), slave select (CS), and a single data line (MOSI) used in half-duplex mode.

This mode is enabled by setting the BIDIMODE bit in the SPICR1 register. In this mode SCK is used for the clock and MOSI in master or MISO in slave mode is used for data communication. The transfer direction (Input/Output) is selected by the BIDIOE bit in the SPI_CR1 register. When this bit is 1, the data line is output otherwise it is input. In Table 2.1 are summarized the actions needed for transmit and receive with this protocol.

Table 2.1: Transmit and receive in bidirectional mode with STM32F429ZIT6

Transmitting (BIDIMODE=1 & BIDIOE=1)
Data are written into the SPI_DR register (<i>Tx buffer</i>)
Data are parallel loaded from the Tx buffer into the 8-bit shift register during the first bit transmission and then shifted out serially to the MOSI pin
No data are received
Receiving (BIDIMODE=1 & BIDIOE=0)
The sequence begins as soon as SPE=1 and BIDIOE=0
The received data on the MOSI pin are shifted in serially to the 8-bit shift register then parallel loaded into the SPI_DR register (<i>Rx buffer</i>)
The transmitter is not activated and no data are shifted out

The two MEMS sensors (Paragraph 1.4.1) were placed into two 3D-printed supports to facilitate the sensor usage, made with a specific resin for clinical use (Figure 2.5). To obtain some probes that easily give stable and reliable signals, several supports of different types and forms were tested with the help of the medical staff. The dimensions, shape, and terminal part profiles were modified to get the carotid and femoral best pulse waves, respectively. The pen-shaped supports that simplified operator handling and provided the most desirable results were selected. The carotid probe terminal part is sharper to be kept as a pen, whereas the femoral one is flatter to be placed among the operator's left-hand

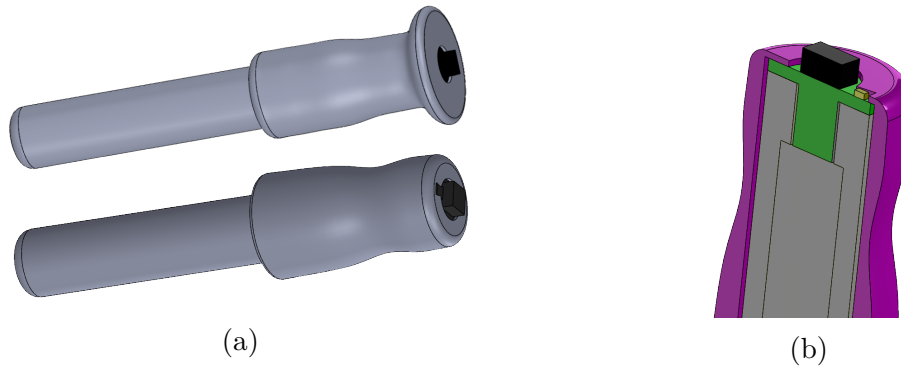


Figure 2.5: (a) 3D printed pen supports for the MEMS sensor; (b) Probe Tip section [40].

fingers. In this way, unlike SphygmoCor (see Paragraph 1.3.1) with the same pen-shaped sensing element for both sites, a stable simultaneous sensor placement is possible, leading to better signal capture [40].

2.2.2 ECG EDAN SE-1

Concerning the ECG, the SE-1 Edan (Edan, Shenzhen, China) electrocardiograph device was chosen to be part of the system because it can output the acquired ECG signal through an external input/output connector.

The SE-1 single-channel electrocardiograph is a high-performance digital

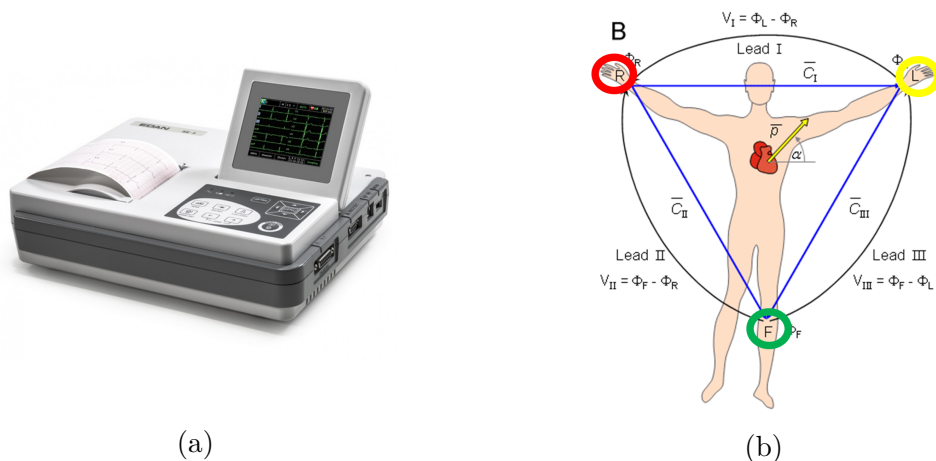


Figure 2.6: (a) ECG Edan SE-1; (b) The usual configuration used with ATHOS.

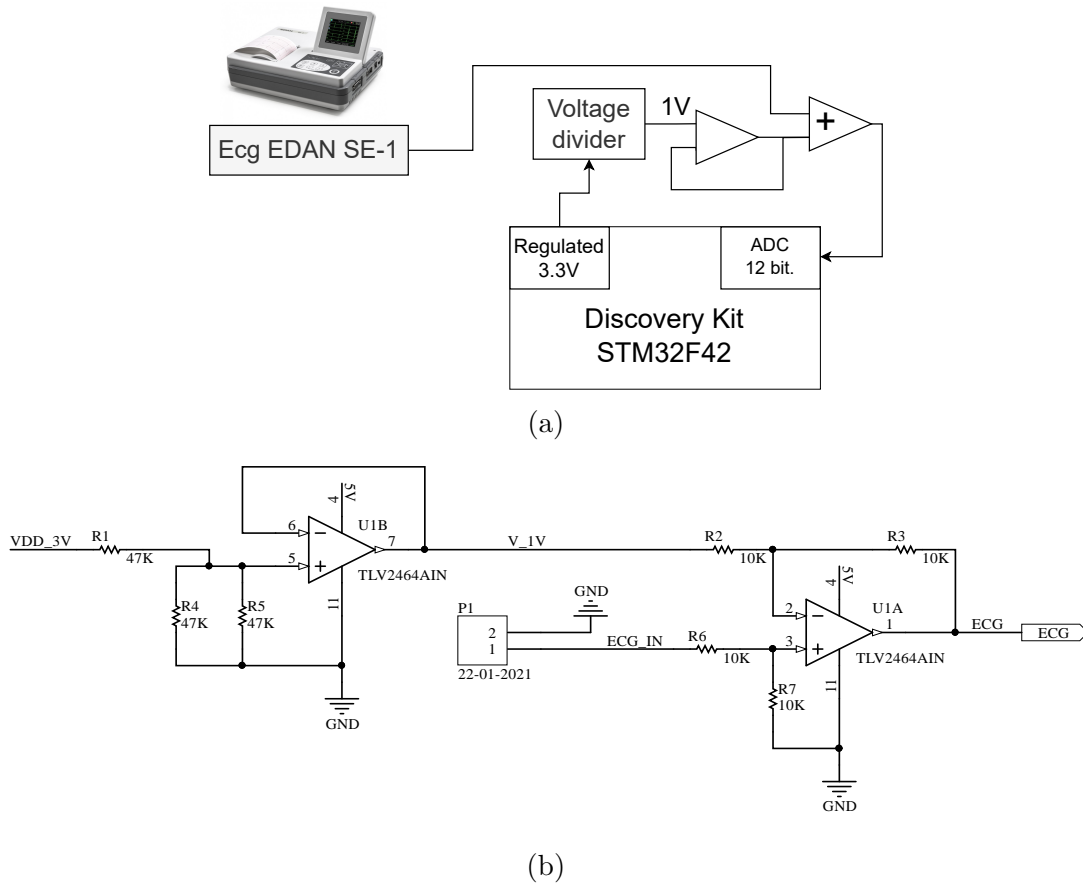


Figure 2.7: (a) Diagram and (b) Schematics of the analog electrocardiogram conditioning from the EDAN SE-1 to the Discovery Kit STM32F42.

single-channel ECG recorder (Figure 2.6a). It could work with two different recording modes: the manual and the automatic, they differ for the way the derivation is chosen (in the first by the operator, in the second by the device).

The design of the single-channel electrocardiograph complies with the international standard IEC 60601-1 of electrical equipment for medical use: general requirements for safety and special requirements of IEC 60601-2-25 for the safety of electrocardiographs, etc. The classification of this device is Class I, type CF, which means a high degree of protection against electric shock and a fully isolated and defibrillation protected patient connection.

Usually in the ATHOS, according to the Einthoven's triangle (see Paragraph 1.2.1), only three of the twelve given electrodes are placed on the subject: the L, F, R and the Lead I is manually chosen (Figure 2.6b).

The such acquired signal is taken from the SE-1 analog output and given as input into the ATHOS main unit, where a simple interface circuitry adjusts it to be compliant with the MCU's characteristics embedded Analog to Digital Converter (ADC) and take advantage of its input dynamic range.

This circuits adds 1 V bias to the cents of mV amplitude of the signal, as reported in Figure 2.7a. The conditioning circuit added to the system is required to sum a buffered bias to the signal to fit the requested 12 bit ADC input range (0V to 3.3V).

2.2.3 The firmware and Bluetooth transmission

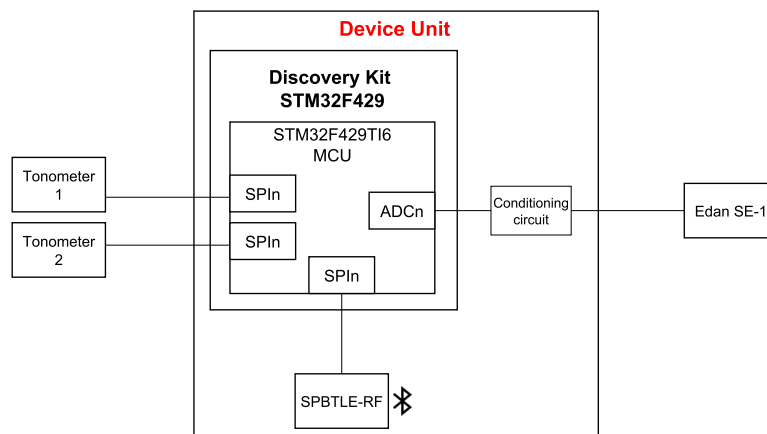


Figure 2.8: The STM32F429ZIT6 microcontroller interconnections in ATHOS.

Figure 2.8 schematizes the ATHOS MCU interconnections: the acquisition of both the tonometers through two SPI, the ADC conversion of the ECG signal, and the data trasmission by the bluetooth module.

To better synchronize both the digital output of MEMS pressure sensors and the analog ECG signal, the MCU sampling frequency is set at 680 Hz, ensuring a temporal resolution of 1.5 ms. But, considering that due to its fabrication components the tonometer maximum sampling frequency is 170 Hz, the three readings have to be synchronized. The flow chart in Figure 2.9 displays the steps followed by the microprocessor for the three signal simultaneous acquisition and how the MCU performs a tonometer reading every four ADC conversions ($170 \times 4 = 680$).

Captured data are put on a buffer that contains 7 samples from each tonometer

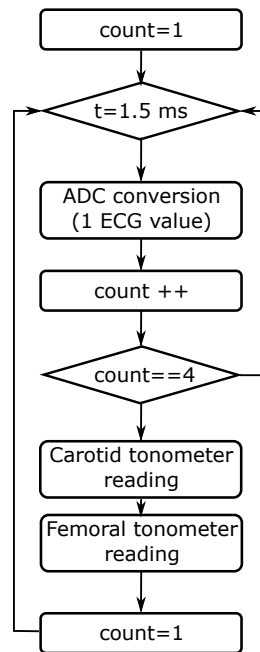


Figure 2.9: The ATHOS STM32F429ZIT6 microcontroller firmware flowchart.

and 28 (7x4) ECG values, forming a buffer of 70 Byte (Figure 2.10), which is then sent through the wireless link.

To ensure the galvanic isolation of the subject, the acquisition unit is controlled by the operator’s laptop through a wireless interconnection. On the PC, the developed software interface helps the operator find the correct placement of the sensors, monitor the quality level of the collected signals, and save them for further analysis. The selected wireless module is the SPBTLE-RF (STMicroelectronics, Shanghai, China) that integrates BLE radio operating at 2.4 GHz (Bluetooth specification version 4.1). It provides a low power data transmission up to 10m, guaranteeing a safe distance between the laptop and the main unit (full compliancy with the IEC-60601). This module is interfaced with an SPI port of the STM32F429 MCU. It establishes a connection with a STEVAL-IDB006V1M module (STMicroelectronics, Shanghai, China), plugged into the operator PC

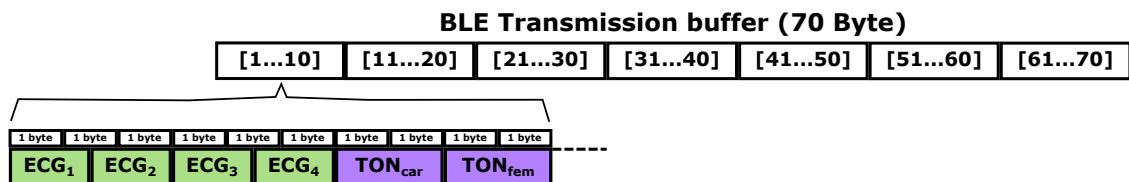


Figure 2.10: The ATHOS Bluetooth protocol.

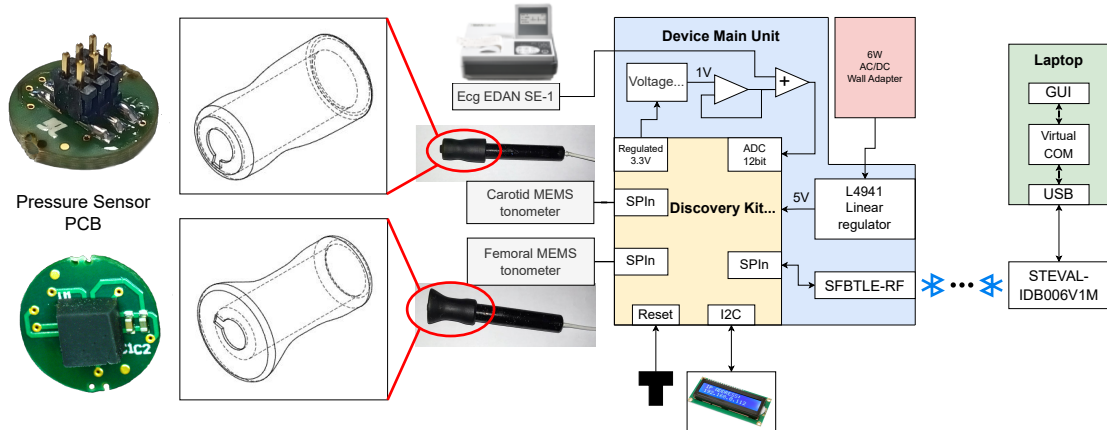


Figure 2.11: Block diagram of ATHOS system [40].

through a USB port [40].

For the real-time data transmission, an ad-hoc protocol was developed and implemented in order to take advantage of the full Bluetooth bandwidth. In which, as soon as one BLE transmission buffer (Figure 2.10) is ready, and this appends each 28 ms (4 ADC reading repeated for 7 times to fill the entire buffer), it is sent to the dongle where it is unpacked for the data showing and process.

Finally, Figure 2.11 summarizes all the hardware component involved in the device, their interconnections and some detailed of the innovative sensors, and relative probes, implemented in ATHOS.

2.3 The system software

By means of the Bluetooth Low Energy (BLE) wireless module and the firmware specifically created, data arrive from the acquisition system to the USB-port-dongle. A virtual serial communication port (COM) is then created on the laptop and, thanks to this, the Graphical User Interface (GUI) is able to receive and manage the data sent from the main acquisition unit (see Figure 2.11).

Moreover, with the GUI the operator can send commands to the acquisition system. For instance, from the user interface it is possible to start and stop the acquisitions, to reset the device and, if needed, to force the MCU to generate a dummy sawtooth waveform, especially useful for debugging purposes.

When a new transmitted buffer is available, this is unpacked and the three

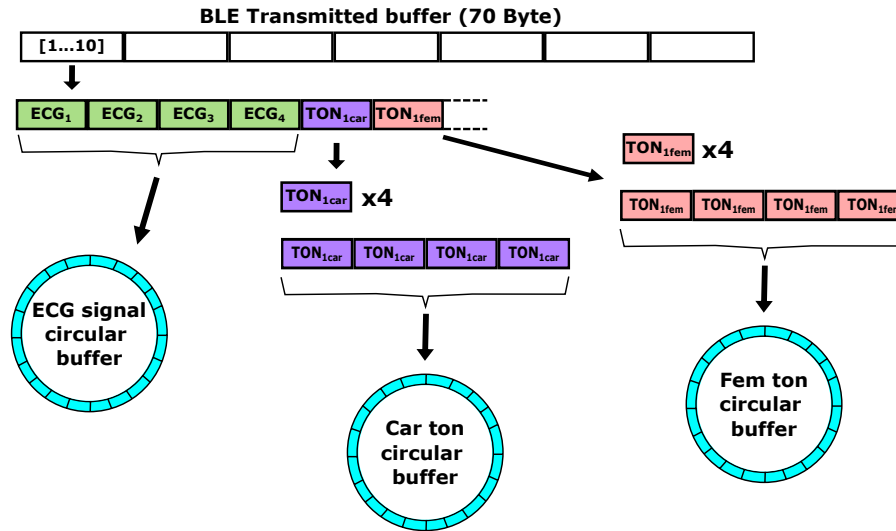


Figure 2.12: Transferred buffer processing: distribution in the three circular buffers (carotid pulse wave (*Car ton*), femoral pulse wave (*Fem ton*) and ECG signal) used for the signals plot in the GUI window.

signals (femoral pulse wave, carotid pulse wave and ECG) are placed into three dedicated circular buffers. To synchronize the visualization of the signals the different sampling frequencies must be considered. For this reason, tonometer waveforms that have a lower number of samples due the lower reading timing, are resampled at 680 Hz to be coherent with the ECG sampling frequency. To do this resampling as fast as possible and to ensure a right timing for the signal visualization, each tonometer sample is repeated four time. In this way, the length of all the signals matches and the GUI can properly run. These three buffers (the ECG, carotid and femoral tonometer) are used to update the signals visualization in the GUI window, at the same time, by means of a parallel task, the carotid and femoral pulse waves are stored for real-time PWV evaluation (Figure 2.12).

For the purpose of updating the PWV every cardiac cycle, the ATHOS interface updates the PWV value every 1.5s. This choice was done in order to have an interval time that comprises at least one blood pulse, considering also subjects with a bradycardia rhythm (a cardiac frequency of 40 bpm corresponds to a blood pulse every 1.5s). Furthermore, a 1.5s PWV update interval lets to achieve a good compromise in terms of parameter evolution and user readability. It is also important to remark that PTT and PWV values displayed are averaged on the last ten cardiac cycles; in this way, the operator can monitor the stability of the parameters and spurious or anomalous events are filtered out.

2.3.1 The intersecting tangent point

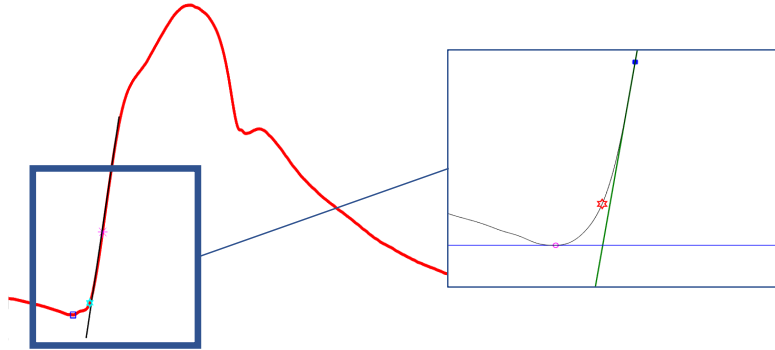


Figure 2.13: Extraction of Intersecting Tangent Point (ITP).

The goal of the algorithm implemented in the ATHOS GUI is to extrapolate on each cardiac cycle the feature that lets to detect the blood pulse passage. For this purpose, the intersecting tangent method is addressed. It is essentially the signal “foot” extrapolation, that corresponds to the point delineated by the projection on the signal of the intersection between a horizontal line, passing through the minimum before the start of the systolic peak, and the tangent to the point of maximum first derivate (Figure 2.13). As demonstrated by Chiu et al. [46], this characteristic of the pulse resulted to be the most reliable among all the features that could be extracted in the arterial pulse (such as minimum, maximum, first derivate point, etc.).

2.3.2 The filters

The algorithm implementation for the intersecting tangent point detection includes several filters steps for removing the DC-bias, for evaluating the heart-beat frequency and, by consequence, the cardiac period of the subject under investigation. Several filter types were evaluated, but the ones that resulted to be more effective are the biquadratic filters, which correspond to a second order recursive linear filter (containing two poles and two zeroes). This choice was done because, unlike all the other digital filter architectures, their structure lets to obtain less signal distortion with a more efficient computational implementation. Furthermore, considering the frequencies involved in our system, they introduce a low phase delay and avoid numerical non-convergence issues.

Specifically, each filter-step is implemented by a zero-phase forward and reverse four stages biquadratic filter: the signal is reversed, it is filtered with a biquadratic filter for the first time and then, after a second reversion, it is again filtered.

Each reversion means to rearrange the order of the samples contained in the signal by putting the elements in the backwards order. The double filtering approach avoids phase shift and ensures the temporal alignment between the pre- and the post- filtered signals. Specifically, the applied Biquadratic Cascade IIR Filters uses a direct form II transposed structure [47] (Figure 2.14), in which every biquadratic stage implements a second-order filter using the difference equation 2.1.

$$y[n] = b0 * x[n] + d1 \tag{2.1}$$

Where:

$$d1 = b1 * x[n] - a1 * y[n] + d2 \tag{2.2}$$

$$d2 = b2 * x[n] - a2 * y[n] \tag{2.3}$$

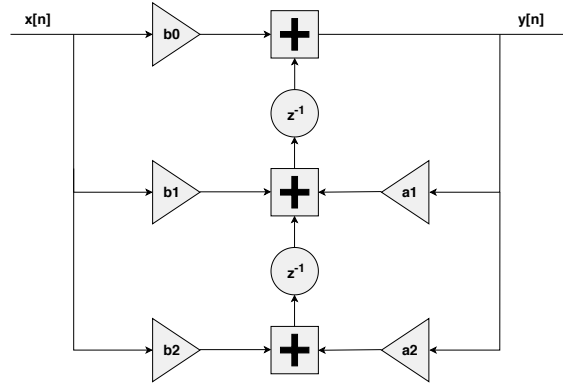


Figure 2.14: Biquadratic Cascade IIR Filters block diagram.

2.3.3 The algorithm for real-time PWV

Here below, the steps addressed to extrapolate the cfPTT every 1.5 s and implemented in the software algorithm are described in detail, while Figure 2.17 provides an overview of the entire procedure.

1. Considering the resampling frequency for the signals visualization (680 Hz, see Paragraph 2.12), a buffer of 1.5 s is composed of 1020 samples. So, starting from the first transmitted data, the pulse wave signals are assembled into two groups of 1020 samples (one for the carotid samples, the other for the femoral samples), as in Figure 2.15.

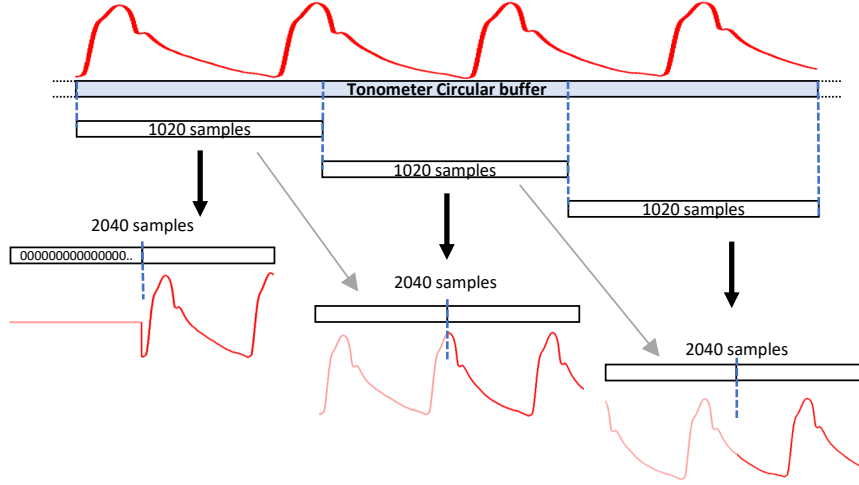


Figure 2.15: First stage of the real-time PWV assessment: pulse wave samples repartition into 1.5 s buffer and merge, for features extraction.

2. In the following, each 1.5 s-segment is merged with the previous one, creating an array of 2040 samples, where only the second half is under investigation. This is done because the adopted digital filters require some transients to stabilize, so in this way it is granted that, on the second half of the buffers, filters are properly working avoiding any distortions. At the beginning, when the very first samples are provided by the acquisition system, an array of 1020 zeroes is added (zero-padding, Figure 2.15).
3. In order to have a system with a high time resolution of the extracted PTT, the tonometer signal is resampled to 2040 Hz through a cubic spline. As a result of this resampling, the signal time resolution is 0.5 ms, which is remarkably higher than before. The adopted interpolation is done through a third-degree polynomial with a forced continuity in the second derivate. Where the new y coordinate is defined, between two known y_j and y_{j+1} considering also their derivatives y_j'' and y_{j+1}'' , as:

$$y = Ay_j + By_{j+1} + Cy_j'' + Dy_{j+1}'' \quad (2.4)$$

With:

$$A = \frac{x_{j+1} - x}{x_{j+1} - x_j} \quad (2.5)$$

$$B = \frac{x - x_j}{x_{j+1} - x_j} \quad (2.6)$$

$$C = \frac{1}{6}(A^3 - A)(x_{j+1} - x_j)^2 \quad (2.7)$$

$$D = \frac{1}{6}(B^3 - B)(x_{j+1} - x_j)^2 \quad (2.8)$$

4. To remove the signal DC-offset, a high pass filter of 4th order with a cut-off frequency of 0.5 Hz is applied (Figure 2.17, box *a*).
5. A 4th order low pass filter at 2 Hz is then applied to identify the numbers of events (blood pulses) that occurred in the 3s-interval under evaluation (Figure 2.17, box *b*). All the relative minimums of the low pass filtered signal are considered as *event starters*, i.e. the array index corresponding to the initial of each blood pulse. Afterward, the *cardiac period* T is defined as:

$$T = \frac{1}{n-1} \sum_{i=1}^{n-1} (\text{eventstarter}_{i+1} - \text{eventstarter}_i) \quad (2.9)$$

Where n is the number of the identified events starters and T represents the number of samples in the mean cardiac period.

6. Starting from each event starter included in the second part of the buffer (i.e. corresponding to the 1.5s under evaluation), only a $\pm T/3$ signal portion is considered, where T is the duration of the cardiac period evaluated in the previous step (Figure 2.17, box *c*). In this interval, all the minimums are identified with the purpose of classifying the ones located at the foot of the pulses rising edges and representing the only ones useful for the intersecting tangent features extraction. A threshold is defined as 50% of the lowest minimum's y-coordinate among all the detected. So, if:

$$y(\min_{(i)}) < \text{threshold} \ \& \ x(\min_{(i)}) > 3059 \quad (2.10)$$

(3059 corresponds to the starting x-coordinate of the considered 1.5s), the relative minimum is saved in the “minimums buffer”.

7. To proceed with the “foot” extraction each blood pulse must be considered separately. For this, starting from every event starter situated in the second half of the signal a window of T samples has to be examined (T -window).

At this point, considering the pulses located in the 1.5s under evaluation, two cases are possible. In the first, the required T samples are available in the investigated buffer (case “a” in Figure 2.16) and the T -window can be identified, continuing the process with the eighth step. Whereas, the second possibility occurs when all the T samples are not in the current array (case “b” in Figure 2.16), meaning that the pulse continues in a next packet of samples not yet available. In this instance, all the samples, starting from the event starter are stored in a special “to append buffer”, (together with the local minimums identified in the previous step) and the process restarts with a new signal segment from the step 1.

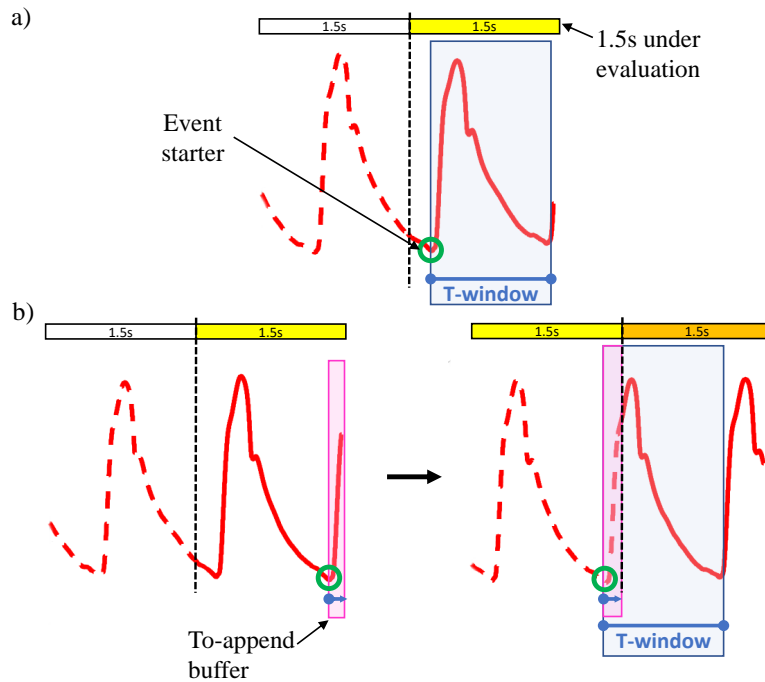


Figure 2.16: a) Case with the T-window totally included in the segment under evaluation; b) On the left, creation of the “To append buffer” for the next 1.5s segment. On the right, union between the “To append buffer” and the actual signal.

For this reason, every time a new packet of acquired samples has to be processed the “to append buffer” is checked. If it is not empty its content will be merged with the current signal and the process continues (Figure 2.17, box *d*).

8. In the selected T-window, the intersecting tangent point extraction is performed. The first derivate of the signal is computed then, starting from each relative minimum extracted in the step 6, the first identified maximum of the first derivate is taken. Once the maximum derivate point is determined, the nearest minimum among all the minimums is taken. The tangent passing through the point of maximum first derivate in the signal and a horizontal line through the minimum are traced. Finally, the intersection between the two lines is projected on the signal and that is the “foot” of the pulse rising edge (Figure 2.13). The foot x-coordinate is saved in carotid o femoral “features vectors”.
9. If both the processing of the carotid and the femoral pulse waves lead to the

feature detection the PTT is evaluated:

$$PTT = foot_{femoral} - foot_{carotid} \quad (2.11)$$

and then the PWV results as:

$$PWV = \frac{distance_{fem-car}}{PTT} \quad (2.12)$$

10. The process restarts from the first step 1 considering a new batch of 1020 freshly acquired samples.

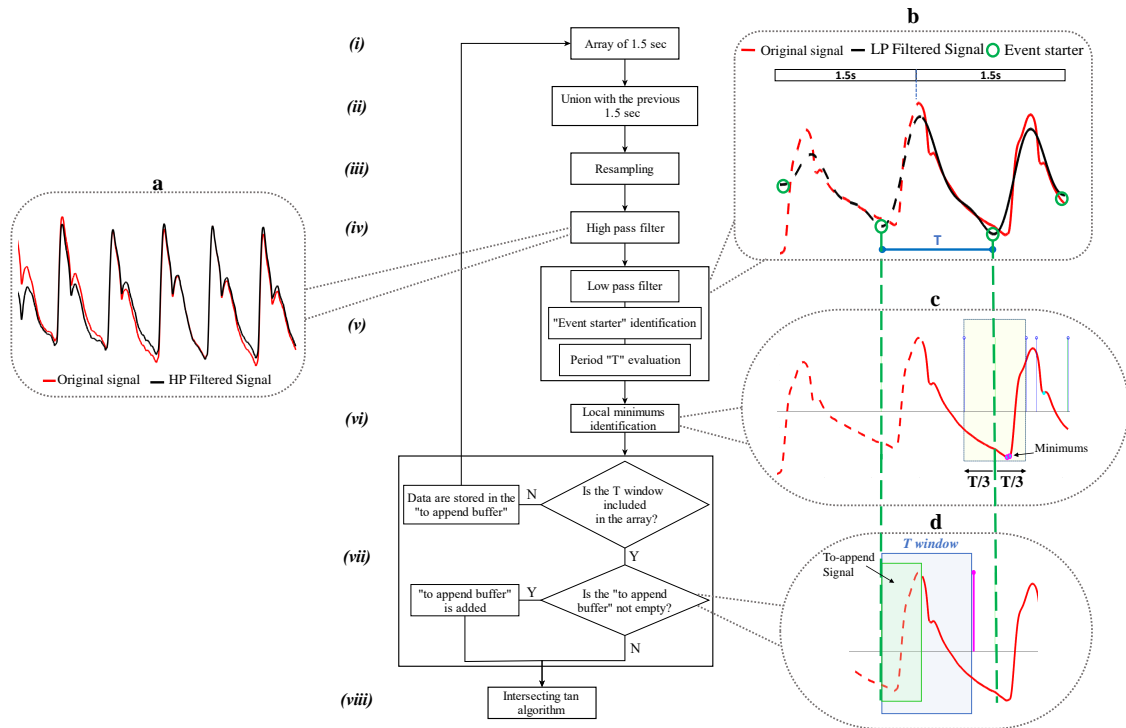


Figure 2.17: Algorithm steps for the real-time "intersecting tangent" feature extraction.

2.4 The PWV acquisition procedure

The ATHOS operator interface was designed in Visual Studio environment, using C# as programming language and DirectX Application Programming Interface. It lets to real-time visualize the acquired signals and to guide the

operator in a good quality PWV assessment through some innovative expedients, that will be explained in this section.

When the software interface is launched, a first “*Study and Patient Data*” window appears (Figure 2.18). In this form, the operator has to insert data regarding the subject under analysis: the identification code (to associate the patient with the trial), the values of systolic and diastolic blood pressures and the cf-distance, i.e. the distance measured between the femoral and the carotid acquisition points. In order to assess the value of the blood pulse velocity, the algorithm considers this cf-distance value multiplied by 0.8, because it has been shown how this value is the most correct and suitable for PWV extraction [48], [49]. Usually, operators perform the distance measurement by using a common tape and projecting in the air the acquisition sites’ positions in order to avoid body protuberances.

Figure 2.18: “*Study and patient data window*” where the operator has to insert the clinical information of the subject under examination.

After this data insertion, the system opens the “*Acquisition window*” (Figure 2.19), to start with the evaluation. If the Bluetooth connection was successful, the play button of the main window is selectable. The user can press it to start to watch the real-time signals. The two pulse waves are displayed by default, whereas, ECG visualization is optional. Signals are drawn on the screen and every five seconds they refresh. The visualization time of each screen can be changed by putting a different duration in the specific box on the window.

To better address a good quality signal acquisition and so a more reliable PWV assessment, the ATHOS interface is provided with a peculiar pulse waves plot: the visualization starts with the zoom only when the signals have an amplitude higher than 400 mVpp. This expedient lets to better achieve a high Signal Noise Ratio of the tonometer signals, which means more stability and less noise corruption in the parameter evaluation. On the other hand, if they have a too large amplitude,

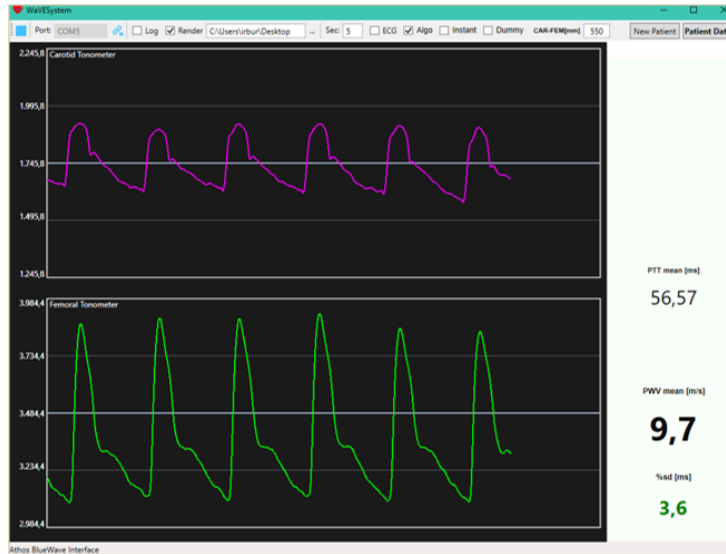


Figure 2.19: “Acquisition window” with a refresh time of five seconds. On the right side of the window the real-time extracted parameters are reported.

they are dynamically refitted on the screen. Moreover, to help the operator to understand the signal quality, two white lines are placed to guide the user to obtain a reasonable signal amplitude in each graph. It is recommended to have a signal that is as big as the amplitude defined by the two horizontal lines. In Figure 2.19 is noticeable how the pink signal (the carotid) is not big enough to be zoomed; otherwise the green (femoral), that is bigger than the white guidelines, does not saturate in the window.

With the purpose of making a GUI useful also for the debug process and for a successive study of the patient data, the *log* and *render* options were added in the main window. With the first, it is possible to store sampled data on a binary file, usable for a potential post-processing. Whereas, the flag “render” lets to freeze the refresh of the screen, while the acquisition continues in the background. When this flag is removed, the visualization of the signals resumes synchronously with the acquisition system Figure 2.20).

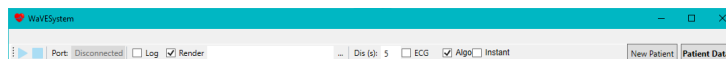


Figure 2.20: ATHOS Graphical User Interface menu bar.

Instead, the command “*algo*” allows the Pulse Wave Velocity algorithm execution (as aforementioned in 2.3.3). As described in detail in the previous

paragraph, each 1.5s a new value of blood pulse velocity is estimated, but it is not the one displayed. In fact, to give a better feedback of the entire acquisition's quality and not only about the instant, the new obtained PWV and PTT values are averaged with the last ten events and then displayed, with the value of the percent standard deviation. So, the mean PWV is the parameter continuously updated, together with the relative percent standard deviation used as key quality factor. If this value becomes green, i.e. if it is below 5% and this means that the acquired parameter is quite stable, it is recommended to press the space bar to generate the report window.

Once the clinical operator has obtained good and stable signals for both the carotid and femoral waves for at least one minute, to finish the acquisition the space bar has to be pushed. With this move, all the bio-signals and the study data (subject ID, distance values, etc.) are stored in the binary file (if the log flag is selected) and the final report is generated. For the PWV evaluation the ATHOS algorithm processes only the last ten seconds of the signals before the acquisition interruption. In addition, considering that the operator must remove the sensors from the subject and press the spacebar for the data storage, the system evaluates the ten-seconds-signals for the final processing discarding the last two seconds.

The “report window” is the final document of the just happened measurement

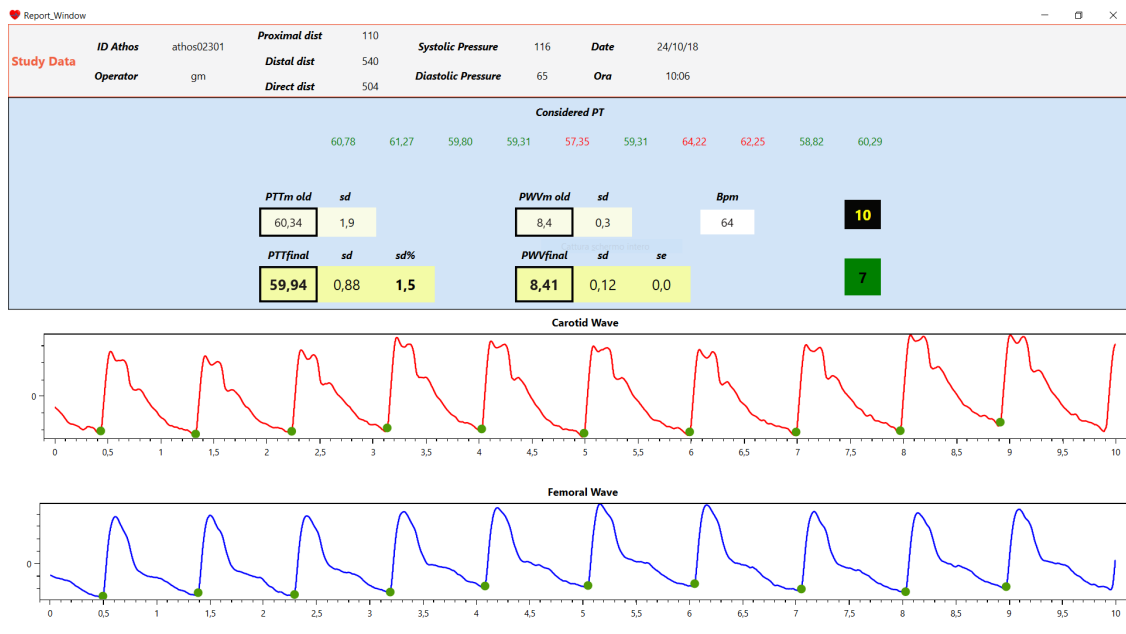


Figure 2.21: “Report window” given by the ATHOS software as final summering output.

(Figure 2.21). It displays the summary of the patient data, the single PTT values obtained on the last ten seconds and the relative averaged PTT and PWV, with their standard deviations and percental standard deviation. To be more comparable as possible with the golden standard, on the PTT values obtained in the ten second under evaluation, the ATHOS system applies the same SphygmoCor discard criterion by removing all the PTT values not included in the range $sd \pm 0.9 * sd$. From these “cleaned” and less scattered PTTs the relative averaged is extracted. The step forward to obtained the final PWV is the division between the femoral-carotid distance, inserted by the operator at the beginning and already multiplied for 0.8 by the system, for this mean cfPTT (as in 1.6).

In particular, the the final report shos the "*PTTm old*", "*PWVm old*", that are the values calculated with the whole intersenting tangent points identified in the ten second under investigation (the exact amount of identified events is written in the black box, i.e. 10 in the example reported in Figure 2.21). But, by applying the standard deviation range restriction, the final values changes and for this are written in "*PTTm new*" and "*PWVm new*", computed among the left over PTTs (the quantity is written in green, i.e. 7 in Figure 2.21).

2.5 System Validation

In order to validate the ATHOS system, thanks to a strict collaboration with “Città della Salute e della Scienza” hospital in Turin, a study was conducted. In this trial, approved by the “University of Turin Bioethical Committee”, the performances given by ATHOS were compared with the one obtained with the SphygmoCor device, that is the clinical reference for non-invasive PWV assessment (as presented in 1.3.1).

For this study 90 voluntary healthy subjects were recruited. Patients aged > 18 years and without any known cardiovascular diseases or antihypertensive therapy were enrolled. Study subjects were then classified into 3 groups based on age: < 30 , 30-59, 60 years old. All underwent measurement of anthropometric parameters such as weight, height and abdominal circumference. Smoking habit, daily alcohol consumption and weekly physical activity hours were assessed. Family history of arterial hypertension, type 2 diabetes mellitus, acute coronary syndrome, ischemic or hemorrhagic stroke, atrial fibrillation, valvulopathies, aortic pathology were evaluated as well. Pulse Wave Analysis (PWA), cfPWV (by reference instrument and ATHOS prototype) and Transthoracic echocardiography (TTE) were assessed on the same day. The exam took place at the Molinette Hospital, AOU City of Health and Science of Turin, Internal Medicine Department, Echocardiography Laboratory. The study was approved by the local bioethics committee of the

University of Turin (protocol number 155412 of 12/04/2018). All the recruited subjects provided a written informed consent.

Table 2.2: Anthropometric and anamnestic parameters of the study population (whole and age-based groups).

Variable (Mean±Sd)	General Population (n=90)	Group <30 (n=30)	Group 30-59 (n=30)	Group ≥ 60 (n=30)
Age	45.6 ±17.8	24.5±2.8 [#]	47.3 ±8.2 [§]	65.1±6.5 [*]
Gender(male,%)	48 (53.3%)	17 (56.7%)	15 (50%)	16 (53.3%)
Weight(kg)	68.2 ±13.6	65.2 ±10.5	68.3±15.2	70.9±14.5
Height(m)	1.70 ±0.1	1.71 ±0.1	1.71±0.1	1.68±0.1
BMI(km ²)	23.4 ±3.5	22.1±1.8	23.2±4	24.8±3.9 [*]
Waist(cm)	87.1±11.4	80.5±7.9	87±10.9 [§]	94.1±10.9 [*]
BSA(m ²)	1.79±0.2	1.77±0.2	1.79±0.23	1.80±0.21
SBP(mmHg)	116±13	113±12	114±13 [§]	120±13 [*]
DBP(mmHg)	72 ±8	68 ±7 [#]	73.1±9	75±8 [*]
PP(mmHg)	44±9	45±8 [#]	41±9 [§]	46±9
MAP(mmHg)	86.6±9.0	83.2±8.0	86.6±9.2	89.9±8.7 [*]
HR(rpm)	66 ±12	68±12	65.5±11	66±12
Smoke	27 (30%)	4 (13.3%) [#]	11 (36.7%)	12 (40%) [*]
Alcool	25 (27.8%)	1 (3.3%) [#]	11 (36.7%)	13 (43.3%) [*]
Sport	68 (75.6%)	19 (63.3%)	25 (83.3%)	24 (80%)
Fam_CV	53 (58.9%)	22 (73.3%)	18 (60%)	13 (43.3%) [*]

BMI: body mass index; BSA: body surface area; Waist: abdominal circumference; SBP: systolic blood pressure; DBP: diastolic blood pressure; PP: pressure pulse; HR: heart rate; Fam_CV: family history for cardiovascular diseases.

[#]: $p < 0.05$ between group <30 and group 30-59;

[§]: $p < 0.05$ between group 30-59 and group ≥ 60;

^{*}: $p < 0.05$ between group <30 and group ≥ 60

Table 2.2 summarizes the clinical and anamnestic characteristics of the volunteers. Population's mean age was 45.6±17.8 years, ranging from 18 to 86 years. Subjects were divided into 3 groups depending on age: age < 30, 30 to 59, and ≥ 60 years old (mean of 24.5±2.8, 47.3±8.3, 65.1±6.5 years, respectively).

Two clinical operators carried out the acquisitions with the two instruments,

interchanging the device between them for every subject (i.e. if for subject 1 the operator A used the ATHOS and the operator B used the SphygmoCor, for subject 2 the operator A was associated with the SphygmoCor and vice versa). Following the study protocol, schematized in Figure 2.22, after the anamnesis information, the two operators identify the best carotid and femoral locations through tactile arterial palpation. Once located, the two spots are marked to be sure that the acquisition sites do not change for the two instruments. Then, through a measuring tape, the femoral-carotid distance is evaluated. As in the standard clinical procedure, this directly measured distance (in mm) is multiplied for a constant equal to 0.8. In fact, S. Huybrechts et al. in [29] explain how thanks to this correction the femoral-carotid distance better matches the real arterial pathway, which is surely different from the one resulting with the linear tape measurement approximation.

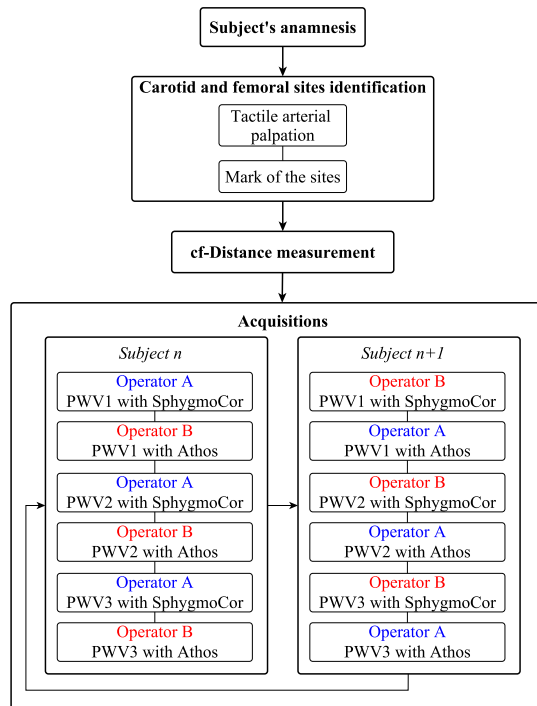


Figure 2.22: Flow chart of ATHOS study protocol [40].

Afterward, the first operator starts with the SphygmoCor two-steps acquisition proceeding with the carotid pulse detection and subsequently with the femoral pulse. When the first PWV assessment is completed, the second operator goes ahead performing the femoral and carotid simultaneous acquisition with the ATHOS device. This procedure will be repeated three times on each subject, both for statistical purposes and also to be aligned with the common practice for

clinical PWV evaluation; indeed, doctors usually consider the actual PWV value as the one obtained after the average of three consecutive acquisitions.

During the ATHOS usage, the operator must address all the reported recommendations oriented to guarantee a reliable PWV evaluation. Firstly, the user has to be sure that the signals have enough amplitude, helped by the smart visualization. In the second place, the operator should check the real-time fluctuation of the PWV value and only when it is stable, with a relative percent standard deviation under 5%, it is suggested to conclude the acquisition. Once the acquisition is concluded, the generated report contains all the extracted parameters and the final cf-PWV, ready to be compared with the SphygmoCor estimation.

2.5.1 Results

The PWV and PTT values of the examined population, assessed with the reference instrument SphygmoCor and with ATHOS are summarized in Table 2.3.

The average cfPWV measured with ATHOS (PWV_{ATH}) and with SphygmoCor (PWV_{Sphy}) is 7.88 ± 1.96 m/s and 7.72 ± 1.95 m/s, respectively ($p = 0.013$). The correlation between the two measurements show a R of 0.959 ($p < 0.001$). The mean difference is 0.15 ± 0.56 m/s (Figure 2.23).

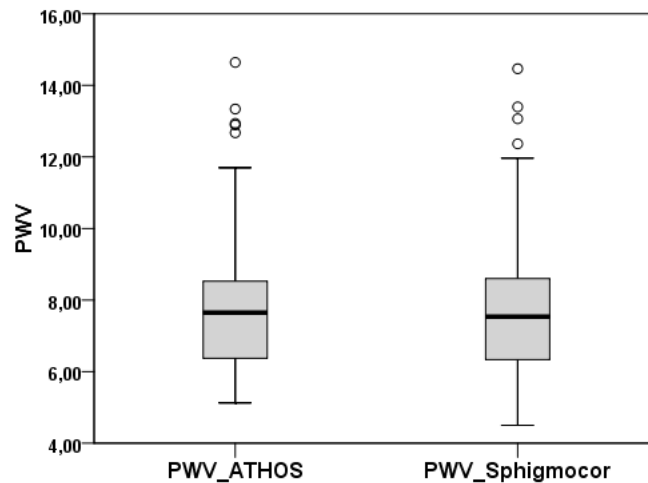


Figure 2.23: Box-plot comparison of PWV from SphygmoCor device ($PWV_{SphygmoCor}$) and the new ATHOS device (PWV_{ATHOS}).

Table 2.3: Pulse wave velocity parameters of the study population (whole and age-based groups)

Variable (Mean±Sd)	General Population (n=90)	Group <30 (n=30)	Group 30-59 (n=30)	Group ≥ 60 (n=30)	p value ANOVA
$PTT_{ATH}(ms)$	64.99±13.6	77.40±9.65 [#]	64.58±8.39 [§]	53.00±9.65 [*]	<0.001
$PWV_{ATH}(m\backslash s)$	7.88±1.96	6.30±0.96 [#]	7.79±1.10 [§]	9.54±2.06 [*]	<0.001
$PTT_{Sphy}(ms)$	66.4±14.77	80.13±12.24 [#]	64.5±8.89 [§]	54.57±9.83 [*]	<0.001
$PWV_{Sphy}(m\backslash s)$	7.73±1.95	6.12±1.04 [#]	7.81±1.11 [§]	9.25±2.07 [*]	<0.001
$\Delta PTT(ms)$	-1.40±5.56	-2.73±6.93	0.09±5.13	-1.57±4.08	0.143
$\Delta PWV(m\backslash s)$	0.15±0.56	0.18±0.48	-0.02±0.58	0.29±0.59	0.104

PTT: pulse transition time; *PWV* pulse wave velocity;
PTT_{ATH}: *PTT* by *ATHOS*; *PWV_{ATH}* : *PWV* by *ATHOS*;
PTT_{Sphy}: *PTT* by *Sphigmocor*; *PWV_{Sphy}*: *PWV* by *Sphigmocor*
 ΔPTT : difference between *PTT_{ATH}* and *PTT_{Sphy}*;
 ΔPWV : difference between *PWV_{ATH}* and *PWV_{Sphy}*;
[#]: $p < 0.05$ between group <30 and group 30-59;
[§]: $p < 0.05$ between group 30-59 and group ≥ 60;
^{*}: $p < 0.05$ between group <30 and group ≥ 60.

The coefficient of repeatability for *ATHOS* and *SphygmoCor* are 0.96 and 1.04 m/s respectively, while the coefficient of variation for *ATHOS* was significantly lower than *SphygmoCor* (3.5% vs 4.3% respectively, $p = 0.01$).

The Bland-Altman plot and the linear regression for *PTT* and *PWV* are showed in Figure 2.24, Figure ??, Figure 2.26, and Figure ??.

If we look at the cases with $PWV \geq 8$ m/s (30 subjects), it is possible to observe a difference between the measured *PWV* values of 0.1 ± 0.63 m/s. While considering the cases with $PWV \geq 9$ m/s (18 subjects) the difference is about 0.04 ± 0.67 m/s.

In other words, there is no statistically significant difference between the mean differences for both *PWV* and *PTT* in the 3 groups ($p = 0.104$ and 0.143 respectively). Meanwhile, examining the 3 groups separately, the two measurements correlated significantly in each group ($r = 0.889$, $p < 0.001$; $r = 0.857$, $p < 0.001$;

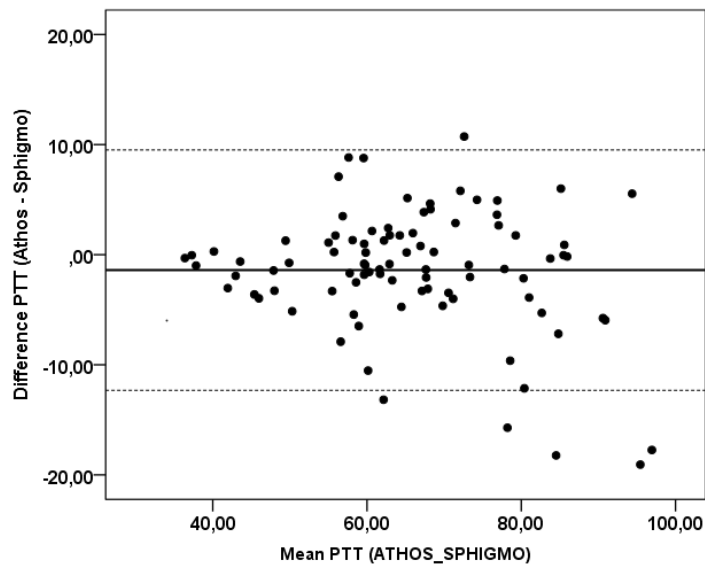


Figure 2.24: Bland Altman plot of the PTT difference between SphygmoCor device and the new ATHOS device.

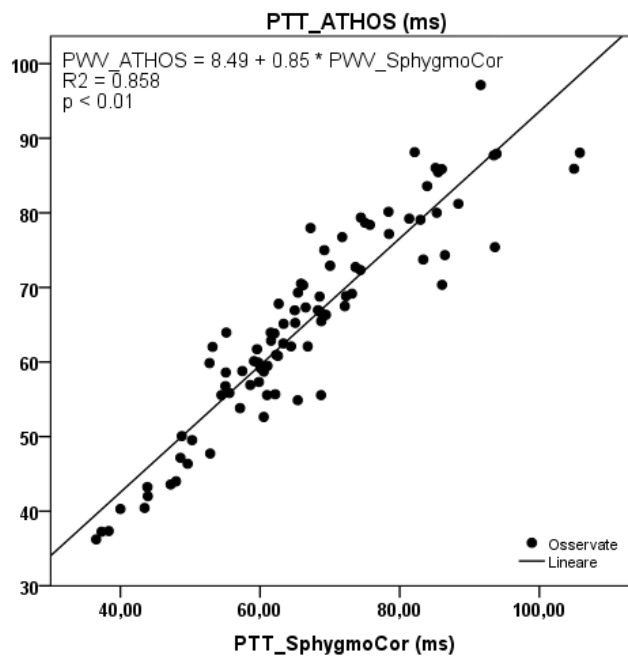


Figure 2.25: Scatter plot with linear regression (solide line) between SphygmoCor device and the new ATHOS device PTTs

$r = 0.959$, $p < 0.001$ respectively). Analyzing possible variables related to the difference between PWVSphygmoCor and PWVATHOS, no anatomic, demographic,

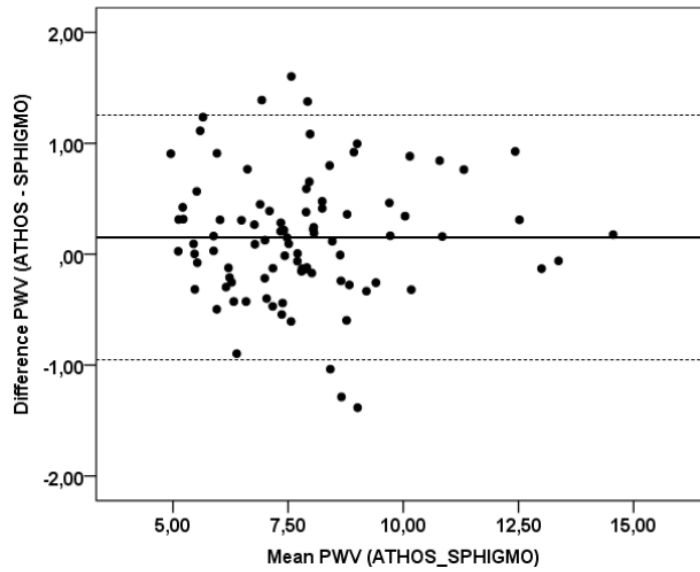


Figure 2.26: Bland Altman plot of the PWV difference between SphygmoCor device and the new ATHOS device.

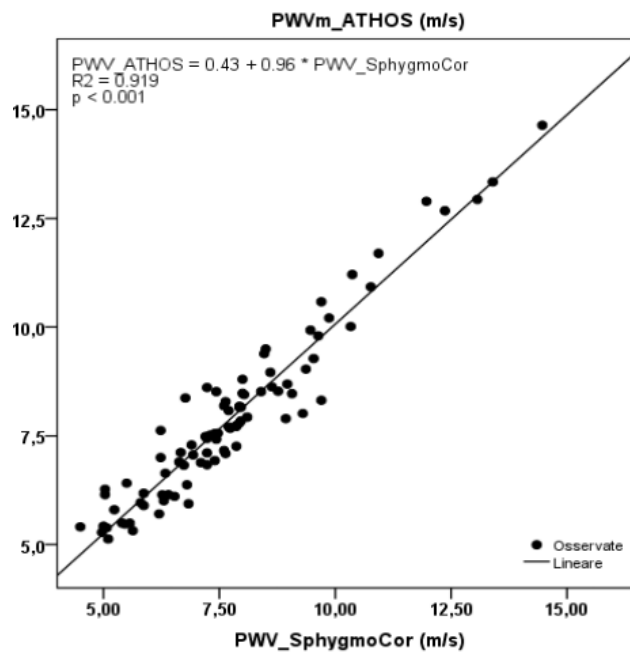


Figure 2.27: Scatter plot with linear regression (solide line) between SphygmoCor device and the new ATHOS device PWVs

echocardiographic or hemodynamic variables resulted to be significant predictors of such a discrepancy.

The reported study has been conducted in order to evaluate the quality, accuracy and reliability of the developed instruments; and according to the operators' feedback, the ATHOS system resulted easier to use with a very fast learning curve.

2.5.2 Results Discussion

The study population included healthy normotensive individuals, within a wide age range, an equal distribution between genders and a wide range of PWV values. We did observe a significant difference in mean cfPWV values between the two devices, probably due to the different way it was assessed. While SphygmoCor use sequential recordings of the waveform with ECG gating, ATHOS allows the non-invasive recording of the pulse wave simultaneously at the level of the carotid and femoral sites, providing a real-time acquired PWV value (obtained from the last 10 cardiac cycles recorded). Nevertheless, there was a strong correlation between the measurements ($r=0.959$, $p<0.001$) and furthermore this difference did not hinder the excellent accuracy of the ATHOS readings.

The ARTERY Society guidelines for the validation of tools for PWV measurements defines three classes of accuracy (poor, acceptable and excellent) based on the mean difference and the corresponding standard deviation [50], as reported in Table 2.4.

Table 2.4: Classes of accuracy following the Artery Society Guidelines.

Accuracy	Mean Difference (m/s)	Standard Deviation (m/s)
Excellent	<0.5	≤ 0.8
Acceptable	< 1	≤ 1.5
Poor	≥ 1	> 1.5

In our study we found an excellent level of accuracy, with an average difference of 0.15 ± 0.56 m/s: in fact, ATHOS slightly overestimated the values compared to the SphygmoCor. In addition, the accuracy between the two methods remained “excellent” also considering the different age groups (<30 , $30-59$, ≥ 60 years, Table 2.3).

It has also to be underlined as both the software were put in the same condition for the time of analyzed signals(ten seconds), same algorithm for the feature extraction(ITP, intersecting tangent point) and same PTTs filtering and restrictions (as previously described). What they mainly differ for is the procedure:

the ATHOS does the simultaneous acquisition of femoral and carotid pulse, meanwhile the SphygmoCor performs them separately. But, despite this, our instrument resulted to be more than comparable with the SphygmoCor and also with a better usability according to the clinician operators.

In a recent review, Milan et al.[22], validation studies of the commercial devices for the non-invasive measurement of PWV were compared. It was shown that accuracy between the methods under examination significantly decreased for cfPWV values $> 8\text{m/s}$. In our cohort, the average difference between SphygmoCor and ATHOS remained in the “excellent” range even for those cases. Moreover, if we compare the technologies reported in Table 2.5, the performances obtained by our prototype are satisfactory. The validation study resulted to be a significant proof about the obtainment of a truly cost-effective system that addresses fully reliable and easy to perform PWV estimations with the ambition to expand the availability of this measure and the fields of application.

Table 2.5: Validation studies of the commercial devices compared with ATHOS.

Devices	Reference Device	Subjs	Age	T Time	PWV _M Device	PWV _M Reference	Δ PWV _M	Accuracy level
ShpygmoCor	Invasive validation	135	60±12.5	ITP	8.7±2.2	8.5±2.4	-0.2±1.55	Poor
SphygmoCor Xcel	SphygmoCor	88	46±20	ITP	7.04±1.72	7.02±1.88	0.01±0.71	Excellent
PulsePen	Millar Tonometry	68	51±20	IIA	8.17±3.45	8.34±3.47	0.17±0.64	Excellent
Complior	SphygmoCor	107	47±16	ITP	8.6±2.6	8.6±2.5	0.0±0.7	Excellent
Aortic	SphygmoCor	85	46	ITP	6.96±1.84	7.0±1.54	0.04±0.3	Excellent
Arteriograph	SphygmoCor	63	48±15	NA	8.0±2.16	7.68±1.58	-	-
Vicorder	SphygmoCor	122	53±18	MSDA	8.3±2.2	8.6±2.9	-0.3±1.5	Acceptable
pOpmètre	SphygmoCor	86	53±20	MSDA	8.77±2.36	8.74±2.15	0.22±2.46	Poor
ATHOS	SphygmoCor	90	45.6±17.8	ITP	7.88±1.96	7.73±1.95	0.15±0.56	Excellent

Data are mean±SD; ITP: Intersecting Tangent Point method, IIA: Intersecting Interpolating Algorithm; NA: Not available; MSDA: Maximum of the Second Derivative Algorithm; PWV_M: Mean Pulse Wave Velocity; Subjs: Enrolled Subjects; T Time: Transit Time; - Means PWV difference and/or SD was not reported.

Chapter 3

PWV with Phonocardiogram

The first attempt to have a wearable system able to continuously monitor the PWV value has been done using the ST MEMS microphone, already introduced in Paragraph 1.4.3. This sensor, if placed on the skin in proximity of an artery (carotid and femoral in the case under analysis) lets to the record all the murmurs produced by the blood pulse propagation. With an ad hoc electronics and an appropriated algorithm, it has been tried to use this technology to develop a system for non-invasive PWV assessment. Finally, these results were compared with the ones obtained with the golden standard methodology, the applanation tonometry by using ST tonometers, as ATHOS does (see Chapter 2).

This chapter is structured as follow: in the first part the hardware of the device is detailed, the second presents the software with the signal processing and, in the last, the validation results are shown.

In particular, the idea of this phono-system consists of a main unite, that acquires data from the carotid and femoral microphones hold by two bends, and that transmits them to a laptop for the signal visualization and processing (Figure 3.1).

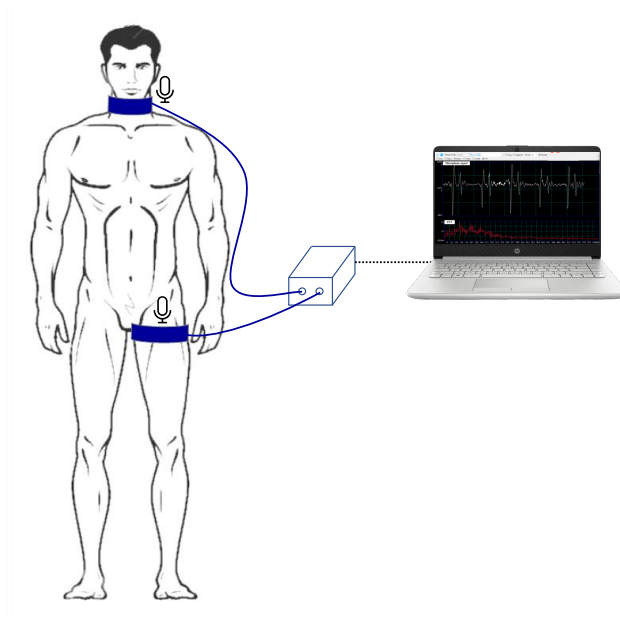


Figure 3.1: The project for the PWV assessment through phonocardiogram signal.

3.1 Hardware implementation

After several tests that implemented different mechanical configurations (one or more microphones and different structure shapes), the best performing one presents a single microphone sensor placed in an appropriate 3d-printed support. As reported in Figure 3.2a, this has two main peculiarities: a cavity where the sensor has to be placed for keeping it stable during the acquisition and a considerable thickness to let the sensor to be well pressed on the skin for a better pulse finding.

As said before, the goal of this part of the PhD project was to have a stand-alone system, that permits to have a reliable PWV assesmente without being corrupting by the operator ability. For this, the support has been placed in two bands, one for the neck and the other for the groin respectively (Figure 3.2b).

Beyond the mechanical part, also the electronics has been adapted to maximize the quality of the acquisitions, especially the signals. In fact, as said in Paragraph 1.2.3, PCG has a frequency band between 0.3 and 200 Hz; for this a band pass filter between this two has been designed. Figure 3.3 reports the flow chart describing all the steps done in the analog conditioning.

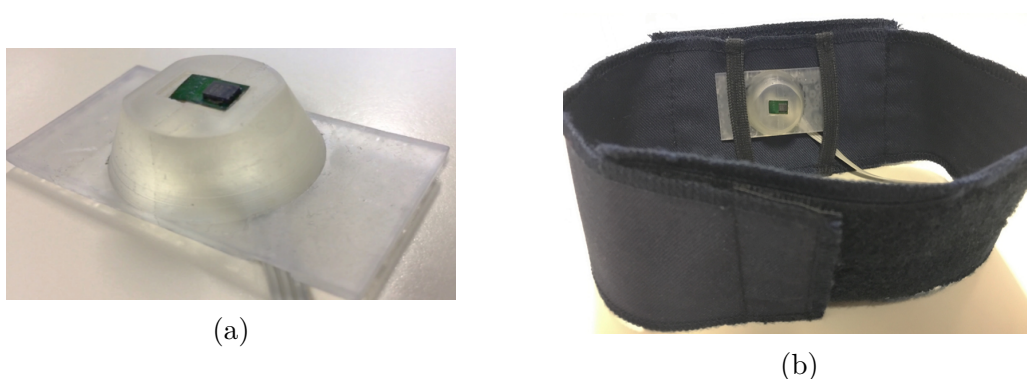


Figure 3.2: Sensor configuration for the phonocardiogram acquisition. (a) 3d-printed support with the MEMS analog microphone; (b) Final acquisition configuration band, where the support can be placed.

The circuit has been assembled with two main components:

- *TLV2464 opAmp*: a low power, four channels, operational amplifier with rail-to-rail input/output with a voltage supply up to 6 V, a gain bandwidth product of 6.4 MHz, and an input voltage offset of 100 μV ;
- *LM317 Adjustable Regulator*: to provide a voltage reference for the amplification and filtering stages, along the amplification chain a reference of 1.5 V is chosen according with the ADC dynamic range that is 3.3 V.

The stage *a* in Figure 3.3 corresponds to a high pass filter with a cut-off frequency given by the components reported in Figure 3.4 and equal to:

$$f_c = \frac{1}{2 * \pi * C * R1} = \frac{1}{2 * \pi * 10 \mu\text{F} * (47 \text{k}\Omega + 10 \text{k}\Omega)} = 0.27 \text{ Hz} \quad (3.1)$$

Meanwhile the second stage, *b*, consists of a unit gain second order low pass filter with a cut-off frequency of 200 Hz.

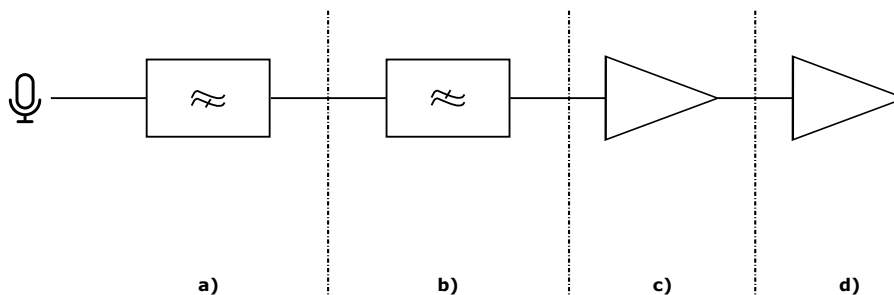


Figure 3.3: Microphone analog signal conditioning diagram.

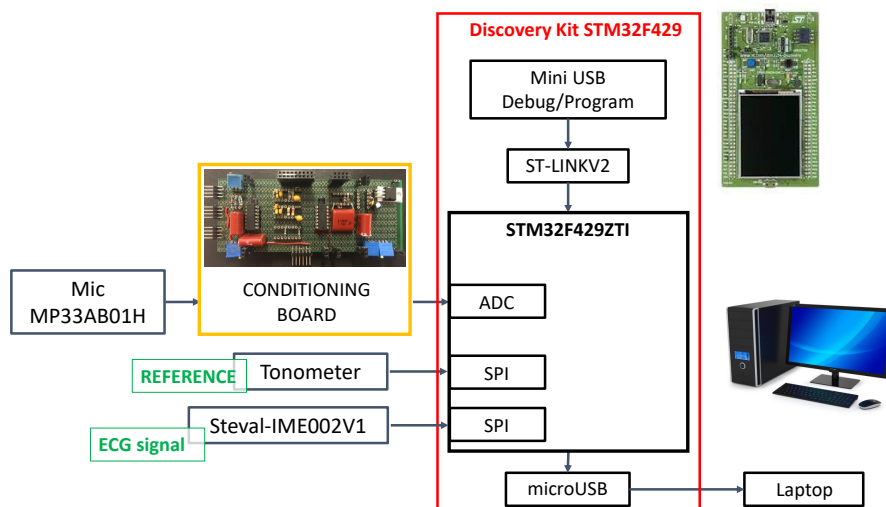


Figure 3.5: Interconnections diagram of the PCG system.

value. This signal is routed to the MCU and configured as interrupt service request.

A specific interrupt service routine is called every time a new ECG sample is present: all the signals are stored by the MCU from ECG's SPI and ADCs. Therefore, every interrupt, samples from ECG and Microphone are collected. The tonometer always works at a maximum frequency of 180 Hz, so it can be read every 11 ECG interrupts (obtaining a 177.5 Hz sampling frequency). Later, at software level this signal will be conveniently resampled.

The final goal of this work was to evaluate the time interval between two simultaneous acquired signals, so it is of primary importance that conditioning circuit introduces a negligible time delay. This time transposition is usually due to the low pass filter (delaying signal) and high pass filter (introducing negative delay) processing.

In order to evaluate the amount of introduced time delay, every conditioning channel has been individually tested. A reference signal is generated and the time difference between the original one and the same after it passes through the conditioning chain is measured. The obtained values are:

- 1.5 ms for ECG signal due to the STEVAL-IME002V1 Board;
- -2 ms for PCG signal due to the circuits.

By comparing this results with the time interval that have to be measured (PTT is in the order of magnitude of 100 ms), the implemented conditioning circuit is a

good compromise between reasonable cut-off frequency and the introduced time delay.

3.2 Signal Analysis

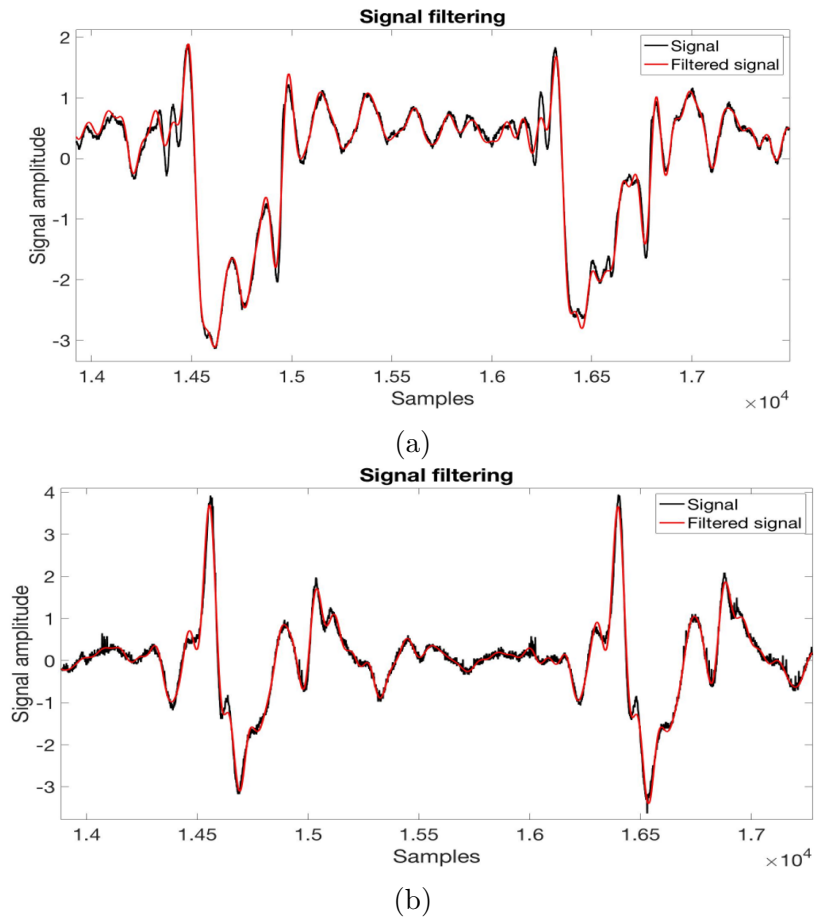


Figure 3.6: Typical signal acquired by the phonocardiogram system. (a)Carotid signal before and after the filter (b)Femoral signal before and after the filter.

Thanks to a specific Graphical User Interface (a modified version of the ATHOS, see Paragraph 2.3) the acquired signal can be continuously checked for the right placement identification. When the blood pulse propagation was clearly visible in the phonocardiogram it is considered a good acquisition.

The use of PCG signal for Pulse Wave Velocity evaluation is totally a new experimental approach and there aren't in literature information about features extraction. Fort this reason, the first step of this work was based on a frequency

components analysis in order to just isolate the band of interest. A Fast-Fourier Transform (FFT) was applied at both Carotid and Femoral signals and it has been noticed that the most significant frequency components are limited under 70 Hz. To eliminate the high frequency noise and the low frequency signal oscillation a filter between 2 and 70 Hz was implemented, the resulting signals are shown in Figure 3.6.

As could be observed in Figure 3.6, despite the shape is not similar to the usual pulse wave achievable by the reference tonometric technique, both the phonocardiograms present a clear peak in correspondence of the blood pulse passage. Hence, the idea was to use that part of the signal to extract a feature that lets to identify the interval time between the two sites, and so the Pulse Wave Velocity. In particular, signal features individuation is made at the top of this rising edge, because it corresponds at the wave portion less distorted by noise and so very repeatable.

In particular, in this case a new feature similar to the intersecting tangent point, described in Paragraph 2.3.1, has been created: the *ear intersecting tangent point*. This corresponds to the projection on the signal of the intersection between the axis passing through the maximum at the beginning of the signal falling and the tangent through the minimum derivative point of the front.

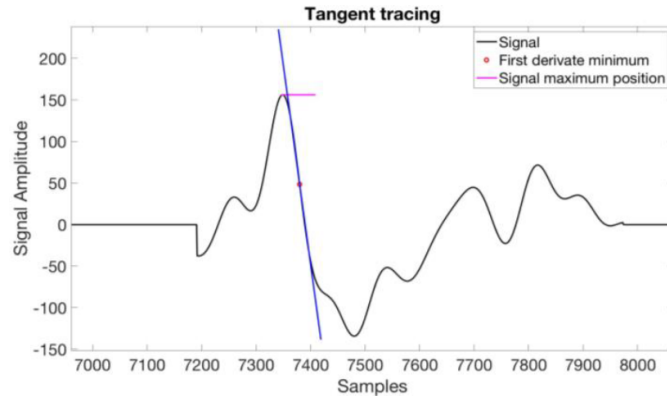


Figure 3.7: "Ear tangent point" extraction in a phonocardiogram pulse: intersection between the axis passing through the maximum and the tangent to the poin of minimum derivative.

3.2.1 Frequencies analysis

Using this feature several tests were done comparing the PTT obtained with the "ear" ITP for the phonocardiogram and the traditional Intersecting Tangent

Point (ITP) for the tonometer, keeping the same point for the acquisition sites. The results were not so encouraging, pushing us to find another way to approach the sound signal. Hence, we analyzed the signal and its component trying to distinguish the part do to the displacement moving and the one due to the pure sound recording.

As explained in Paragraph 1.4.3, the MEMS microphone sensor is essentially a variable capacitor. In detail, its transduction principle is based on a change in the capacitance between a fixed plate and a membrane. So, it transforms a perturbation of the atmospheric pressure (i.e. sound) into an electrical quantity. In this work, a capacitive MEMS microphone is adopted and placed in contact with the skin, whose pressure variation, due to mechanical mass vibration, is transformed into a capacitance variation. In this way, the capacitance alteration is generated both by atmospheric pressure and by skin translation, together resulting from the artery physical movement caused by the pulsatile blood flows.

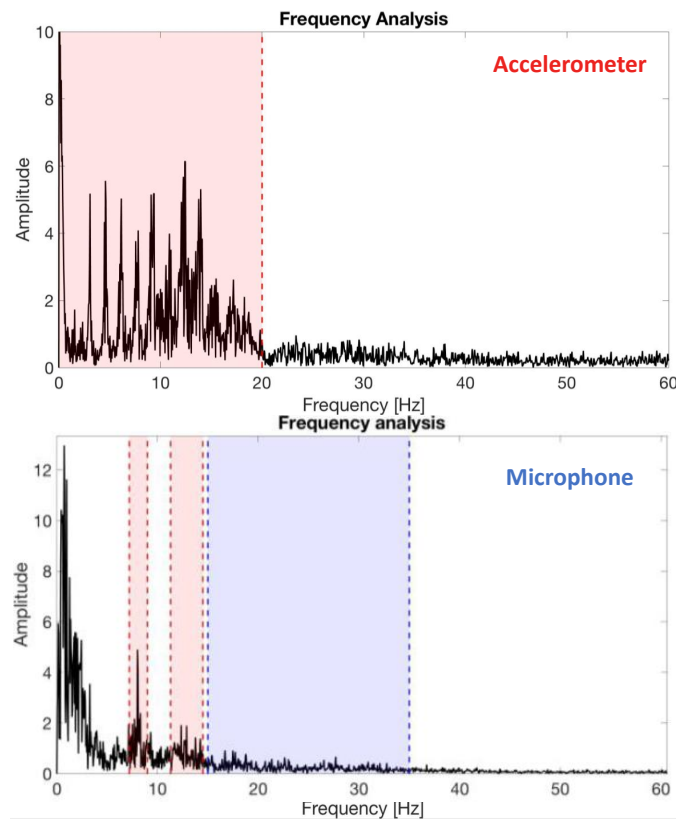


Figure 3.8: On the top: displacement frequency analysis through Fast Fourier Transform; On the bottom: sound frequency information content.

To discern these two components of the detected signal (the sound and the

vibration) a new experiment was conducted. We introduced two instruments: an accelerometer (LIS2DS12, STMicroelectronics, Geneva, Switzerland) and a high sensibility microphone (Brüel & Kjær 4943, serial number of 264565). In particular, since accelerometer sensor is located in contact with the skin, it lets to acquires displacement signal. On the other hand, the high sensibility microphone, unlike the accelerometer, is placed close to the skin but without contact, so it can record only sound. By doing so, each signal components can be analysed separately. They were both used to acquire the signal from the carotid and the relative frequency components were evaluated.

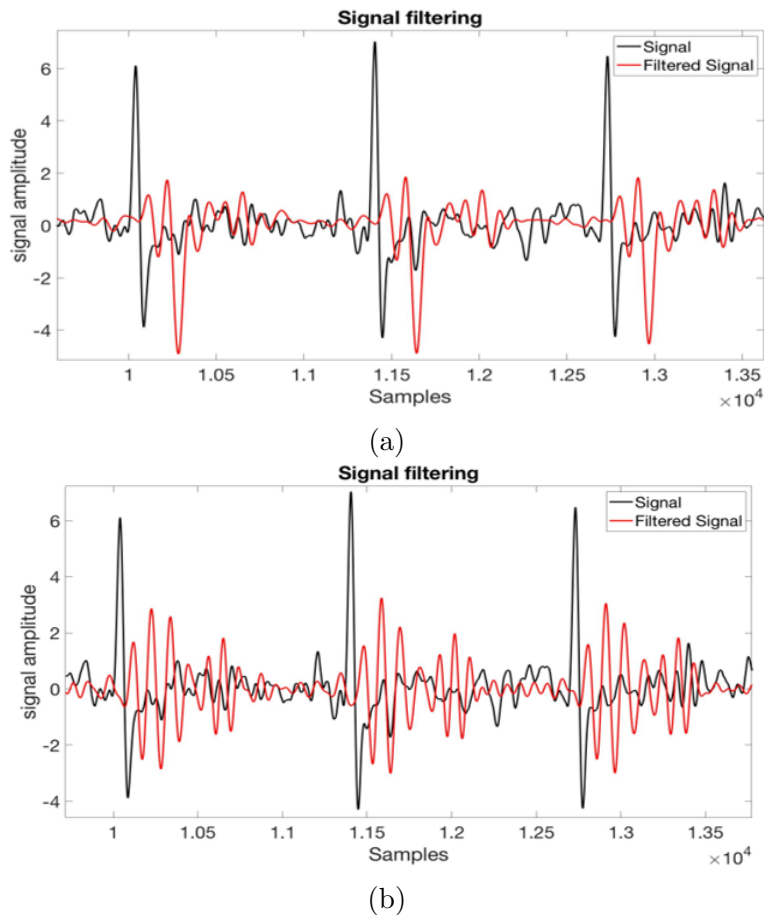


Figure 3.9: Plot of the two components forming the signal detected by a microphone on the skin in proximity of an artery: (a) Displacement contribution between 8 and 12 Hz and (b) Sound components, 13 to 35 Hz.

In Figure 3.8 is represented the developed frequency component analysis through Fast-Fourier Transform (FFT) of the signal obtained by the accelerometer, where it is possible to notice that the main information content is limited

under 20 Hz. Meanwhile, for what concern the sound acquisition, as it is possible to see in Figure 3.8, the main information content is limited under 35 Hz, but the signal has two frequency components also around 8 Hz and 12 Hz. Hence, the low frequency contribution (8 Hz and 12 Hz) are present on both the Accelerometer and Brüel&Kjær4943 acquisitions.

So, either the phenomena is considered from the pure sound point of view or it is considered from the pure movement aspect, the conclusion is that 8 Hz and 12 Hz contributions are still present and cannot be explicitly associated to the sound or the movement component. This is an important indication for the signal processing approach that have to be adopted on the MEMS microphone configuration. The better results are expected to be achievable using the movement component of the signal. Thus, in order to avoid any sound related contribution, the band 8 Hz and 12 Hz should be removed from the MEMS microphone acquisition.

Thanks to this analysis, it was deduced that the MEMS Microphone signal can be divided in two different frequency ranges mainly containing displacement contribution rather than sound components. These intervals are respectively set between 0.5 and 20 Hz for movement, without 8 Hz and 12 Hz components (Figure 3.9a), and from 15 to 35 Hz (Figure 3.9b) for sound. For the shake of simplicity, signals are renamed as Displacement and Sound respectively, even if it is not full formal and accurate classification.

3.2.2 Shape repeatability and feature extraction

Dividing the acquired signal in the sound and displacement components for both the carotid and femoral sites, the one that was more reliable in term of repeatability was chosen. As it can be observed in Figure 3.10 the displacement pulse wave, i.e. the signal acquired by the microphone and filtered between 0.5 and 20 Hz, resulted to be the most stable in the signal fraction that could be use for the temporal identification of the blood passage.

Once the displacement signal was chosen, different features were compared in both the falling and rising part to identify the most reliable. In particular for each rising and falling edges one at the bottom and one at the top was considered (see Figure 3.11):

- *ear-right intersecting tangent point*, located at the top of the right greatest front respect to the absolute minimum;
- *foot-right intersecting tangent point*, located in the lower part of the right greatest front respect to the absolute minimum;

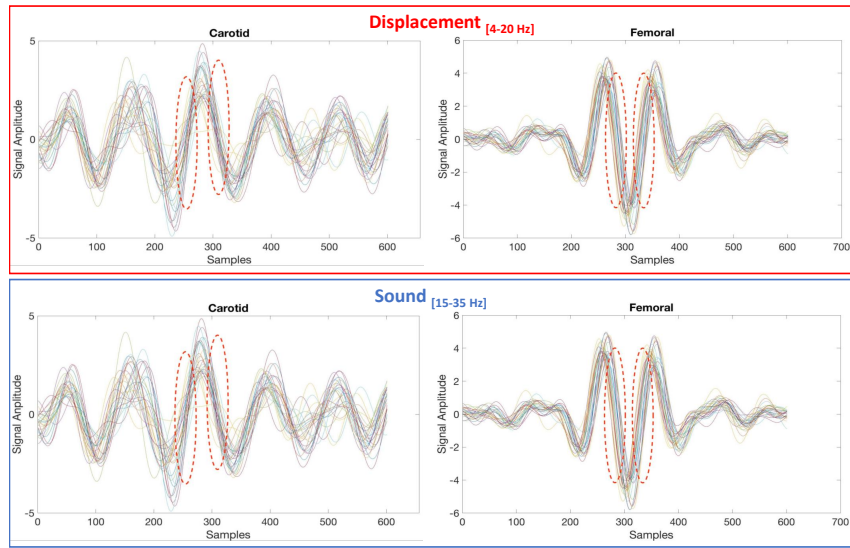


Figure 3.10: Shape repeatability analysis of displacement and sound signals, in red are circled the zone under evaluation, where the blood passage is more detectable and the features will be extracted.

- *ear-left intersecting tangent point*, located at the top of the left greatest front respect to the absolute minimum;
- *foot-left intersecting tangent point*, located in the lower part of the left greatest front respect to the absolute minimum.

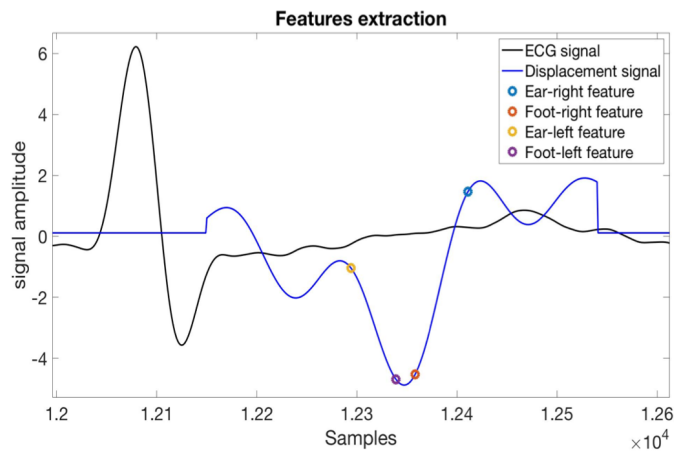


Figure 3.11: The features considered and their locations in the sound pulse wave.

They all differ for the lines used for the intersection, the fronts identification, and first derivative minimum or maximum calculation. In case of left “ear” and

left “foot” features, the first derivate minimum is taken, while for the right “ear” and right “foot” features, the first derivate maximum is selected.

After several test, the “Foot-right” resulted to be the one more reliable probably because it is identified around the minimum of the pulse, the part usually less corrupted by noise.

3.3 Validation Results

The intersecting tangent point evaluated on the greater front of the Displacement Pulse Wave, seemed to be a good way for PWV parameter estimations. But, despite the improvements done considering firstly only the low frequencies of the signal and secondly the foot of the right rising front as the feature, in some cases the detected value was still not fully in line with the reference one (obtained by using Tonometer signal as ATHOS does, Chapter2). After several attempts and analysis we figured out then when the frequency bands of the signal are well separated, the computed PTT is good. While, when the level of noise is such that low frequency band are not well distinguishable then the extracted PTT values differ from the expected.

For this reason, a sort of SNR parameter, based on Fast Fourier Transform analysis, has been introduced to discriminate those undesired situations. This Quality Factor (QF) is obtained as:

$$QF = \frac{signal[(0.5 \text{ Hz} \div 22 \text{ Hz})]^2}{signal[(25.5 \text{ Hz} \div 47 \text{ Hz})]^2} \quad (3.2)$$

Specifically, the signal power computed in the 0.5 to 20 Hz range is divided by the signal power computed on frequency higher than 40 Hz. The computed QF value, updated every 3 seconds, is displayed on the Graphical User Interface running on the control laptop. It is expected that acquired samples will provide reliable results when QF value is greater than 30.

After the last improvement the phonocardiogram system was ready to be validated compered to the golden standard sensor: the applanation tonometry. To do this in the specific 3D-support, place in the band as previously explained, were placed together the MEMS microphone and the MEMS tonometer (Paragraph 1.4.1) and they were simultaneously acquired with the system, described in Paragraph 3.1, at the carotid and femoral site. At least, three acquisitions of thirty second were done and once collected the two signals have been post-processed in

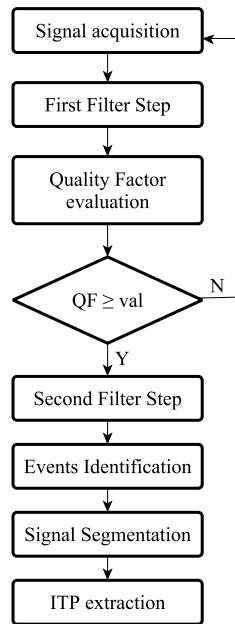


Figure 3.12: Flow chart of the phonocardiogram signal post-processing. *For ITP is meant the Intersecting Tangent Point algorithm; for val a threshold value for the Quality Factor(QF), usually 30.*

Matlab to extract the cfPTT of both.

In particular, for what concerned the PTT tonometric pulse wave, it has been evaluated considering the intersecting tangent point for each pulse extracted following the same procedure implemented by ATHOS system (Paragraph 2.3.3) with the only difference that has been performed in post-processing and not in real-time.

On the other hand, the PTT sound pulse wave has been obtained following these steps, summarized in Figure 3.12:

1. The carotid and femoral sound signals are simultaneously acquired by two MP33AB01H with a sampling frequency of 1953 Hz and filtered by the conditioning circuit between 0.3 and 200 Hz;
2. The post-processing begins with the isolation of the displacement band frequency through two filters of 4th order at 0.5 and 20 Hz respectively. Also in this case, as for ATHOS, it was chosen to apply zero-phase forward and reverse biquadratic filter (Paragraph 2.3.2);
3. The QF is evaluated through equation 3.2, if this condition is satisfied the algorithm continues otherwise a new acquisition is required;

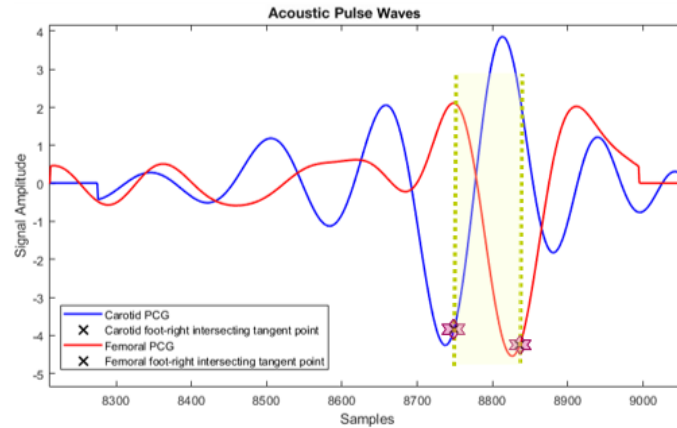


Figure 3.13: Carotid-femoral PTT with ITP features in phonocardiogram signals.

4. Other three filters are done to surely isolate the right component of the signal, a high pass at 4 Hz, a low pass at 20 Hz and a notch at 8 Hz (this last one is done because it was noticed that this component is well observable also in the sound part of the signal and this could interfere with the further evaluation);
5. A low pass filter at 1.5 Hz lets to isolate all the recorded pulses;
6. The signal is segmented with fixed windows, center every event, and the absolute minimum in the window is considered; from it, the biggest rising front on the right is considered for the foot feature extraction;
7. The intersecting tangent point for each pulse is so obtained, for both the carotid and the femoral acquisition. The final subtraction of the associated features lets to obtain the final PTT through the MEMS microphone signal (see Figure 3.13).

In Figure 3.14 are reported two resulting acquisitions. In particular, Figure 3.14a depicts a carotid detection of both the tonometer and phonocardiogram signal, and the relative ITP extraction. On the other hand, in Figure 3.14b the femoral signals and features are reported.

As it is possible to see in Table 3.1, data obtained with the controlled acoustic signal have a lower variability, both referring to the ECG and also in the direct carotid-femoral measurement (standard deviation in the order of 2-3 ms). For what concerned the electrocardiogram, it gives the reference time of the pulse start through the R-peak (as said in Paragraph 1.2.1) and this has been detected through Pan-Tompkins QRS detection algorithm [51].

The main achievement is a sensibly reduced discrepancy between PTT values given by Acoustic Pulse Wave and the Pressure Pulse Wave. For these reasons, it

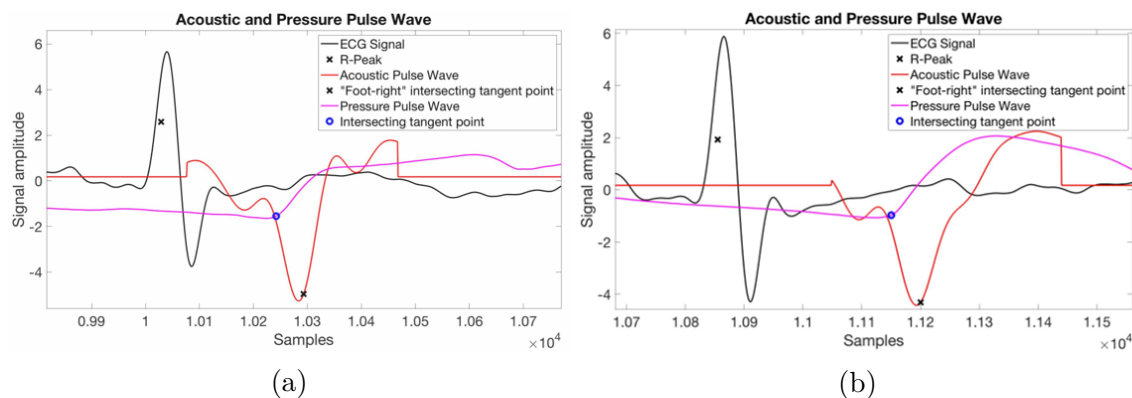


Figure 3.14: (a) Carotid and (b) Femoral simultaneous acquisitions with tonometer and microphone, and relative extracted features.

is possible to conclude that Microphone signal, properly filtered, can be considered a reliable approach for PWV parameter extraction.

All this approach for the Pulse Wave Velocity assessment through sound signal analysis has been proposed and submitted as Patent.

Table 3.1: PTT evaluation with the phonocardiogram compared to the tonometer reference.

Acquisition	Parameter	Respect to R-peak		Microphone	Tonometer
		Carotid	Femoral		
1	PTT(ms)	139.16	189.7	51.06	51.02
	st.dev.(ms)	2.8	2.66	2.57	3.3
	QF	53.67	433.24		
2	PTT(ms)	138.9	194.36	54.10	54.33
	st.dev.(ms)	2.99	2.76	1.65	2.9
	QF	70.3	350.95		
3	PTT(ms)	137	190	53.34	50.07
	st.dev.(ms)	2.86	3.08	1.58	2.69
	QF	49.88	423.56		
4	PTT(ms)	142.86	195.45	52.82	52.25
	st.dev.(ms)	3.47	3.57	2.29	2.62
	QF	60.45	545.22		

PTT: Pulse Transit Time; *st.dev*: standard deviation;

QF: Signal to Noise Ratio of the acquisition evaluated as in equation 3.2;

Chapter 4

PWV with Photoplethysmography

Among all the sensors investigated during my PhD, some of them were chosen in order to find the right one that would simplify the PWV measurement. With the software realized in ATHOS, in fact, it is possible to completely change the vision that is limiting the PWV usage as useful clinical parameter, obtaining a measurement in a faster way on a side and in a continuous mode on the other. This could deeply open the possible application of the parameter and its spread in several medical field, not only as a cardiovascular risk stratification factor, that is the original scope for what this velocity has been initially addressed, but with various illnesses (i.e. fluid therapy and chemotherapeutic response).

To better compare which sensors results to be the most compliant with the compactness and stand-alone requirement, aimed at a wearable device that does not need the constant operator presence, in this part of the work a system that allows the simultaneous acquisition of all the known sensor for pulse wave detection was designed. In particular, the main compared methods were:

- *applanation tonometry* with the ST MEMS tonometer (Paragraph 1.4.1), golden standard technology for this application, already adopted in the ATHOS prototype examined in depth in Chapter 2;
- *acoustic detection* with the ST MEMS analog microphone (Paragraph 1.4.3), an innovative approach that included the development of an ad hoc algorithm and led to a system described in Chapter 3;
- *photoplethysmography* with two different sensors (ST physiological probe, Paragraph 1.4.2, and a commercial one, Paragraph 1.4.2), that is the traditional way used in several commercial application to detect the blood pulse through light absorption;

- *electrocardiography* with was taken as the reference to identify the start of blood pulse propagation.

All these methodologies are managed by the same system, specifically designed for this purpose, and the obtained data are sent to a laptop where a new version of the graphical user interface (already introduced in Paragraph 2.3) lets their real-time visualization and collection. An overview of the system is reported in Figure 4.1.

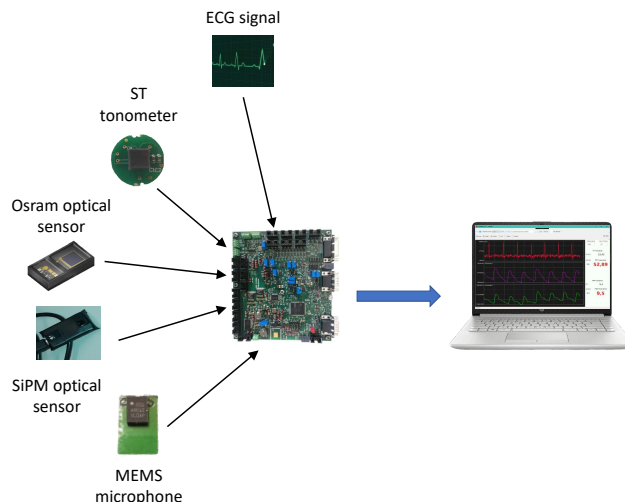


Figure 4.1: An overview of the system: all the considered sensors, the unit for their acquisition and the laptop for the data collection.

4.1 System Hardware

In Figure 4.2 is represented the specifically realized PCB acquisition board, that lets to simultaneously acquire all the signals. It is mainly based on three different devices:

- *STM32H743ZIT6 Mirocontroller* (STMicroelectronics, Geneva, Switzerland) for the tonometers, both the optical sensors and the microphones acquisition. It has an Arm Cortex M7 RISC of 32 bit and can work up to 480 MHz, more than six SPI interfaces, four I²C, two 12-bit ADC, twelve general-purpose timers etc.;
- *ADS1299 Analog to Digital Converter* (Texas Instrument, Dallas, Texas), interfaced with the main MCU lets the differential digital conversion of the ECG, PPG and PCG signals. It is a sigma-delta converter with 9 input channels

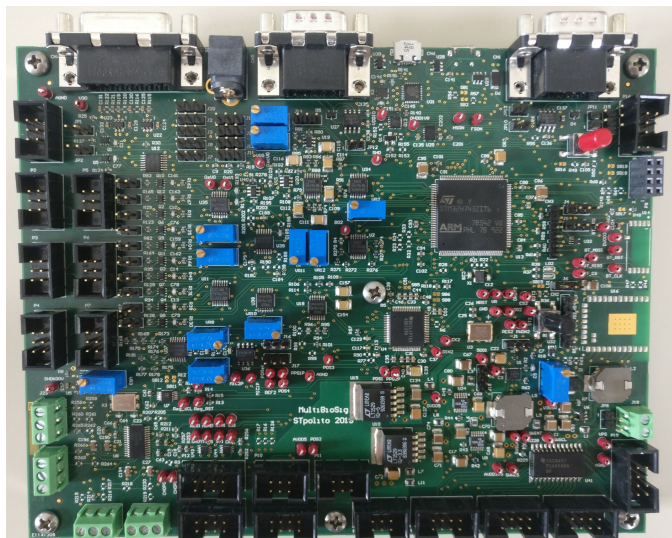


Figure 4.2: Acquisition board configuration.

and PGA(Programmable Gain Amplifier), internal oscillator, 4 GPIO pin and an SPI interface;

- *integrated USB interface* for the data transmission to the laptop.

In Figure 4.3 is reported the scheme that shows the interconnection created in the acquisition board for signals acquisitions and the main components. In the following paragraphs, each signal handling will be treated separately.

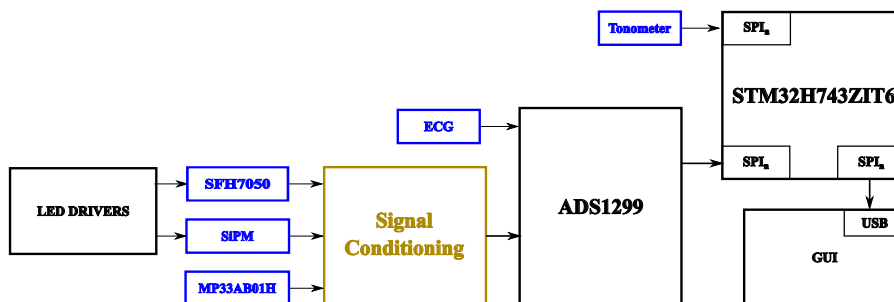


Figure 4.3: Acquisition board diagram.

4.1.1 Photoplethysmogram signal Acquisition

Figure 4.4 reports the flow chart describing all the main steps done in the analog conditioning circuit for the photoplethysmogram signal conditioning, both Osram and SiPM.

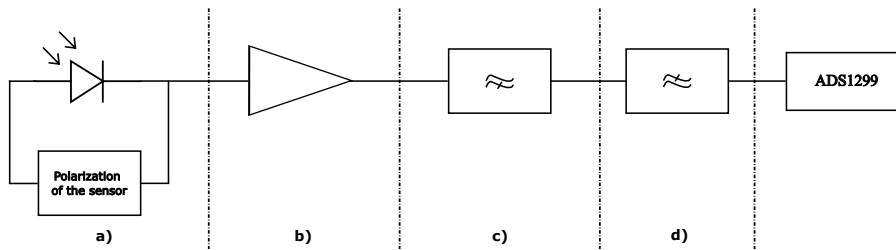


Figure 4.4: Optical sensor analog conditioning diagram.

Although the steps are similar in the purpose, the two sensors undergoes two different electronics and for this reason they will be treated a part.

Osram SFH7050

In particular, the Osram conditioning consists of the following steps, realized with the circuit in Figure 4.6:

a) *Sensor polarization*

In the first step the optical sensor is polarized in order to give the photodiode the right quantity of current to generate the light at the desired wavelength. In this passage, it is important to be sure that the generated current remains stable and constant during all the sensors usage.

In Figure 4.5 is reported the polarization of one of the two LED of the SFH7050, which needs a small junction current. To be sure of the amount of current that will flow in the sensor, a manual trimmer V1 has been placed in the circuit and it can be set at whichever value. As it could be seen, this enters the net LEDO_K1 in Figure 4.5, that corresponds to the sensor cathode. Moreover, driving a periodical commutation directly from the LEDO_G1, that

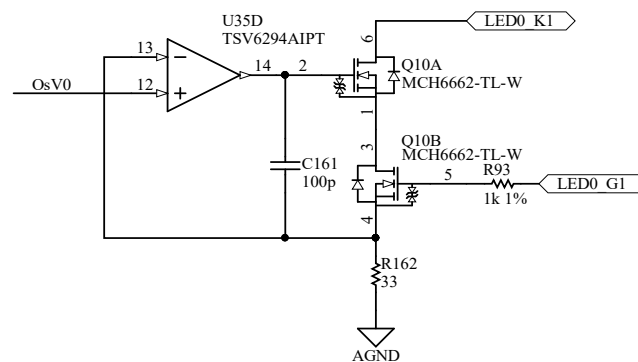


Figure 4.5: Osram Sensor polarization circuit.

coincides with a GPIO port of the MCU, it would be possible to drive the sensor with a pulsating current, easily manageable by the mosfet.

In this work, this circuit has been set to generate a 4 mA current for the SFH7050 led 0 (of the two it has in the package).

b) *Current-to-voltage*

In the second step, the variation of current inducted by the tissue light absorption is transformed in a voltage variation through a special trans-impedance amplifier with settable gain. As explained in Paragraph 1.2.2, the Photo-plethysmogram signal is composed by two contributions one static (the DC component) and one dynamic (the AC). Although only this second is the one of interest, in this initial phase both of them are amplified.

Figure 4.6 report the total conditioning circuit, where each operational amplifier represents a conditioning step. The first, that is the trans-impedance amplifier has two inputs: one is the current collected by the sensor, the second one is an offset voltage (net PDRef1), which is the voltage given to the sensor when it results to be in a baseline condition. In other words, by adjusting the VR10 trimmer it changes the value of sensor current read when the acquisition starts (the DC component).

c) *High-pass filter*

It is an high pass filter to remove the signal continuous component, of third order with a cut off frequency at 0.1 Hz.

d) *Low-pass filter*

In the last step, signal undergoes to a low-pass anti-aliasing filter of first order with a cut off frequency of 482 Hz.

The system is configured to acquire two different Osram signals (for the carotid

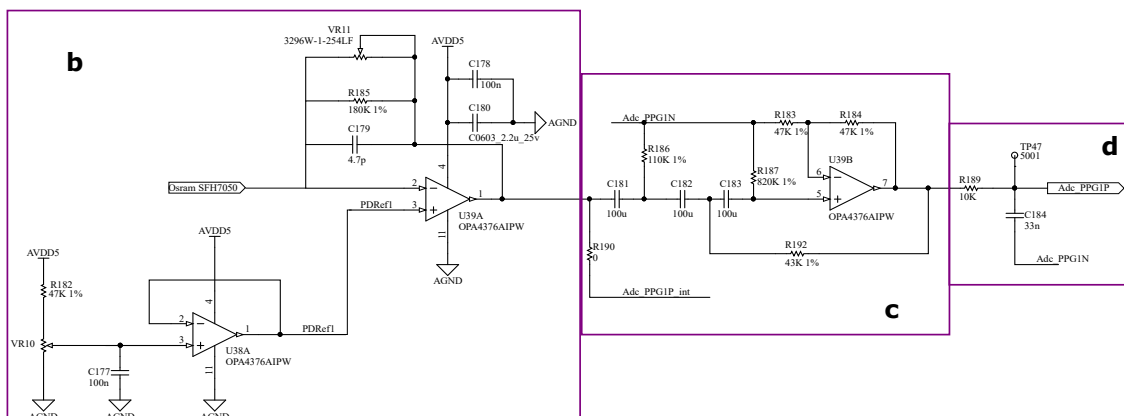


Figure 4.6: Osram sensor analog conditioning circuit.

and femoral acquisitions respectively) that are addressed to channel 4 and 5 of the ADS1299.

SiPM

On the other hand, the SiPM conditioning consists of the following steps, realized with the circuit in Figure 4.8:

a) *Sensor polarization*

For what concerned the SiPM depolarization the circuit is very similar to the one of the Osram optical sensor. The main difference is that it has two different ways to establish the amount of current: digitally through the DAC of the MCU or physically with the trimmer (VR5 in the Figure 4.7).

In this work, it has been chosen to use the latter mode to obtain a current of 4 mA flowing in the SiPM (the same of the previous case).

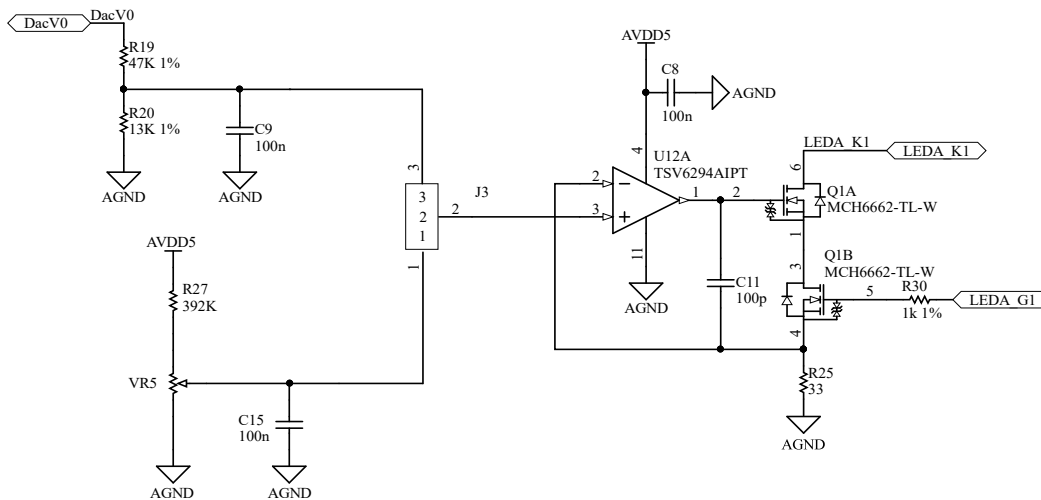


Figure 4.7: SiPM Sensor polarization circuit.

b) *Decoupling*

This stage is formed by a voltage follower to decouple signal from the whole circuit.

c) *High-pass filter*

As for the Osram, to remove the DC component of the signal is applied a high pass filter of third order with a cut off frequency of 0.1 Hz.

d) *Low-pass filter*

The signal is then filtered again but with a low pass filter of first order at

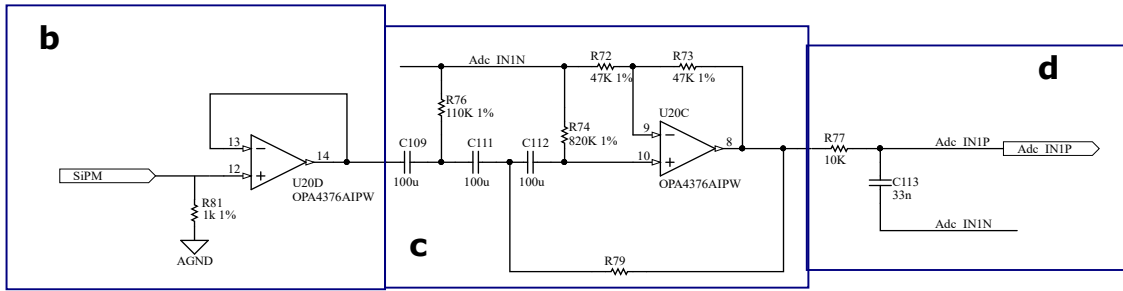


Figure 4.8: SiPM sensor analog conditioning circuit.

482 Hz before entering the ADS1299. In this case the two signals (for femoral and carotid sites) occupy the channel 1 and 2.

4.1.2 Phonocardiogram signal Acquisition

Regarding the phonocardiogram, the acquisition board developed in this project lets to acquire up to two analog MEMS microphones, that have an analog conditioning before entering the channel 6 and 7 of the ADS1299. Figure 4.9 outlines the main step of this part. This is similar to the one developed for the former system, treated in Chapter 3 Paragraph 3.1, that acquires only PCG but with little improvements.

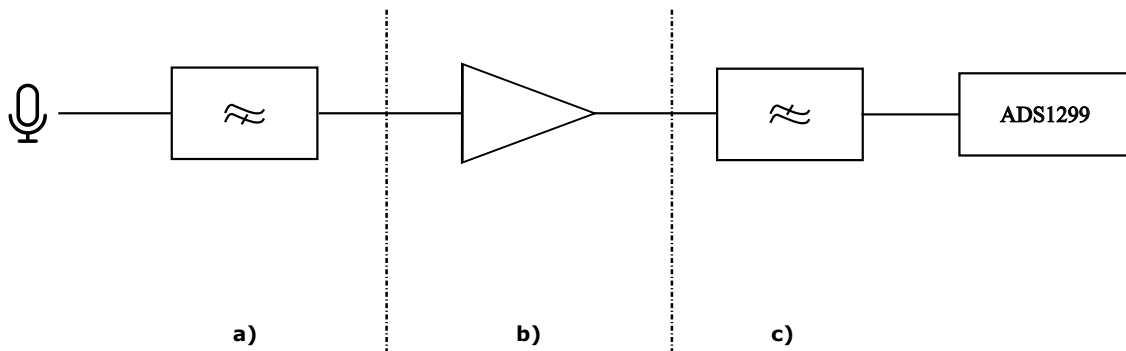


Figure 4.9: Analog microphone conditioning diagram.

In the detail, as implemented in the circuit in Figure 4.10, the sound signal goes through:

a) *High pass filter*

In order to remove the signal offset a third order filter with a cut off frequency of 0.1 Hz is placed in the first stage of the circuit.

b) *Amplification*

To better take advantage of the ADC full range, the signal is amplified in the second step.

c) *Low pass filter*

In the third, an anti-aliasing low pass filter of first order at 482 Hz is applied.

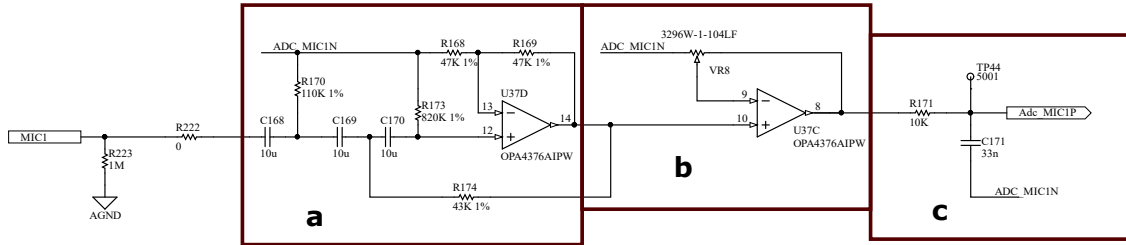


Figure 4.10: Analog microphone conditioning circuit.

4.1.3 Elettrocardiogram signal Acquisition

In the previous prototypes the ECG was acquired by a commercial and certificated device (see Paragraph 2.2) or a commercial evaluation board, the STeval-IME0021V1 (see Paragraph 3.1). In this case, instead, the twelve ECG derivations are directly handle by the analog to digital converter but with some simple expedients shown below.

The board is configured to work with three ECG derivation: the left arm (LA), the right arm (RA) and the right leg (RL). The ECG electrodes are merged in a 15 pin DIN connector and two jumpers allow, firstly, the selection of the shield (J20 to ground in our configuration) and, secondly, if the right leg derivation is amplified to remove the common mode interference (J14 to the right leg driver conditioning). The removal is done giving as input of this stage the output of the mean value between the RA and the LA voltage (Adc2_BIASOUT in Figure 4.11).

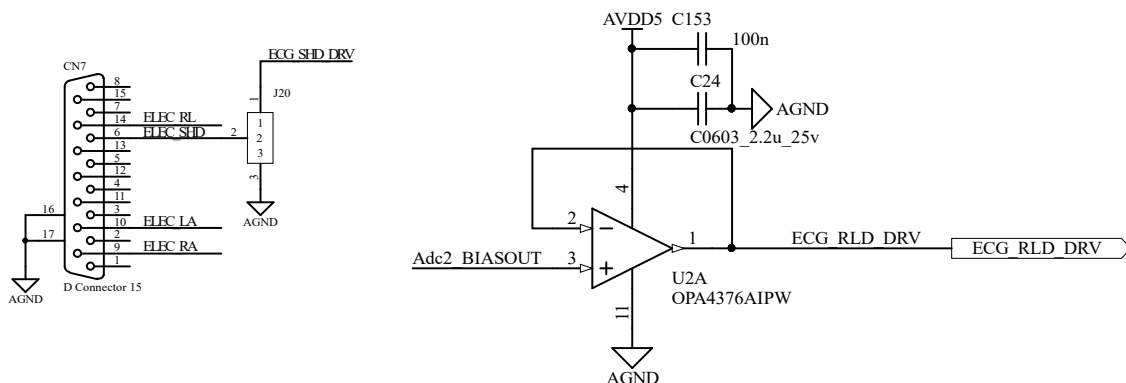


Figure 4.11: Electrocardiogram conditioning circuit.

The electrocardiogram signal then enters the ADS1299 in channel 8 and the relative internal PGA is set with gain 8.

4.1.4 Tonometer signal Acquisition

As said more times in this dissertation, the used tonometer have digital output so they are directly connected to the MCU SPI. In this prototype two tonometers are connected in 3-wire mode (as explain in Paragraph 2.2.1) to SPI4 and SPI5 of the STM32H743ZIT6.

4.1.5 Acquisitions Management

Finally, considering all the collected signal the central MCU has to manage:

- 1 differential ECG (two channel of the ADS1299);
- two PCG signals (corresponding to two channel of the ADS1299);
- two PPG with Osram sensor (corresponding to two channel of the ADS1299);
- two PPG with SiPM sensor (corresponding to two channel of the ADS1299);

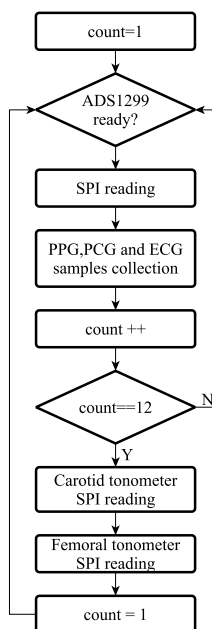


Figure 4.12: The system firmware flowchart.

- two digital tonometers for arterial pulse acquisition (directly connected to the microcontroller)

Also in this case, as it was for the other prototypes described in the preceding chapters, the maximum working frequency of the tonometer is 170 Hz and this has to merge in a synchronous way with the ADS1299 conversion. The configured protocol imposes at the ADC a sampling frequency of 2 kHz, that results to be 12 times the tonometer frequency.

So, in this case, as reported in the flow chart in Figure 4.12 the MCU performs the two tonometer SPIs reading each twelve ADS1299 conversions. As shown in the diagram in Figure 4.3 the ADS1299 is an external analog to digital converter specific for biosignals acquisition and connected to the core through one of the available SPI.

4.2 Signals analysis

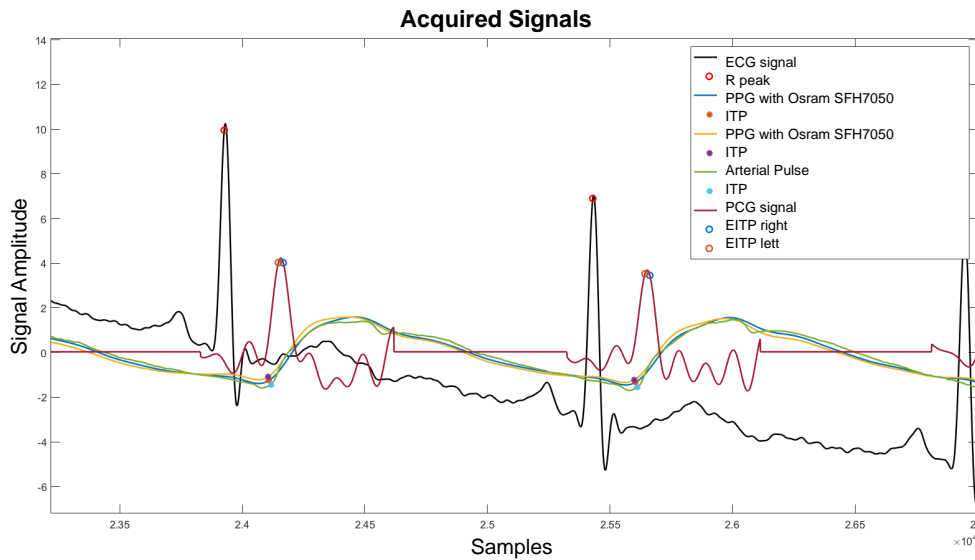


Figure 4.13: All the analyzed signals and relative features.

In this section is explained how are handled the signals once they are post-processed for the Pulse Transit Time extraction. For this purpose, in fact, from each of them a distinct feature has to be extracted to detect the right time of the pulse passage in the considered sites and so the time employed by the blood for the flowing.

Despite the other system already illustrated this one has the characteristic to let the acquisition of all the possible biosignals through which the arterial pulse could be superficially detected in a wearable configuration (thanks to the use of two bands). So, for the signals already treated in the former chapters the described and consolidated algorithms have been implemented. In particular, each signal and the relative method for the feature extraction will be listed as follows and shown in Figure 4.13:

- Pan-Tompkins QRS detection algorithm for the ECG signal
- Intersecting tangent point (ITP) extraction for both the tonometer arterial pulse and the PPG with Osram and SiPM, that let to obtain signal with very similar shape (see Paragraph 2.3.1)
- Ear intersecting point (EITP) identification for the PCG signal, when the displacement part between 0.5 and 20 Hz is considered (see Paragraph 4.13)

4.3 Acquisitions

4.3.1 Carotid acquisition

To compare the performances of all the sensors, they were placed in a special 3d support created in order that each of them can detect the pulse wave through its mechanical transduction. This support, reported in Figure 4.14 is then held by a band that has to be placed around the neck or the leg for the carotid and femoral acquisition respectively.

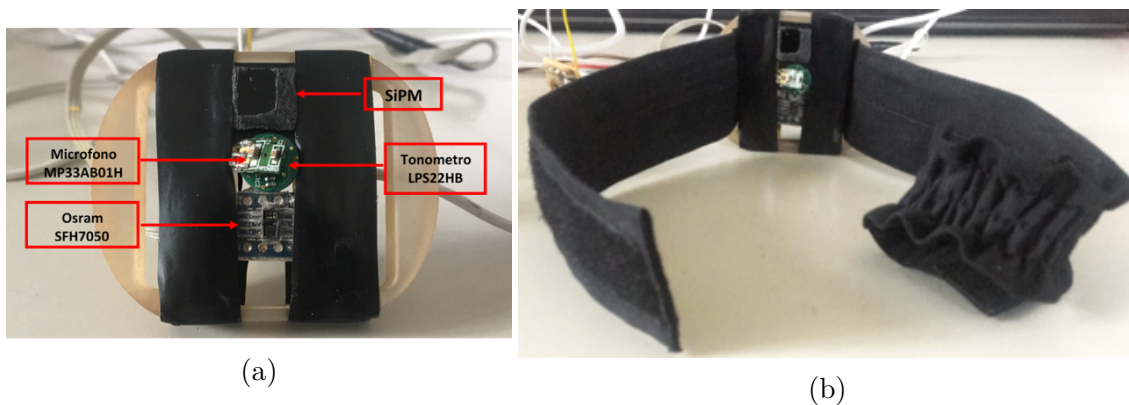


Figure 4.14: Sensor configuration for the total system acquisition. (a) 3d-printed support with the MEMS analog microphone, the tonometer and the two optical sensors; (b) Final acquisition configuration band, where the support can be placed.

With this configuration several carotid acquisitions were done to try to figure out which sensor resulted to be more stable in this configuration and in a long acquisition that could lead to a PWV monitoring, as we would obtain. Table 4.1 reports data achieved for three different acquisitions in the same subject. For each acquisition, N represents the number of events considered to extract the PTT parameter, and N_{out} the discarded ones. The criterion of the PTT_i inclusion is based on:

$$|PTT_i - PTT_{mean}| \geq 0.9 * sd \quad (4.1)$$

Table 4.1: Carotid PTT obtained with all the considered sensors.

Acquisition	Sensor	Feature*	PTT(ms)	SD(ms)	N	N_{out}
1	MIC	l-EITP	104.5	1.02	18	8
		r-EITP	114.1	1	18	8
	TON	ITP	87.1	1.3	15	11
	OSRAM	ITP	85.6	1.4	19	7
	SiPM	ITP	84.4	1.3	17	9
2	MIC	l-EITP	105.3	1.1	15	9
		r-EITP	115	1.3	16	8
	TON	ITP	86.5	1.2	16	8
	OSRAM	ITP	85.2	1.3	16	8
	SiPM	ITP	82.7	1	13	11
3	MIC	l-EITP	104.1	1.0	15	14
		r-EITP	113.5	1.0	15	14
	TON	ITP	87.0	1.1	20	9
	OSRAM	ITP	83.8	1.1	17	12
	SiPM	ITP	81.7	1.2	16	12

*: feature used to evaluate the carotid PTT; SD: standard deviation

N: number of events on which the PTT has been evaluated;

N_{out} : discarded events; l-EITP: left ear intersecting tangent point;

r-EITP: right ear intersecting tangent point; ITP: intersecting tangent point;

With these results was not possible to understand which sensor and feature was better in the monitoring employing, all the standard deviation are very low and each sensor, if compared with its self results to be very repeatable.

4.3.2 Carotid-Femoral acquisition

From the carotid tests shown above were chosen the more valid sensors combination to perform the double sites acquisition. In particular, it was chosen to use the microphones coupled with themselves because they do not result to be aligned with the others. Whereas, the Osram sensor and the tonometer with interchangeability. The resulting examined configurations are:

- a) Tonometer for carotid and Tonometer for femoral;
- b) Osram for carotid and Tonometer for femoral;
- c) Microphone for carotid and Microfone for femoral;

Configuration *a*

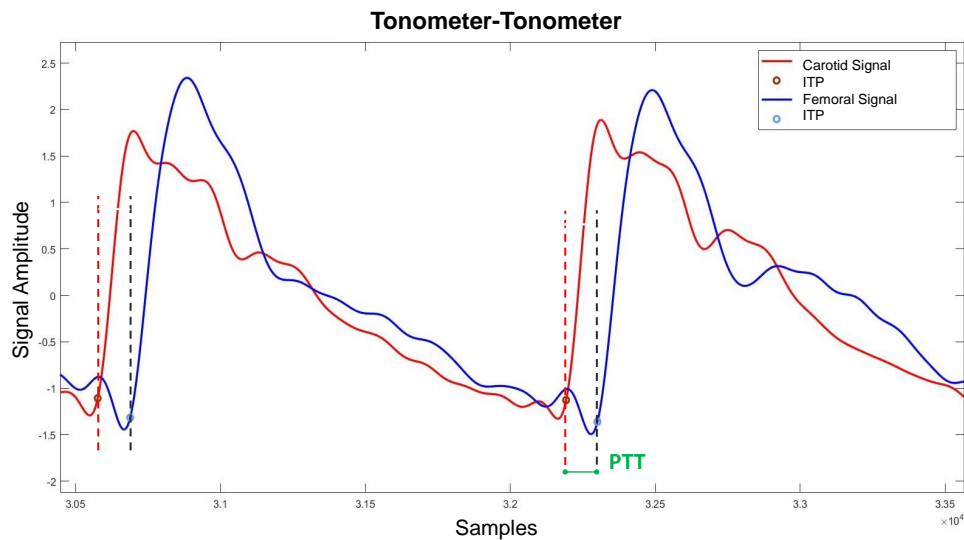


Figure 4.15: Tonometer-Tonometer signals and features.

The Figure 4.15 represents the two signals (carotid and femoral) acquired with two tonometers in a wearable configuration. As it could be seen, their shapes are very similar to the ones obtained encapsulating these devices in two pen-probes usable by a clinical operator (as ATHOS does in Chapter 3) and the resulting PTT are stable and repeatable.

Table 4.2 shows the computed PTT, and relative PWV on two different subjects and for different acquisitions (done on different days). A new parameter of valuation has been inserted: a quality key (QK) that is the ratio between the

Table 4.2: Results for the tonometer-tonometer configuration

Sub	Acq	PTT(ms)	SD(ms)	N	Nout	PTT _R (ms)	PWV(m/s)	QK
1	1	66.63	1.3	32(67%)	16(33%)	67	7.5	2%
	2	67.13	1.28	40(71%)	16(29%)	67	7.45	2%
	3	68.10	1.14	41(71%)	17(29%)	67	7.34	2%
	4	68.74	2.38	51(93%)	4(7%)	67	7.27	3%
1	1	56.81	1.18	113(94%)	7(6%)	56.5	8.8	2%
	2	56.24	1.01	82(95%)	4(5%)	56.5	8.89	2%
	3	57.01	0.88	78(76%)	25(24%)	56.5	8.77	2%
	4	56.95	1.39	91(98%)	2(2%)	56.5	8.78	2%
2	1	54.96	1.13	37(67%)	18(33%)	54	9.1	2%
	2	54.28	1.54	58(98%)	1(2%)	54	9.21	3%
	3	54.65	0.67	43(58%)	31(42%)	54	9.15	1%
	4	55.03	0.92	52(72%)	20(28%)	54	9.09	2%
2	1	56.35	1.09	51(89%)	6(11%)	56.5	8.87	2%
	2	56.50	1.25	47(96%)	2(4%)	56.5	8.85	2%
	3	55.07	1.44	46(96%)	2(4%)	56.5	9.08	3%
	4	54.91	0.75	33(61%)	21(39%)	56.5	9.11	1%

SD: standard deviation; *N*: number of events on which the PTT has been evaluated;
PTT_R(ms): PTT obtained with the reference golden standard;
N_{out}: discarded events; *QK*: quality key;

standard deviation and the final mean PTT. If this is inferior to 6% the acquisition is considered valid.

This configuration shows a high repeatability in term of intra-subject variability and in term of standard deviation for each acquisition. Moreover, it could be observed how the value assessed with the wearable configuration results to be very comparable with the one obtain by an expert operator (column PTT_R in Table 4.2).

Configuration b

Changing the sensor used for the carotid detection with the optical sensor, the signals shapes do not present significant differences, as notable in Figure 4.16.

But, if we move our observation on the performances of the system in term of PTTs, it is notable how the discrepancies with the golden standard get bigger (up to 7 ms) for the subject 2. This trend confirms what was discovered before in the comparing of all the sensor at the carotid sites: the signal obtained through optical sensors are not stable in term of repeatability, very often they tend to anticipate the pulse detected with the tonometer.

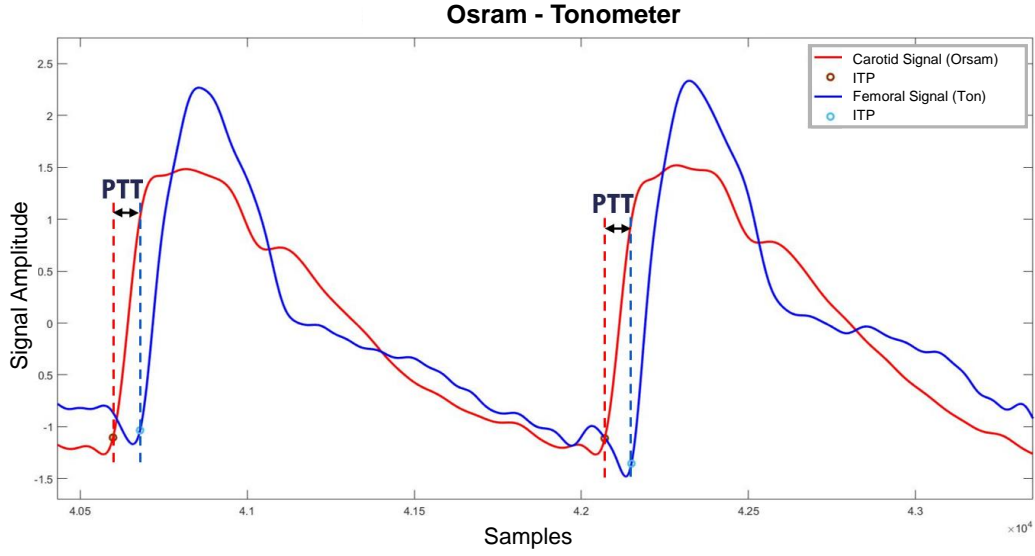


Figure 4.16: Osram-Tonometer signals and features.

Table 4.3: Results for the Osram-tonometer configuration

Sub	Acq	PTT(ms)	SD(ms)	N	Nout	PTTr(ms)	PWV(m/s)	QK
1	1	64,87	2,82	55	14	67	7,71	4%
	2	61,53	2,2	44	21	67	8,13	4%
	3	63,84	2,98	49	21	67	7,83	5%
	4	64,25	1,81	38	28	67	7,78	3%
1	1	60,44	1,39	41	18	62	8,27	2%
	2	61,42	1,79	57	12	62	8,14	3%
	3	61,44	2,21	57	13	62	8,14	4%
	4	58,38	2,8	53	18	62	8,56	5%
2	1	44,29	0,92	41	26	56	11,29	2%
	2	42,02	1,14	48	28	56	11,9	3%
	3	40,71	0,58	38	28	56	12,28	1%
	4	38,75	0,81	54	24	56	12,9	2%
2	1	47,86	1,03	36	18	56	10,45	2%
	2	47,04	1,18	51	9	56	10,63	3%
	3	45,97	0,73	39	18	56	10,88	2%
	4	46,77	1,19	55	9	56	10,69	3%

SD: standard deviation; *N*: number of events on which the *PTT* has been evaluated;

PTT_R(ms): *PTT* obtained with the reference golden standard;

N_{out}: discarded events; *QK*: quality key;

In other words, the results got with this configuration have less reliability compared to the reference and also for the intra-subject tests. For this, the first configuration still results to be better.

Configuration *c*

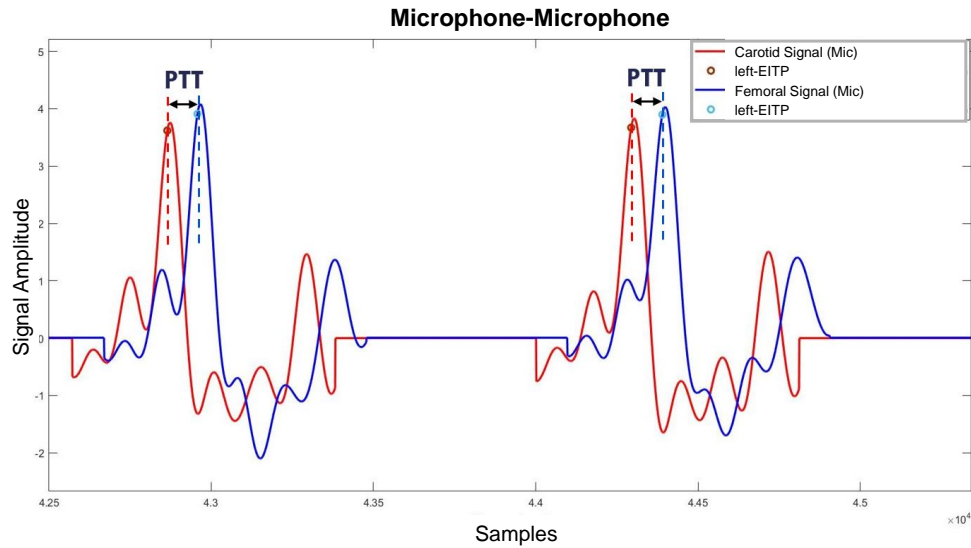


Figure 4.17: Microphone-Microphone signals and features.

Also for this configuration, as for the previous one, using completely different signals shape we obtained PTT value far from the golden standard assessment. Whith this system also the repeatability intra-subject does not excel as it can be seen from the repetition of subject 2. This probably happens because such prototype is still too much vulnerable to the environmental noise that could corrupt the acquisition.

Table 4.4: Results for the microphone-microphone configuration

Sub	Acq	PTT(ms)	SD(ms)	N	Nout	PTTr(ms)	PWV(m/s)	QK
1	1	53.08	1.18	64	13	53.5	9.42	2%
	2	52.27	1.71	91	4	53.5	9.56	3%
	3	53.7	1.93	69	1	53.5	9.31	4%
	4	55.56	2.65	54	3	53.5	9	5%
1	1	51.44	3.37	64	2	49.5	9.72	7%
	2	48.87	1.59	34	27	49.5	10.23	3%
	3	50.33	1.34	36	22	49.5	9.93	3%
	4	50.89	2.47	57	10	49.5	9.82	5%
2	1	47.14	0.61	35	17	52	10.61	1%
	2	47.66	0.56	56	7	52	10.49	1%
	3	48.09	1.13	61	1	52	10.4	2%
	4	47.56	0.61	81	11	52	10.51	1%
2	1	41.57	1.83	49	5	47	12.03	4%
	2	37.28	2.06	54	1	47	13.41	6%
	3	39.59	2.51	57	1	47	12.63	6%
	4	40.45	1.61	46	12	47	12.36	4%

SD: standard deviation; *N*: number of events on which the PTT has been evaluated;

PTT_R(ms): PTT obtained with the reference golden standard;

N_{out}: discarded events; *QK*: quality key;

4.4 Results Discussion

In conclusion, the wearable system that shows the best results in terms of best repeatability of PTT and average PWV values, less intra-subjects variation, and less irregularity of PTT values within the same acquisition is the one formed by the pair tonometer-tonometer.

Chapter 5

PWV with Graphene pressure sensor

In this chapter the last attempt to have a wearable system to pave the way for a continuous monitoring of the Pulse Wave Velocity will be explored. This means to acquire the cardiovascular parameter without the constant presence of a specialized operator. At the beginning of the acquisition, two patches should be placed in the correct acquisition points and then the system will automatically acquire, process the signals and show the parameter extracted each pulse.

To pursue this goal, thanks to the collaboration with Nano chemistry group of “Institut de Science et d’Ingénierie Supramoléculaires” (University of Strasbourg), my work has approached an innovative functionalized graphene-based pressure sensor (FGP sensor) with the aim to have a reliable and cost-effective system in a more wearable solution, compared to the ones depicted in the chapters above.

5.1 HardWare implementation

With this purpose, the PCB acquisition board already used in the project described in the previous Chapter 4 (paragraph 4.1) has been readjusted to acquire, together with the others, also the new graphene pressure sensor (deeply expounded in Paragraph 1.4.4).

At the beginning of the study, the main purpose of the research has been the comparing of the novel sensor with the one that has always results the one performing better in term of repeatability and reliability with the clinical golden standard: the tonometer. Hence, the system overview of this project is represented in Figure 5.1: the acquisition board manages the collection of

two tonometers, two graphene pressure sensors and the ECG signal. As usual, data are then sent to the laptop for the real-time visualization and traces collection.

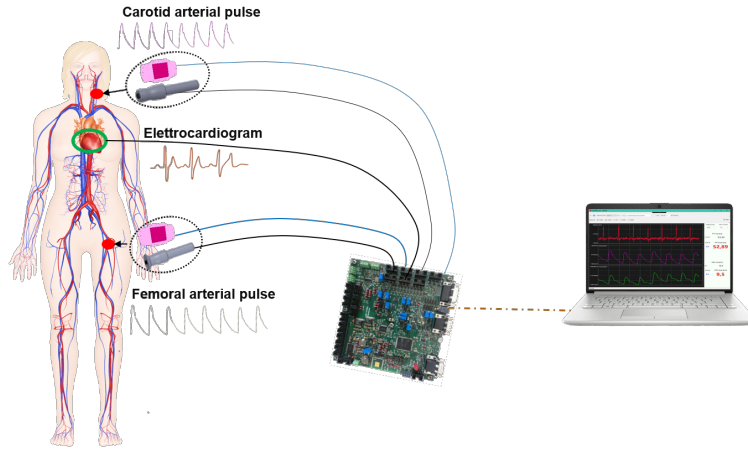


Figure 5.1: System overview of the signals and sensors considered in this part of the project.

As for the monitoring system described in Chapter 4, the STM32H743ZIT6 manages the acquisition of all the signals through various interconnections: digital SPI for the tonometers, and conditioning and then entering the ADS1299 in the case of the analog signals (ECG and graphene pressure sensor). Figure 5.2 schematizes all the new system connections.

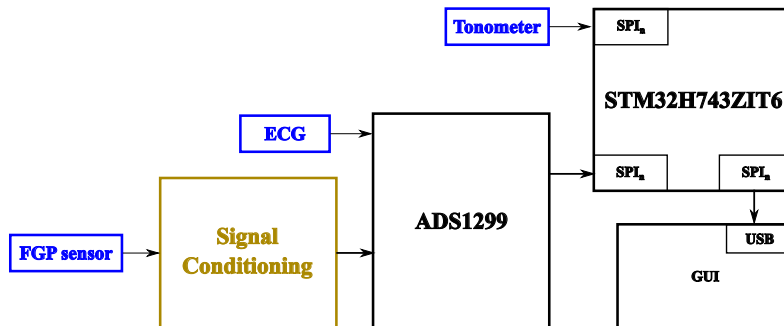


Figure 5.2: New acquisition board flowchart.

5.1.1 Graphene pressure sensor signal Acquisition

The graphene pressure sensor, as said in Paragraph 1.4.4 is a novel piezoresistive device that undergoes to a resistance value change when it detects a pressure variation. The baseline resistance value of this sensor is around $500\ \Omega$ up to $1\ \text{k}\Omega$

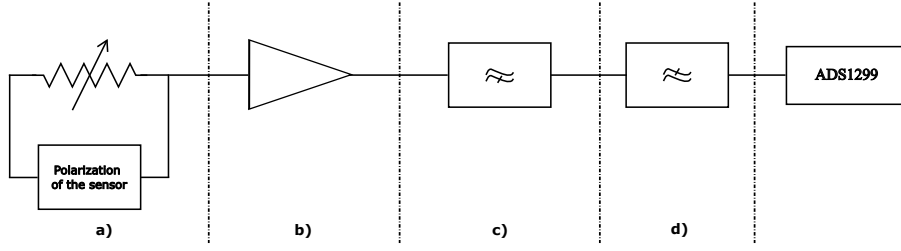


Figure 5.3: Graphene pressure sensor conditioning diagram.

and they can change their value of the 80% respect to the baseline.

To let this sensor to be read by the acquisition board already designed it has been chosen to do a current reading of the sensor adjusting the channel used by the Osram sensor and described in Paragraph 4.1.1. In particular, as shown before, the analog conditioning involves the steps summarizes in the flowchart in Figure 5.3.

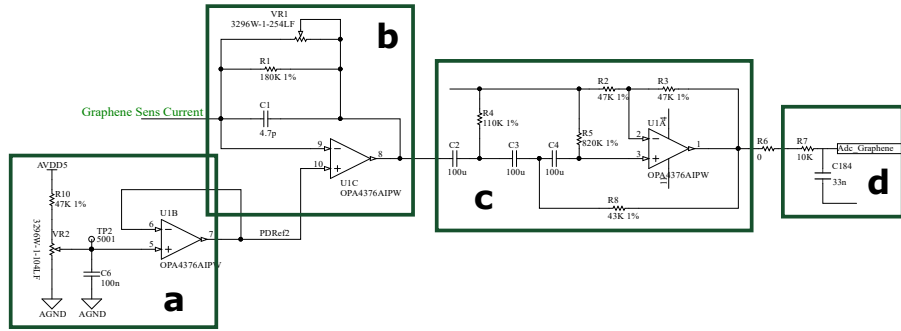


Figure 5.4: Graphene pressure sensor analog conditioning circuit.

Meanwhile, Figure 5.4 reports the total conditioning circuit, where each operational amplifier represents a conditioning step. In the detail, it has:

a) *Sensor polarization*

The first stage is the sensor biasing block in which the proper voltage is generated and applied to the functionalized graphene pressure sensor. To define the correct biasing, the value of the baseline resistance is measured and, with the willing to have a current of few mA flowing in the sensor, the value of voltage is set through the trimmer VR2. For instance, the values resulted from the two sensors mainly used in this prototype are:

$$R_{baseline}^{sens1} = 0.6 \text{ k}\Omega, VD_{ref1} = 0.3 \text{ V}, I_{sens1} = \frac{VD_{ref1}}{R_{baseline}^{sens1}} = 0.5 \text{ mA} \quad (5.1)$$

$$R_{baseline}^{sens1} = 0.5 \text{ k}\Omega, VD_{ref1} = 0.25 \text{ V}, I_{sens1} = \frac{VD_{ref1}}{R_{baseline}^{sens1}} = 0.5 \text{ mA} \quad (5.2)$$

b) *Current-to-voltage*

In the second step, the variation of current inducted by changing in the detected pressure is transformed in a voltage variation through a special trans-impedance amplifier with settable gain, in order to manually adjust the gain of the channel while the acquisition is running.

This trans-impedance amplifier has two inputs: one is the current collected by the sensor, the second one is an offset voltage (net P_{DRef1}), that is the voltage given to the sensor when it results to be in a baseline condition. In other words, by adjusting the VR10 trimmer it changes the value of sensor current read when it starts the acquisition, in a non work condition.

c) *High-pass filter*

It is an high pass filter to remove the signal continuous component of third order with a cut off frequency at 0.1 Hz.

d) *Low-pass filter*

In the last step, signal undergoes to a low-pass filter of first order with a cut off frequency of 482 Hz.

For what concerned the FGP sensor the main problem to solve was the sensor contacts. The cooper wires resulted to be not appropriate for this application and, using other wires, the silver paste on the ITO-PET were very easily removable (Figure 5.5). In fact, due to its fabrication process as it could be seen from Figure 5.5a, the sensor has the connections on both the sides, so one has always to be directly facing the skin and the other the tape. In this way, trying to place the sensor directly in contact with the skin through a tape, we dealt two problems: the obtained waves were too much corrupted by noise for the rubbing and the action to remove and replace the tape many times ruined the sensor itself. Hence, born the need to have an holding of the sensor to prevent the contact of the sensor with the skin and with the tape.

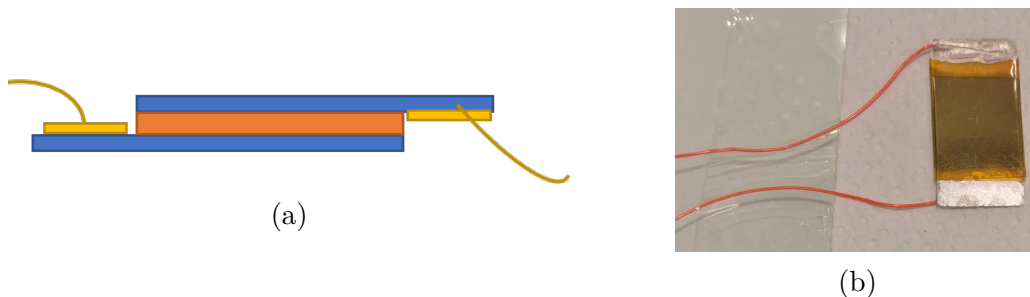


Figure 5.5: Graphene pressure sensor final device configuration(a) and resulting connections(b).

With this purpose several 3D-supports were designed in order to find the right ones that ensure good acquisitions for both the carotid and the femoral sites. The final one, shown in Figure 5.6 is a sensor support, for both the neck and the groin, and with some characteristics: an extension in width to obtain inlets for the elastic bands (leading to a better isolation and easier placement of the sensor), two flaps to cover the electrical contact from the skin side, and a smoothing of all the edges to make the support more comfortable for the patients.

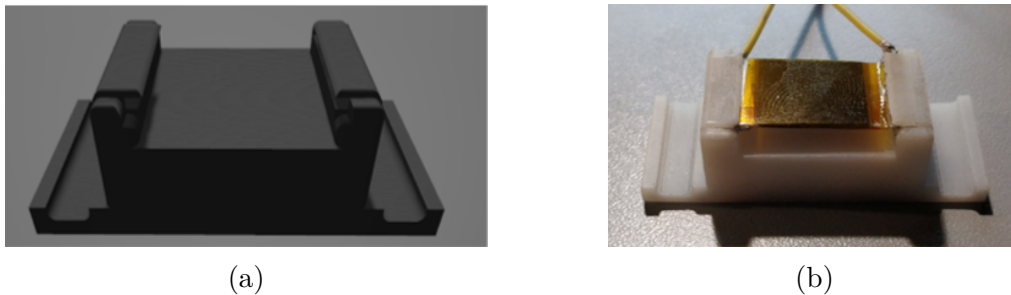


Figure 5.6: Sensor configuration for graphene acquisition. (a) Model of the support for the graphene pressure sensor; (b) Support with the sensor.

5.1.2 Elettrocardiogram signal Acquisition

The twelve ECG derivations are directly handle by the ADS1299 analog to digital converter, as earlier explained in Paragraph 4.1.3.

5.1.3 Tonometer signal Acquisition

As said more times in this dissertation, the used tonometer have digital output so they are directly connected to the MCU SPI. In this prototype two tonometer are connected in 3-wire mode (as explain in Paragraph 2.2.1) to SPI4 and SPI5 od the STM32H743ZIT6.

5.1.4 Acquisitions Management

Concerning the firmware implemented in the microcontroller, it remains the same of the previous system configuration in order to always synchronize the maximum working frequency of the tonometer (180 Hz) and the sample rate of the external ADC (2 kHz). As in Figure 4.12 the MCU performs the two tonometer SPIs reading each twelve ADS1299 conversions.

5.2 Signals Analysis

The graphene sensor, being a device for others application, has a transduction and a working principle quite different from the ones usually used to detect the arterial blood pulse. This, merged with the stand-alone configuration, brought to a signal that has a shape sometimes similar to the common arterial pulse (Figure 5.7a as we saw for the tonometer signal or the photoplethysmogram) and some others with the identification of the pulsatile events, but not having a "good shape", i.e. a clean and strict rising front in which the usual ITP algorithm performs well (Figure 5.7b). To overcome the problem to not necessary obtain a perfect shape wave and try to have a system the more versatile is possible, two different approaches were developed.

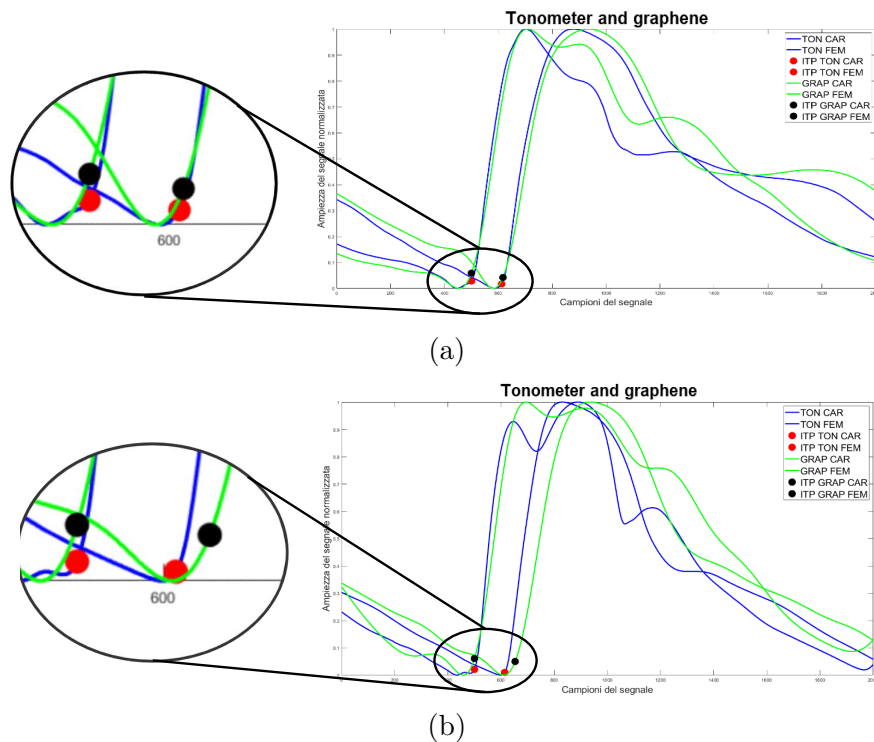


Figure 5.7: (a) Case in which the ITP performs well also with the graphene signal, the two rising fronts are perfectly synchronous; (b) Case of different pending of the signal fronts, but same waves shift

In the detail, these are the three used post-processing techniques and the relative signals where they can be implemented:

- Pan-Tompkins QRS detection algorithm for the ECG signal;

- Intersecting tangent point (ITP) extraction for the tonometer arterial pulse and graphene pressure arterial wave (see Paragraph 2.3.1);
- Cross-correlation evaluation for the graphene pressure arterial wave.

Both the Pan-Tompkins algorithm and the ITP point detection were already got deep in the previous parts of this dissertation, the next paragraph, instead, will explain the cross-correlation approach adopted for the FGP signals.

5.2.1 Cross-correlation technique

We started thinking that the needed information, i.e. the time passed between the two acquired signals, could be obtained evaluating the waves delay without relying on an algorithm that is based on a certain signal shape. As for the telecommunication field, where mathematical formula are use to calculate the time employed by a sinusoidal wave to travel from a point to another, we could considered the carotid and the femoral pulse waves as two quite similar waves that are taken in two different sites and so with a certain phase shift.

This approach, summarized by the flow chart in Figure 5.8, consists of the following step:

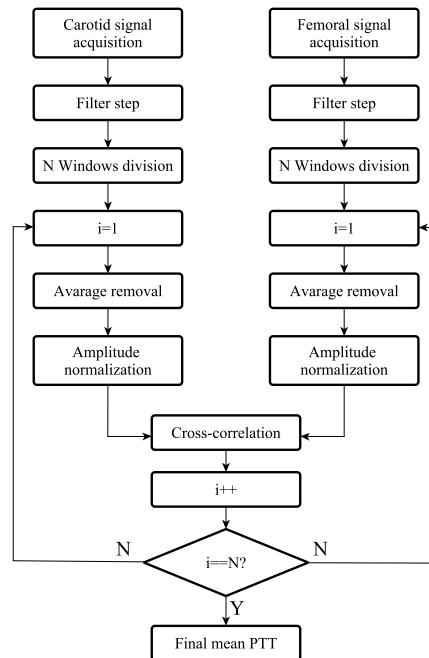


Figure 5.8: Cross-correlation algorithm flow chart.

- The carotid and the femoral signals are filtered with a high pass filter at 0.5 Hz to remove the bias and, later, with a low pass filter with a cut off frequency of 10 Hz to separate only the useful components of the signal;
- The two waves are divided in windows of 5 second;
- In each window the mean value is removed and the amplitude is normalized;
- Through the Matlab function *xcorr* the cross-correlation between every five seconds carotid signal and the relative femoral one is computed. This function gives as result an array of R samples, that coincides with $2x + 1$ (where x is the number of samples in five second of signal).

To estimate the delay, an index (*ind*) has been extracted and corresponds to the x coordinate in which the cross-correlation has the maximum value. The final determined delay (*tmp*) is obtained through the following formula:

$$tmp = abs(ind - [\frac{length(R) - 1}{2}] - 1) \quad (5.3)$$

Where: the *tmp* corresponds to the Pulse Transit Time in samples between the considered femoral and carotid windows;

- For the whole signal N delay values, corresponding to the N divided signal pieces, are computed. The final PTT results to be:

$$PTT = \frac{\sum_{i=1}^N}{N} * \frac{F_s}{1000} \quad (5.4)$$

With N, the number of the individuated windows through the acquired signal, and F_s the simple frequency.

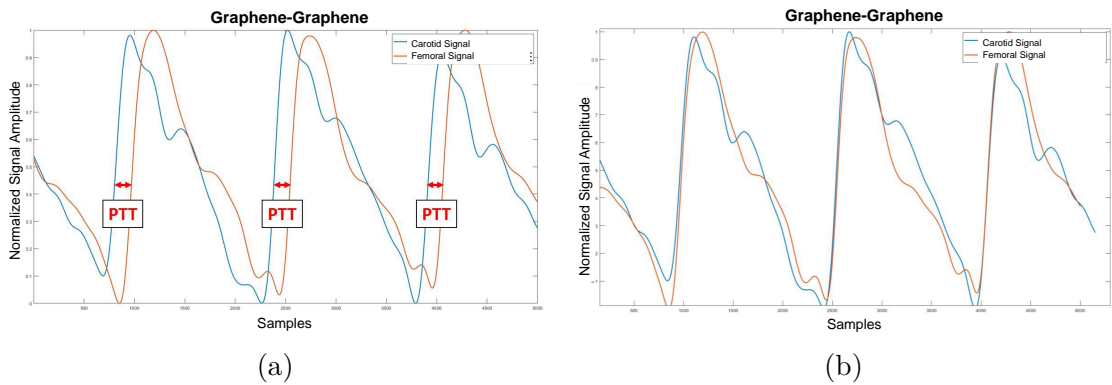


Figure 5.9: (a) Shift between the carotid and the femoral pulse; (b) The resulted delay, evaluated through the cross-correlation technique and applied to the carotid signal

Finally, in Figure 5.9 is reported an example of two signals wherein the ITP algorithm was not well performing. But, thanks to the cross-correlation technique it was possible identify the relative waves delay. In fact, it is visible how applying the estimated shift to the carotid the two pulses become perfectly aligned (Figure 5.9b).

5.3 Validation Results

In order to validate the PWV assessed through this innovative methodology the system depicted in Figure 5.10 was created: a graphene pressure sensor with its 3D support is placed in a bend hold around the neck for carotid acquisition, meanwhile an other graphene sensor with a special semi-spherical support, that ensures a stable grasp to the skin groin, is put in a second bend.

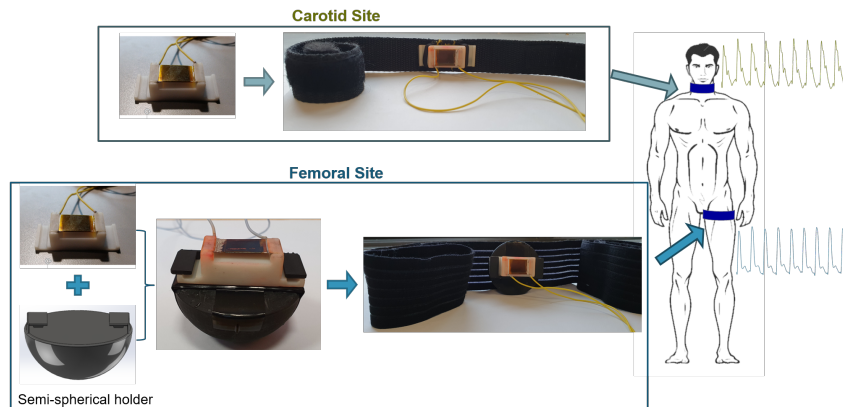


Figure 5.10: Final set up of the graphene system.

After the entire system design, a protocol was established to compare the non-invasive PWV assessment through the graphene with ATHOS (see Chapter 2) and with the clinical golden standard (SphygmoCor). In the first phase, the patient anamnesis is conducted, then through tactile skin palpation the carotid and femoral sites are identified and marked. In this way, we are sure that for all the instruments the distances between the two spots is the same. After this preparation, the two operators perform the acquisitions as reported in Figure 5.11.

5.3.1 ITP method

In Table 5.1 are reported the results obtained on ten subjects with the three devices and applying the ITP to the graphene signals. Meanwhile, the Figure 5.12

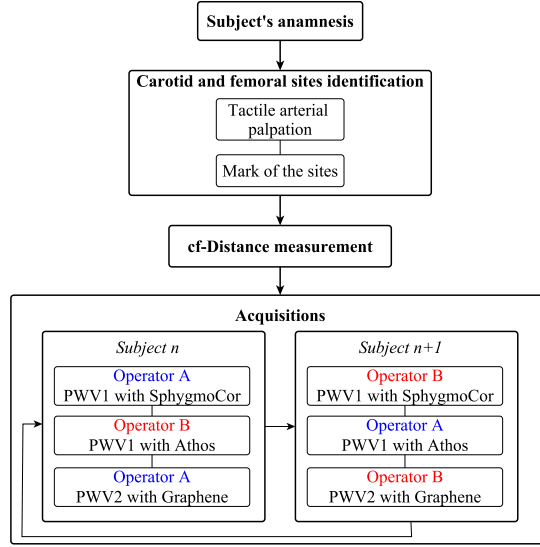


Figure 5.11: Flowchart of the clinical protocol for graphene validation.

reports the Bland Altman Plot of the differences between the clinical golden standard device and the new proposed methodology.

Table 5.1: Graphene (with ITP), ATHOS and SphygmoCor comparison results.

Sub	SphygmoCor		Tonometer		Graphene			PWV _{Sphy}	PWV _{ATH}	PWV _G
	cfPTT	sd	cfPTT	sd	cfPTT	sd	d			
1	72.20	6.36	66.24	0.95	72.05	2.70	472	6.5	7.1	6.6
2	63.30	1.41	58.31	1.51	70.69	2.73	496	7.8	8.5	7.0
3	72.10	1.13	73.41	1.60	79.94	2.90	448	6.2	6.1	5.6
4	74.35	2.33	63.62	0.40	72.22	3.32	488	6.6	7.7	6.8
5	80.40	3.82	66.13	1.28	71.06	2.24	480	6.0	7.3	6.8
6	67.20	6.79	66.81	1.37	74.83	3.82	440	6.5	6.6	5.9
7	77.05	9.40	73.58	0.84	70.75	2.07	520	6.7	7.1	7.4
8	88.00	2.40	86.32	1.88	86.04	2.26	440	5.0	5.1	5.1
9	76.35	2.76	76.63	0.59	85.65	0.45	472	6.2	6.2	5.5
10	75.25	3.61	103.55	1.89	74.98	4.68	440	5.8	4.2	5.9

Sub: stays for subject; *cfPTT*: carotid-femoral Pulse Transit Time

sd: standard deviation in ms; *d*: carotid-femoral distance in mm

PWV_{Sphy}: SphygmoCor Pulse Wave Velocity;

PWV_{ATH}: ATHOS Pulse Wave Velocity;

PWV_G: Graphene Pulse Wave Velocity;

The mean difference between the new methodology and the golden standard resulted to be 0.1 ± 0.56 m/s and it was a good result, considering all the limitation due to the untimely system and all the improvements that can be done in the future.

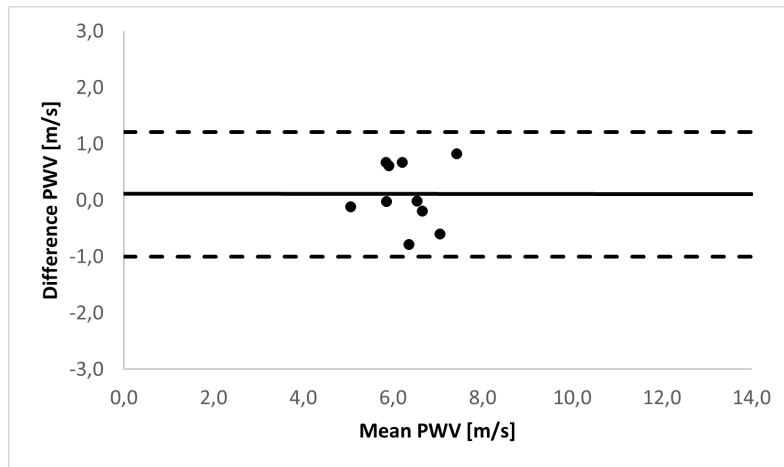


Figure 5.12: Bland Altman plot of the PWV difference between SphygmoCor and the new graphene device.

5.3.2 Cross-correlation method

Regarding the cross-correlation method, instead, we found out that as reported in Table 5.2 and in Figure 5.13 for some subjects let to obtain quite good results, but for the others (like the 8 and the 10) they differ more than with ITP from the golden standard. Here, the mean difference becomes 0.6 ± 1.1 m/s, significantly bigger than before.

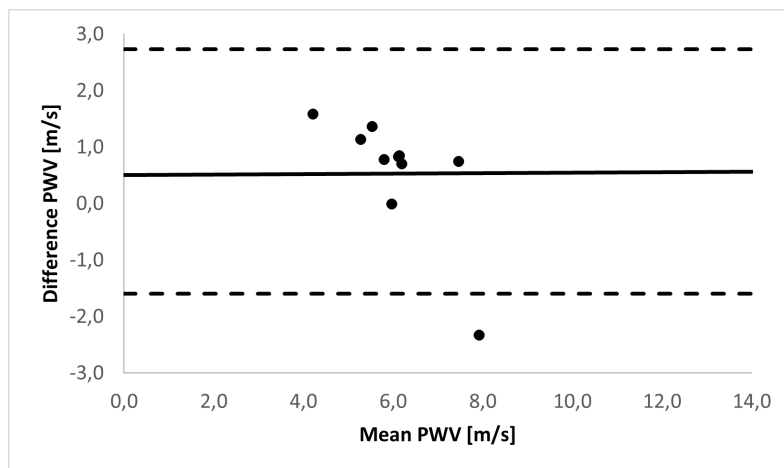


Figure 5.13: Bland Altman plot of the PWV difference between SphygmoCor and the new graphene device, implementing the cross-correlation technique.

Table 5.2: Graphene (with cross-correlation), ATHOS and SphygmoCor comparison results.

Sub	SphygmoCor		Tonometer		Graphene			PWV _{Sphy}	PWV _{ATH}	PWV _G
	cfPTT	sd	cfPTT	sd	cfPTT	sd	d			
1	72.20	6.36	66.24	0.95	82.70	3.03	472	6.5	7.1	5.7
2	63.30	1.41	58.31	1.51	69.97	1.16	496	7.8	8.5	7.1
3	72.10	1.13	73.41	1.60	92.37	1.17	448	6.2	6.1	4.9
4	74.35	2.33	63.62	0.40	85.37	0.21	488	6.6	7.7	5.7
5	80.40	3.82	66.13	1.28	80.30	2.71	480	6.0	7.3	6.0
6	67.20	6.79	66.81	1.37	75.23	6.82	440	6.5	6.6	5.8
7	77.05	9.40	73.58	0.84	57.27	10.67	520	6.7	7.1	9.1
8	88.00	2.40	86.32	1.88	128.75	2.51	440	5.0	5.1	3.4
9	76.35	2.76	76.63	0.59	87.27	1.46	472	6.2	6.2	5.4
10	75.25	3.61	103.55	1.89	93.27	5.11	440	5.8	4.2	4.7

Sub: stays for subject; cfPTT: carotid-fermoral Pulse Transit Time

sd: standard deviation in ms; d: carotid-fermoral distance in mm

PWV_{Sphy}: SphygmoCor Pulse Wave Velocity;

PWV_{ATH}: ATHOS Pulse Wave Velocity;

PWV_G: Graphene Pulse Wave Velocity;

5.4 Results Discussion

In this Chapter was presented the feasibility of an innovative wearable system for the continuous estimation of PWV through graphene pressure sensors. In particular, we were able to obtain stable pulse waves nevertheless the sensors configuration and an algorithm optimization that let to assess PWV with a high accuracy, if compared to the clinical golden standard.

Chapter 6

Conclusions

In collaboration with STMicroelectronics, University of Torino (Città della Salute e della Scienza di Torino Hospital) and PolitoBIOMed Lab interdepartmental laboratory, the main aim of my research project was the design of a low-cost Pulse Wave Velocity (PWV) estimation system.

To spread the adoption of PWV evaluation as a key parameter to assess cardiovascular risk, regardless of other well accepted risk factors, a significant cost reduction on adoptable measurement devices is strongly required. On the other hand, the quality, accuracy, and reliability of the provided results must be preserved together with a simple and fast examination approach based on a portable system.

In this work, ATHOS, a novel noninvasive system for clinical PWV estimation, has been proposed. The presented solution covers all the aspects related to the parameter acquisition and many of them have been improved: starting from the sensing elements, going through the signal processing algorithms and up to the way the user interface brings the operator to a rapid, consistent and real-time displayed result.

Moreover, other several systems were presented, involving different bio-signals and sensors with the common purpose to obtain a device reliable in the measurement, with a procedure easy to carry out and that does not require a high economic investment by the user. Moreover, the main achieved goal was to change and improve the PWV measurement procedure, moving from a discrete and punctual assessment to a parameter monitoring.

PPG, PCG, and Pulse Wave signals were collected and compared in three different systems. All of them were used for PWV evaluation and the results were shown. The ones which performed better (ATHOS) or lets us to obtain a

wearable system (Graphene pressure sensor) were then validated by comparison with Sphygmocor measurements.

These results, considered the gold standard reference equipment, showed a very strong similarity. It is also interesting to note that, in most cases, the acquired results related to the same subject demonstrate better quality and repeatability.

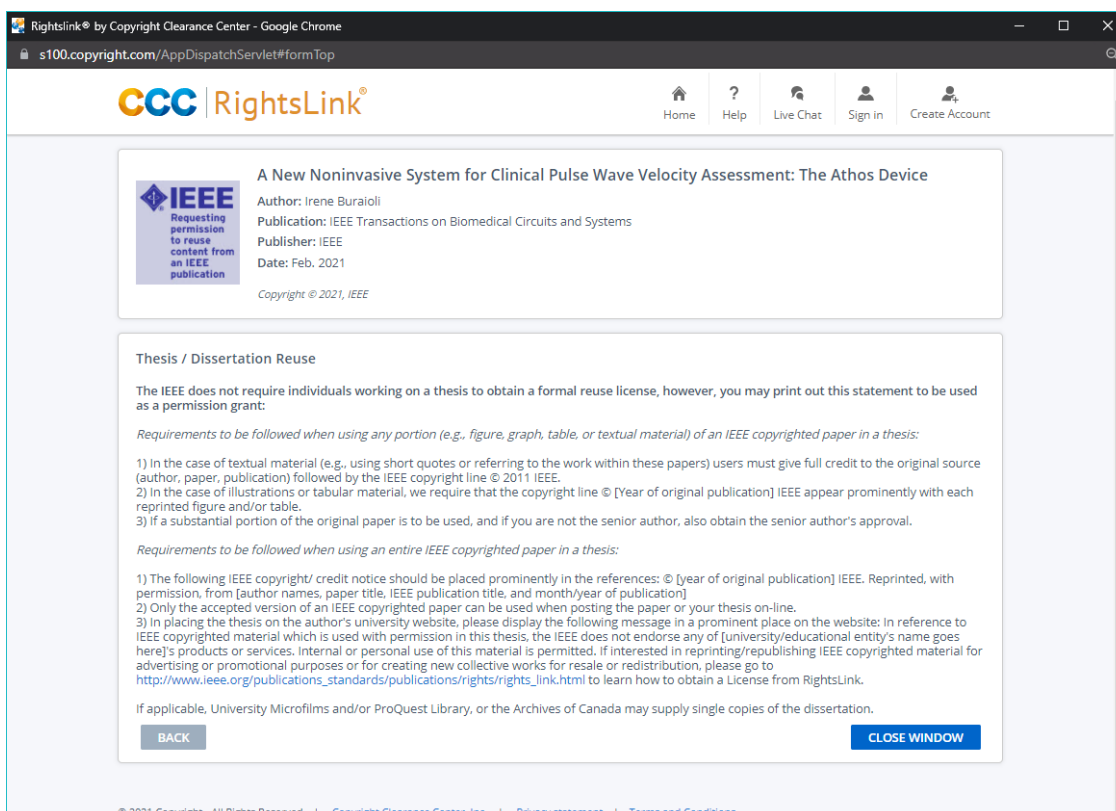
The proof of concept in this research project was to prove the possibility to use innovative sensors together with a novel data processing and graphical user interface.

In conclusion, it was possible to prove:

- how ATHOS has the potential to become a truly cost-effective system that addresses fully reliable and easy to perform PWV estimations with the ambition to expand the availability of this measure and the fields of application;
- the feasibility of obtaining a wearable system to overcome the current PWV measurement limitation through the use of innovative sensors for this cardiovascular parameter monitoring.

Appendix A

Articles copyrights



The screenshot shows the IEEE RightsLink website interface. At the top, there is a navigation bar with the IEEE logo and the text "Requesting permission to reuse content from an IEEE publication". The main content area displays the following information:

A New Noninvasive System for Clinical Pulse Wave Velocity Assessment: The Athos Device
Author: Irene Buraioli
Publication: IEEE Transactions on Biomedical Circuits and Systems
Publisher: IEEE
Date: Feb. 2021
Copyright © 2021, IEEE

Thesis / Dissertation Reuse

The IEEE does not require individuals working on a thesis to obtain a formal reuse license, however, you may print out this statement to be used as a permission grant:

Requirements to be followed when using any portion (e.g., figure, graph, table, or textual material) of an IEEE copyrighted paper in a thesis:

- 1) In the case of textual material (e.g., using short quotes or referring to the work within these papers) users must give full credit to the original source (author, paper, publication) followed by the IEEE copyright line © 2011 IEEE.
- 2) In the case of illustrations or tabular material, we require that the copyright line © [Year of original publication] IEEE appear prominently with each reprinted figure and/or table.
- 3) If a substantial portion of the original paper is to be used, and if you are not the senior author, also obtain the senior author's approval.

Requirements to be followed when using an entire IEEE copyrighted paper in a thesis:

- 1) The following IEEE copyright/ credit notice should be placed prominently in the references: © [year of original publication] IEEE. Reprinted, with permission, from [author names, paper title, IEEE publication title, and month/year of publication]
- 2) Only the accepted version of an IEEE copyrighted paper can be used when posting the paper or your thesis on-line.
- 3) In placing the thesis on the author's university website, please display the following message in a prominent place on the website: In reference to IEEE copyrighted material which is used with permission in this thesis, the IEEE does not endorse any of [university/educational entity's name goes here]'s products or services. Internal or personal use of this material is permitted. If interested in reprinting/republishing IEEE copyrighted material for advertising or promotional purposes or for creating new collective works for resale or redistribution, please go to http://www.ieee.org/publications_standards/publications/rights/rights_link.html to learn how to obtain a License from RightsLink.

If applicable, University Microfilms and/or ProQuest Library, or the Archives of Canada may supply single copies of the dissertation.

At the bottom of the form, there are two buttons: "BACK" and "CLOSE WINDOW".

© 2021 Copyright - All Rights Reserved | Copyright Clearance Center, Inc. | Privacy statement | Terms and Conditions

Figure A.1: IEEE copyright request for Buraioli et al [40].

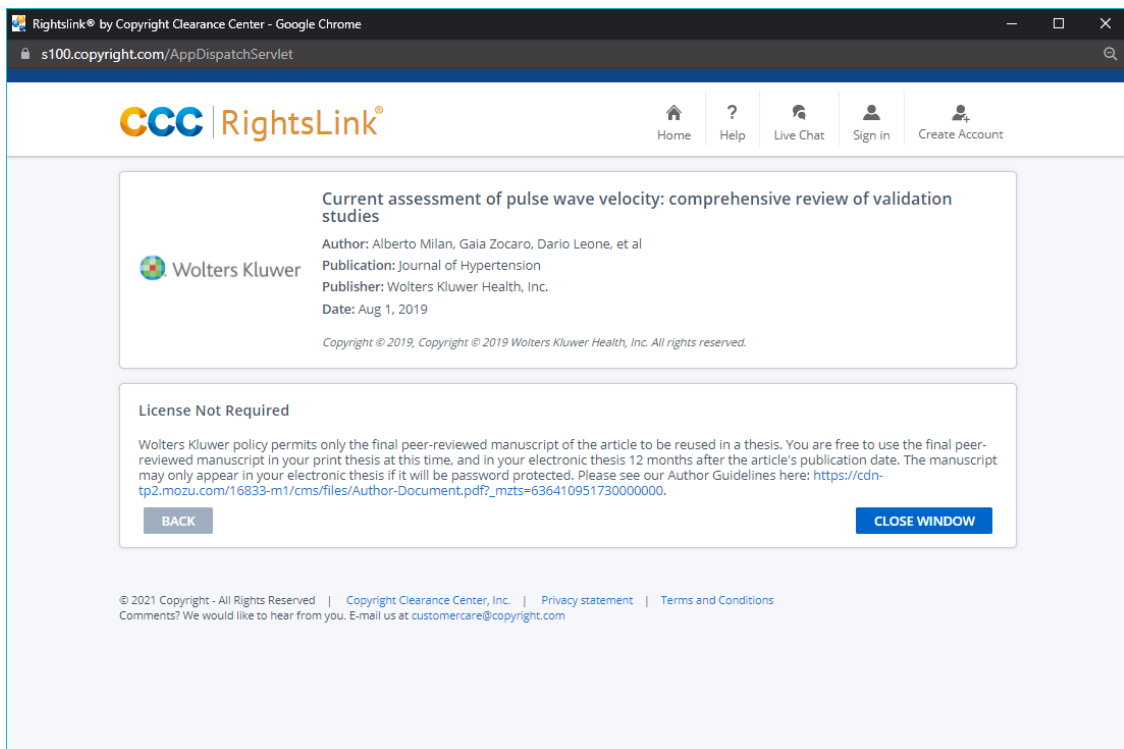


Figure A.2: Wolters Kluwer copyright request for Milan et al [22].

Nomenclature

Acronyms / Abbreviations

aPWV aortic Pulse Wave Velocity

ATHOS Arterial sTiffness faitHful tOol aSsessment

BLE Bluetooth Low Energy

BP Blood Pressure

cfPTT carotid-femoral Pulse Transit Time

cfPWV carotid-femoral Pulse Wave Velocity

COM COMmunication port

CVDs Cardiovascular Diseases

DBP Diastolic Blood Pressure

ECG ElectroCardioGram Signal

EITP Ear intersecting point

FFT Fast-Fourier Transform

FGP Functionalized Graphene-Based

GO Graphene Oxide

GUI Graphical User Interface

ITO Indium Tin Oxide

ITP Intersecting Tangent Point

LED Light Emitting Diode

MEMS Micro Electro-Mechanical Systems

- PCB** Printed Circuit Board
- PCG** PhonoCardioGram Signal
- PET** Polyethylene Terephthalate
- PPG** PhotoPlethysmoGram Signal
- PTT** Pulse Transit Time
- PWA** Pulse Wave Analysis
- PWV** Pulse Wave Velocity
- SBP** Systolic Blood Pressure
- SiPMs** Silicon Photomultipliers
- SNR** Signal-to-Noise Ratio
- SPI** Serial Peripheral Interface

Bibliography

- [1] “Human cardiovascular system | Description, Anatomy, & Function”, Encyclopedia Britannica. (), [Online]. Available: <https://www.britannica.com/science/human-cardiovascular-system> (visited on 02/23/2021).
- [2] R. Fernandez-Jimenez, B. D. Hoit, R. A. Walsh, *et al.*, “NORMAL PHYSIOLOGY OF THE CARDIOVASCULAR SYSTEM”, in *Hurst’s The Heart*, V. Fuster, R. A. Harrington, J. Narula, *et al.*, Eds., 14th ed., New York, NY: McGraw-Hill Education, 2017. [Online]. Available: accessmedicine.mhmedical.com/content.aspx?aid=1161723424 (visited on 02/23/2021).
- [3] “CV physiology | cardiac cycle”. (), [Online]. Available: <https://www.cvphysiology.com/Heart%20Disease/HD002> (visited on 03/02/2021).
- [4] B. Williams, G. Mancia, W. Spiering, *et al.*, “2018 ESC/ESH Guidelines for the management of arterial hypertension”, *European Heart Journal*, vol. 39, no. 33, pp. 3021–3104, Sep. 1, 2018, ISSN: 1522-9645. DOI: 10.1093/eurheartj/ehy339. pmid: 30165516.
- [5] P. A. Iaizzo, Ed., *Handbook of Cardiac Anatomy, Physiology, and Devices*, 3rd ed. Springer International Publishing, 2015, ISBN: 978-3-319-19463-9. DOI: 10.1007/978-3-319-19464-6. [Online]. Available: <https://www.springer.com/gp/book/9783319194639> (visited on 06/14/2021).
- [6] L. Ortiz Martin, P. Picazo-Sanchez, P. Peris-Lopez, *et al.*, “Heartbeats Do Not Make Good Pseudo-Random Number Generators: An Analysis of the Randomness of Inter-Pulse Intervals”, *Entropy*, vol. 20, p. 94, Jan. 30, 2018. DOI: 10.3390/e20020094.
- [7] M. Elgendi, “On the Analysis of Fingertip Photoplethysmogram Signals”, *Current Cardiology Reviews*, vol. 8, no. 1, p. 14, Feb. 2012. DOI: 10.2174/157340312801215782. pmid: 22845812. [Online]. Available: <https://www.ncbi.nlm.nih.gov/pmc/articles/PMC3394104/> (visited on 03/09/2021).
- [8] T. Tamura, Y. Maeda, M. Sekine, *et al.*, “Wearable Photoplethysmographic Sensors—Past and Present”, *Electronics*, vol. 3, no. 2, pp. 282–302, 2 Jun. 2014. DOI: 10.3390/electronics3020282. [Online]. Available: <https://www.mdpi.com/2079-9292/3/2/282> (visited on 03/17/2021).

- [9] F. Mezirani, S. M. Debbal, and A. Atbi, “Analysis of phonocardiogram signals using wavelet transform”, *Journal of Medical Engineering & Technology*, vol. 36, no. 6, pp. 283–302, Aug. 1, 2012, ISSN: 0309-1902. DOI: 10.3109/03091902.2012.684830. [Online]. Available: <https://doi.org/10.3109/03091902.2012.684830> (visited on 03/19/2021).
- [10] J. Maddury, “Arterial Pulse”, *Indian Journal of Cardiovascular Disease in Women - WINCARS*, vol. 02, no. 04, pp. 099–110, Dec. 2017, ISSN: 2455-7854. DOI: 10.1055/s-0038-1636691. [Online]. Available: <http://www.thieme-connect.de/DOI/DOI?10.1055/s-0038-1636691> (visited on 04/12/2021).
- [11] G. Mancina, R. Fagard, K. Narkiewicz, *et al.*, “2013 ESH/ESC Guidelines for the management of arterial hypertension”, *European Heart Journal*, vol. 34, no. 28, pp. 2159–2219, Jul. 21, 2013, ISSN: 0195-668X. DOI: 10.1093/eurheartj/ehz151. [Online]. Available: <https://academic.oup.com/eurheartj/article/34/28/2159/451304> (visited on 02/24/2020).
- [12] Safar Michel E., Levy Bernard I., and Struijker-Boudier Harry, “Current Perspectives on Arterial Stiffness and Pulse Pressure in Hypertension and Cardiovascular Diseases”, *Circulation*, vol. 107, no. 22, pp. 2864–2869, Jun. 10, 2003. DOI: 10.1161/01.CIR.0000069826.36125.B4. [Online]. Available: <https://www.ahajournals.org/doi/full/10.1161/01.CIR.0000069826.36125.B4> (visited on 02/24/2020).
- [13] J. A. Chirinos, P. Segers, T. Hughes, *et al.*, “Large-Artery Stiffness in Health and Disease: JACC State-of-the-Art Review”, *Journal of the American College of Cardiology*, vol. 74, no. 9, pp. 1237–1263, Sep. 3, 2019, ISSN: 0735-1097. DOI: 10.1016/j.jacc.2019.07.012. [Online]. Available: <http://www.sciencedirect.com/science/article/pii/S0735109719358437> (visited on 01/15/2021).
- [14] Segers Patrick, Rietzschel Ernst R., and Chirinos Julio A., “How to Measure Arterial Stiffness in Humans”, *Arteriosclerosis, Thrombosis, and Vascular Biology*, vol. 40, no. 5, pp. 1034–1043, May 1, 2020. DOI: 10.1161/ATVBAHA.119.313132. [Online]. Available: <https://www.ahajournals.org/doi/10.1161/ATVBAHA.119.313132> (visited on 01/15/2021).
- [15] J. Solà, O. Chételat, C. Sartori, *et al.*, “Chest pulse-wave velocity: A novel approach to assess arterial stiffness”, *IEEE transactions on bio-medical engineering*, vol. 58, no. 1, pp. 215–223, Jan. 2011, ISSN: 1558-2531. DOI: 10.1109/TBME.2010.2071385. pmid: 20813631.
- [16] Resnick Lawrence M., Militianu Daniela, Cunnings Amy J., *et al.*, “Direct Magnetic Resonance Determination of Aortic Distensibility in Essential Hypertension”, *Hypertension*, vol. 30, no. 3, pp. 654–659, Sep. 1, 1997. DOI: 10.1161/01.HYP.30.3.654. [Online]. Available: <https://www.ahajournals.org/doi/full/10.1161/01.hyp.30.3.654> (visited on 02/24/2020).

- [17] L. M. Van Bortel, S. Laurent, P. Boutouyrie, *et al.*, “Expert consensus document on the measurement of aortic stiffness in daily practice using carotid-femoral pulse wave velocity”, *Journal of Hypertension*, vol. 30, no. 3, pp. 445–448, Mar. 2012, ISSN: 0263-6352. DOI: 10.1097/HJH.0b013e32834fa8b0. [Online]. Available: https://journals.lww.com/jhypertension/Abstract/2012/03000/Expert_consensus_document_on_the_measurement_of.1.aspx (visited on 02/24/2020).
- [18] C. M. McEniery, M. Spratt, M. Munnery, *et al.*, “An analysis of prospective risk factors for aortic stiffness in men: 20-year follow-up from the Caerphilly prospective study”, *Hypertension (Dallas, Tex.: 1979)*, vol. 56, no. 1, pp. 36–43, Jul. 2010, ISSN: 1524-4563. DOI: 10.1161/HYPERTENSIONAHA.110.150896. pmid: 20530296.
- [19] Reference Values for Arterial Stiffness’ Collaboration, “Determinants of pulse wave velocity in healthy people and in the presence of cardiovascular risk factors: ’establishing normal and reference values’”, *European Heart Journal*, vol. 31, no. 19, pp. 2338–2350, Oct. 2010, ISSN: 1522-9645. DOI: 10.1093/eurheartj/ehq165. pmid: 20530030.
- [20] P. M. Nabeel, V. R. Kiran, J. Joseph, *et al.*, “Local Pulse Wave Velocity: Theory, Methods, Advancements, and Clinical Applications”, *IEEE reviews in biomedical engineering*, vol. 13, pp. 74–112, 2020, ISSN: 1941-1189. DOI: 10.1109/RBME.2019.2931587. pmid: 31369386.
- [21] T. Pereira, C. Correia, and J. Cardoso, “Novel Methods for Pulse Wave Velocity Measurement”, *Journal of Medical and Biological Engineering*, vol. 35, no. 5, pp. 555–565, 2015, ISSN: 1609-0985. DOI: 10.1007/s40846-015-0086-8. pmid: 26500469. [Online]. Available: <https://www.ncbi.nlm.nih.gov/pmc/articles/PMC4609308/> (visited on 02/24/2020).
- [22] A. Milan, G. Zocaro, D. Leone, *et al.*, “Current assessment of pulse wave velocity: Comprehensive review of validation studies”, *Journal of Hypertension*, vol. 37, no. 8, pp. 1547–1557, Aug. 2019, ISSN: 1473-5598. DOI: 10.1097/HJH.0000000000002081. pmid: 30882597.
- [23] V. Bikia, S. Pagoulatou, B. Trachet, *et al.*, “Noninvasive Cardiac Output and Central Systolic Pressure From Cuff-Pressure and Pulse Wave Velocity”, *IEEE Journal of Biomedical and Health Informatics*, vol. 24, no. 7, pp. 1968–1981, Jul. 2020, ISSN: 2168-2208. DOI: 10.1109/JBHI.2019.2956604.
- [24] J. Joseph, P. M. Nabeel, S. R. Rao, *et al.*, “Assessment of Carotid Arterial Stiffness in Community Settings With ARTSENS®”, *IEEE Journal of Translational Engineering in Health and Medicine*, vol. 9, pp. 1–11, 2021, ISSN: 2168-2372. DOI: 10.1109/JTEHM.2020.3042386.

- [25] P. M. Nabeel, S. Karthik, J. Joseph, *et al.*, “Arterial Blood Pressure Estimation From Local Pulse Wave Velocity Using Dual-Element Photoplethysmograph Probe”, *IEEE Transactions on Instrumentation and Measurement*, vol. 67, no. 6, pp. 1399–1408, Jun. 2018, ISSN: 1557-9662. DOI: 10.1109/TIM.2018.2800539.
- [26] M. Butlin and A. Qasem, “Large Artery Stiffness Assessment Using SphygmoCor Technology”, *Pulse*, vol. 4, no. 4, pp. 180–192, 2016, ISSN: 2235-8676, 2235-8668. DOI: 10.1159/000452448. pmid: 28229053. [Online]. Available: <https://www.karger.com/Article/FullText/452448> (visited on 06/15/2021).
- [27] M.-H. Hwang, J.-K. Yoo, H.-K. Kim, *et al.*, “Validity and reliability of aortic pulse wave velocity and augmentation index determined by the new cuff-based SphygmoCor Xcel”, *Journal of Human Hypertension*, vol. 28, no. 8, pp. 475–481, 8 Aug. 2014, ISSN: 1476-5527. DOI: 10.1038/jhh.2013.144. [Online]. Available: <https://www.nature.com/articles/jhh2013144> (visited on 06/15/2021).
- [28] “SphygmoCor XCEL”, ATCOR. (), [Online]. Available: <https://atcormedical.com/technology/sphygmocor-xcel/> (visited on 05/16/2021).
- [29] P. Salvi, G. Lio, C. Labat, *et al.*, “Validation of a new non-invasive portable tonometer for determining arterial pressure wave and pulse wave velocity: The PulsePen device”, *Journal of Hypertension*, vol. 22, no. 12, pp. 2285–2293, Dec. 2004, ISSN: 0263-6352. DOI: 10.1097/00004872-200412000-00010. pmid: 15614022.
- [30] “DiaTecne s.r.l./Products/PulsePen”. (), [Online]. Available: <https://www.pulsepen.com/pulsepen.html>.
- [31] F. Stea, E. Bozec, S. Millasseau, *et al.*, “Comparison of the Complior Analyse device with Sphygmocor and Complior SP for pulse wave velocity and central pressure assessment”, *Journal of Hypertension*, vol. 32, no. 4, pp. 873–880, Apr. 2014, ISSN: 1473-5598. DOI: 10.1097/HJH.000000000000091. pmid: 24509122.
- [32] “Complior | products”. (), [Online]. Available: <http://www.complior.com/products> (visited on 06/15/2021).
- [33] H. Ig, N. A, L. Z, *et al.*, “Invasive validation of a new oscillometric device (Arteriograph) for measuring augmentation index, central blood pressure and aortic pulse wave velocity.”, *Journal of Hypertension*, vol. 28, no. 10, pp. 2068–2075, Oct. 1, 2010, ISSN: 0263-6352, 1473-5598. DOI: 10.1097/hjh.0b013e32833c8a1a. pmid: 20651604. [Online]. Available: <https://europepmc.org/article/med/20651604> (visited on 06/15/2021).

- [34] “Arteriograph - NIBP patient monitor by TensioMed | MedicalExpo”. (), [Online]. Available: <https://www.medicalexpo.com/prod/tensioemed/product-77436-541335.html> (visited on 06/15/2021).
- [35] S. S. Hickson, M. Butlin, J. Broad, *et al.*, “Validity and repeatability of the Vicorder apparatus: A comparison with the SphygmoCor device”, *Hypertension Research: Official Journal of the Japanese Society of Hypertension*, vol. 32, no. 12, pp. 1079–1085, Dec. 2009, ISSN: 1348-4214. DOI: 10.1038/hr.2009.154. PMID: 19779487.
- [36] “Vicorder™ SMT - Laboratorio vascolare portatile per esami vascolari periferici e cardiovascolari - Medical Graphics”. (), [Online]. Available: <https://www.medgraphics.it/vicordertm-smt-laboratorio-vascolare-portatile-per-esami-vascolari-periferici-e-cardiovascolari/> (visited on 06/15/2021).
- [37] G. Styczynski, A. Rdzanek, A. Pietrasik, *et al.*, “Echocardiographic Assessment of Aortic Pulse-Wave Velocity: Validation against Invasive Pressure Measurements”, *Journal of the American Society of Echocardiography: Official Publication of the American Society of Echocardiography*, vol. 29, no. 11, pp. 1109–1116, Nov. 2016, ISSN: 1097-6795. DOI: 10.1016/j.echo.2016.07.013. PMID: 27614541.
- [38] J. Calabria, P. Torguet, M. Garcia, *et al.*, “Doppler ultrasound in the measurement of pulse wave velocity: Agreement with the Complior method”, *Cardiovascular Ultrasound*, vol. 9, p. 13, Apr. 15, 2011, ISSN: 1476-7120. DOI: 10.1186/1476-7120-9-13. PMID: 21496271.
- [39] J. J. M. Westenberg, E. P. van Poelgeest, P. Steendijk, *et al.*, “Bramwell-Hill modeling for local aortic pulse wave velocity estimation: A validation study with velocity-encoded cardiovascular magnetic resonance and invasive pressure assessment”, *Journal of Cardiovascular Magnetic Resonance: Official Journal of the Society for Cardiovascular Magnetic Resonance*, vol. 14, p. 2, Jan. 9, 2012, ISSN: 1532-429X. DOI: 10.1186/1532-429X-14-2. PMID: 22230116.
- [40] I. Buraioli, D. Lena, A. Sanginario, *et al.*, “A New Noninvasive System for Clinical Pulse Wave Velocity Assessment: The Athos Device”, *IEEE Transactions on Biomedical Circuits and Systems*, vol. 15, no. 1, pp. 133–142, Feb. 2021, ISSN: 1940-9990. DOI: 10.1109/TBCAS.2021.3058010.
- [41] S. Conoci, F. Rundo, G. Fallica, *et al.*, “Live Demonstration of Portable Systems based on Silicon Sensors for the monitoring of Physiological Parameters of Driver Drowsiness and Pulse Wave Velocity”, in *2018 IEEE Biomedical Circuits and Systems Conference (BioCAS)*, Oct. 2018, pp. 1–3. DOI: 10.1109/BIOCAS.2018.8584709.

- [42] “MP33AB01H - MEMS audio surface-mount bottom-port silicon microphone with analog output - STMicroelectronics”. (), [Online]. Available: <https://www.st.com/en/audio-ics/mp33ab01h.html> (visited on 06/16/2021).
- [43] M. Quintana, E. Vazquez, and M. Prato, “Organic Functionalization of Graphene in Dispersions”, *Accounts of Chemical Research*, vol. 46, no. 1, pp. 138–148, Jan. 15, 2013, ISSN: 0001-4842. DOI: 10.1021/ar300138e. [Online]. Available: <https://doi.org/10.1021/ar300138e> (visited on 05/07/2021).
- [44] C.-B. Huang, S. Witomska, A. Aliprandi, *et al.*, “Molecule–Graphene Hybrid Materials with Tunable Mechanoresponse: Highly Sensitive Pressure Sensors for Health Monitoring”, *Advanced Materials*, vol. 31, no. 1, p. 1804600, 2019, ISSN: 1521-4095. DOI: 10.1002/adma.201804600. [Online]. Available: <https://onlinelibrary.wiley.com/doi/abs/10.1002/adma.201804600> (visited on 05/07/2021).
- [45] “IEC 60601-1 - Medical electrical equipment - Part 1: General requirements for basic safety and essential performance”. (), [Online]. Available: <https://webstore.iec.ch/publication/2603>.
- [46] Y. C. Chiu, P. W. Arand, S. G. Shroff, *et al.*, “Determination of pulse wave velocities with computerized algorithms”, *American Heart Journal*, vol. 121, no. 5, pp. 1460–1470, May 1, 1991, ISSN: 0002-8703. DOI: 10.1016/0002-8703(91)90153-9. [Online]. Available: <http://www.sciencedirect.com/science/article/pii/0002870391901539> (visited on 02/25/2020).
- [47] “Biquad Cascade IIR Filters Using a Direct Form II Transposed Structure”. (), [Online]. Available: https://www.keil.com/pack/doc/CMSIS/DSP/html/group__BiquadCascadeDF2T.html (visited on 05/22/2021).
- [48] A. L. Wentland, T. M. Grist, and O. Wieben, “Review of MRI-based measurements of pulse wave velocity: A biomarker of arterial stiffness”, *Cardiovascular Diagnosis and Therapy*, vol. 4, no. 2, pp. 193–206, Apr. 2014, ISSN: 2223-3652. DOI: 10.3978/j.issn.2223-3652.2014.03.04. pmid: 24834415. [Online]. Available: <https://www.ncbi.nlm.nih.gov/pmc/articles/PMC3996237/> (visited on 02/26/2020).
- [49] T. Weber, M. Ammer, M. Rammer, *et al.*, “Non-invasive determination of carotid–femoral pulse wave velocity depends critically on assessment of travel distance: A comparison with invasive measurement”, *Journal of Hypertension*, vol. 27, no. 8, pp. 1624–1630, Aug. 2009, ISSN: 0263-6352. DOI: 10.1097/HJH.0b013e32832cb04e.

- [50] I. B. Wilkinson, C. M. McEniery, G. Schillaci, *et al.*, “ARTERY Society guidelines for validation of non-invasive haemodynamic measurement devices: Part 1, arterial pulse wave velocity”, *Artery Research*, vol. 4, no. 2, pp. 34–40, Mar. 2010, ISSN: 1876-4401. DOI: 10.1016/j.artres.2010.03.001. [Online]. Available: <https://www.atlantis-press.com/journals/artres/125927448> (visited on 05/30/2021).
- [51] J. Pan and W. J. Tompkins, “A Real-Time QRS Detection Algorithm”, *IEEE Transactions on Biomedical Engineering*, vol. BME-32, no. 3, pp. 230–236, Mar. 1985, ISSN: 0018-9294. DOI: 10.1109/TBME.1985.325532. [Online]. Available: <http://ieeexplore.ieee.org/document/4122029/> (visited on 06/04/2021).

This Ph.D. thesis has been typeset by means of the \TeX -system facilities. The typesetting engine was pdf \LaTeX . The document class was `toptesi`, by Claudio Beccari, with option `tipotesi=scudo`. This class is available in every up-to-date and complete \TeX -system installation.